

CGER'S SUPERCOMPUTER MONOGRAPH REPORT Vol.27

**Numerical studies on the variety of climates of exoplanets
using idealistic configurations**

**Masaki Ishiwatari, Kensuke Nakajima, Shin-ichi Takehiro,
Yuta Kawai, Yoshiyuki O. Takahashi, George L. Hashimoto,
Youhei Sasaki and Yoshi-Yuki Hayashi**

Center for Global Environmental Research



National Institute for Environmental Studies, Japan



CGER'S SUPERCOMPUTER MONOGRAPH REPORT Vol.27

**Numerical studies on the variety of climates of exoplanets
using idealistic configurations**

**Masaki Ishiwatari, Kensuke Nakajima, Shin-ichi Takehiro,
Yuta Kawai, Yoshiyuki O. Takahashi, George L. Hashimoto,
Youhei Sasaki and Yoshi-Yuki Hayashi**

Center for Global Environmental Research



National Institute for Environmental Studies, Japan



CGER'S SUPERCOMPUTER MONOGRAPH REPORT Vol.27

Numerical studies on the variety of climates of exoplanets using idealistic configurations

**Masaki Ishiwatari, Kensuke Nakajima, Shin-ichi Takehiro,
Yuta Kawai, Yoshiyuki O. Takahashi, George L. Hashimoto,
Youhei Sasaki and Yoshi-Yuki Hayashi**

Edited by:

Center for Global Environmental Research (CGER)
National Institute for Environmental Studies (NIES)

Coordination for Resource Allocation of the Supercomputer:

Center for Global Environmental Research (CGER)
National Institute for Environmental Studies (NIES)

Supercomputer Steering Committee (FY2020):

Masayoshi Ishii (Meteorological Research Institute, Japan Meteorological Agency)
Masaki Satoh (Atmosphere and Ocean Research Institute, The University of Tokyo)
Seiya Nishizawa (Computational Climate Science Research Team, RIKEN AICS)
Akinori Takami (Center for Regional Environmental Research, NIES)
Nobuaki Yoshiguchi (Planning Department, NIES)
Hisashi Yashiro (Center for Global Environmental Research, NIES)
Hideharu Akiyoshi (Center for Global Environmental Research, NIES)
Seita Emori (Center for Global Environmental Research, NIES)

Maintenance of the Supercomputer System:

Environmental Information Department (EID)
National Institute for Environmental Studies (NIES)

Operation of the Supercomputer System:

NEC Corporation

Copies of this report can be obtained from:

Center for Global Environmental Research (CGER)
National Institute for Environmental Studies (NIES)
16-2 Onogawa, Tsukuba, Ibaraki, 305-8506 Japan
Fax: +81-29-858-2645
E-mail: www-cger@nies.go.jp

This report is also available as a PDF file.

See: <http://www.cger.nies.go.jp/ja/activities/supporting/publications/report/index.html>

Copyright 2021:

NIES: National Institute for Environmental Studies

This publication is printed on paper manufactured entirely from recycled material (Rank A), in accordance with the Law Concerning the Promotion of Procurement of Eco-Friendly Goods and Services by the State and Other Entities.

ISSN 1341-4356 (printed version), ISSN 2434-5679 (online version), CGER-I153-2021

Foreword

The Center for Global Environmental Research (CGER) at the National Institute for Environmental Studies (NIES) was established in October 1990, with the main objectives of contributing to the scientific understanding of global environmental change and identifying solutions to critical environmental problems. CGER conducts environmental research from an interdisciplinary, multi-agency, and international perspective, and provides an intellectual infrastructure for research activities in the form of databases and a supercomputer system. CGER also ensures that data from its long-term monitoring of the global environment is made available to the public.

CGER installed its first supercomputer system (NEC SX-3, Model 14) in March 1992, and this was subsequently upgraded to an NEC Model SX-4/32 in 1997, an NEC Model SX-6 in 2002, an NEC Model SX-8R/128M16 in 2007, an NEC Model SX-9/A(ECO) in June 2013, and an NEC Model SX-ACE in June 2015. In March 2020, the system was further upgraded with the inclusion of an NEC Model SX-Aurora TSUBASA A511-64 to provide an increased capacity for speed and storage.

The supercomputer system is available for use by researchers from NIES and other research organizations and universities in Japan. The Supercomputer Steering Committee consists of leading Japanese scientists in climate modeling, atmospheric chemistry, ocean environment, computer science, and other areas concerned with global environmental research, and one of its functions is to evaluate proposals of any research requiring the use of the supercomputer system.

To promote the dissemination of results, we publish both Annual Reports and occasional Monograph Reports. Annual Reports deliver the results of all research projects that have made use of the supercomputer system in a given year, while Monograph Reports present the integrated results of a particular research program.

This Monograph presents the results obtained in numerical studies performed by a research group of GFD Dennou Club. The contents are based mainly on two papers: Ishiwatari et al. (2002) and Noda et al. (2017). In these studies, a variety of climates of aquaplanets with gray atmosphere are investigated by changing the values of solar constant and the horizontal distribution of incoming solar radiation flux. Since simple physical schemes and idealized model configurations are used in these studies, the results obtained by experiments are more understandable compared to results obtained by sophisticated models and are expected to provide a theoretical framework for acquiring a general understanding of the maintenance mechanism and existence conditions of various climates. The results will contribute to investigations of the variety of climates of exoplanets and the stability of Earth's climate.

In the years to come, we intend to continue our support for environmental research by enabling the use of our supercomputer resources and continue to disseminate practical information based on our results.

March 2021

三枝信子

Nobuko Saigusa

Director

Center for Global Environmental Research

National Institute for Environmental Studies

Preface

This volume of the CGER'S SUPERCOMPUTER MONOGRAPH REPORT series is the 27th publication of research outcomes achieved by users of the supercomputer facilities at the Center for Global Environmental Research (CGER) at the National Institute for Environmental Studies (NIES).

The authors have investigated a variety of climates of aquaplanets with gray atmosphere taking exoplanets into consideration using atmospheric general circulation models. Exoplanets are planets that exist around stars outside our solar system and are considered to have a climate different from the climate of Earth. The authors have focused on extreme climates of planets with amounts and a horizontal distribution of incident solar flux different from those of the Earth, since solar flux is one of the most important parameters for determining climate. In the experiments, the runaway greenhouse state emerged when the amount of solar flux (solar constant) increased by several tens of percent. The runaway greenhouse state is the nonequilibrium atmospheric state in which temperature and atmospheric water vapor keep increasing. In the runaway greenhouse state, liquid water disappears from the planetary surface, thus the surface environment would not be suitable for harboring life. As for the extreme horizontal distribution of solar flux, the authors investigated the climates of synchronously rotating planets. A synchronously rotating planet has the same rotation period as the orbital period due to strong tidal force and is a possible type of exoplanet. Since such planets have a peculiar distribution of incoming flux with a perpetual dayside and a nightside, the climate would be severe for life.

This monograph is a summary of two papers that consider extreme climates: Ishiwatari et al. (2002) that examined the occurrence conditions of the runaway greenhouse state, and Noda et al. (2017) that examined the climates of synchronously rotating planets. These papers provide knowledge about the various climates from mild to extreme of aquaplanets with gray atmosphere. Although the models used in these studies are simple, the results can be described by simpler conceptual models such as one-dimensional models and can be used as a theoretical framework for considering the variety of planetary climates. We believe that the publication of this monograph will be valuable as a summary of such a theoretical framework. It is expected that the consideration of the occurrence conditions of the drastic change in climate will become a basis for the examination of the stability of Earth's climate. This monograph will also contribute to assessing the habitability of terrestrial-type exoplanets that have been discovered and will be discovered in the future.

March 2021

石渡 正樹

Masaki Ishiwatari
Professor
Graduate School of Science
Hokkaido University

Contents

Foreword	i
Preface	ii
Contents	iii
List of Figures	vi
List of Tables	x

Numerical studies on the variety of climates of exoplanets using idealistic configurations	1
---	----------

Abstract	3
-----------------------	----------

Chapter 1	
Introduction	5

1.1 Drastic climate change caused by the change of the solar constant: occurrence of the runaway greenhouse state	7
1.2 Circulation structures of planets with a peculiar distribution of solar flux	8
1.3 Contents of this monograph	9

Chapter 2	
Model description	11

2.1 Basic assumptions	12
2.2 An overview of GCMs	12
2.3 Discretization	12
2.4 Atmospheric constituents and radiation processes	12
2.5 Physical processes other than radiation processes	13
2.6 Surface conditions	13
2.7 Model modification for experiments with increased solar constant	14
2.7.1 p_s change due to evaporation and condensation	14
2.7.2 Upper damping layer	14
2.7.3 Vertical filter	15

Chapter 3	
Occurrence condition of the runaway greenhouse state in a three-dimensional system	17

3.1 Introduction	18
3.2 Model configuration	18

3.3 Emergence of thermally runaway states.....	22
3.4 Comparison with a one-dimensional system.....	23
3.5 Circulation structure toward the runaway greenhouse state.....	27
3.6 Remarks.....	35
3.7 Summary	35

Chapter 4

Circulation structure of planets with a peculiar distribution of incoming solar radiation flux: climate of synchronously rotating planets37

4.1 Introduction	38
4.2 Model configuration.....	38
4.3 Dependence of the atmospheric circulation characteristics on the planetary rotation rate.....	40
4.4 Typical atmospheric circulation structures	43
4.4.1 Type-I: Day-night convection (Case $\Omega 0.0$)	44
4.4.2 Type-II: Stationary Rossby wave on broad equatorial westerly jet (Case $\Omega 0.15$) ...	46
4.4.3 Type-III: Long time scale north-south asymmetric variability (Case $\Omega 0.75$).....	50
4.4.4 Type-IV: Mid-latitude westerly jets (Case $\Omega 1.0$).....	54
4.5 Day-night energy transport.....	57
4.5.1 Dependence on Ω^*	57
4.5.2 Moist atmosphere radiation limit constraint	59
4.6 Dependence on resolution	60
4.7 Summary	63

Chapter 5

Preliminary results obtained for cloudy atmosphere with non-gray radiation.....65

5.1 Introduction	66
5.2 Model configuration.....	66
5.3 Results	67
5.4 Summary	68

Chapter 6

Conclusion and discussion69

6.1 Summary	70
6.2 Ongoing problem and future plans.....	70
Acknowledgements	73
References	73
Contact person.....	75

CGER'S SUPERCOMPUTER ACTIVITY REPORT (previously published)	77
NIES Supercomputer Annual Report (previously published).....	77
CGER'S SUPERCOMPUTER MONOGRAPH REPORT (previously published)	77

List of Figures

Chapter 1

- 1.1 Relationships between surface temperature and OLR for gray atmosphere. The black solid line shows σT_s^4 . Other solid lines represent equilibrium solutions obtained by the vertical one-dimensional radiative-convective model. The green, red, orange, and blue lines represent the results for $p_{n0}=10^6, 10^5, 10^4, 0$ Pa, respectively. p_{n0} is the partial pressure of dry air at the surface. The solid dashed-line represents the Komabayashi-Ingersoll limit obtained by the stratosphere model. Modified from Ishiwatari (2014), Fig. 1..... 7
- 1.2 Small-mass exoplanets discovered by astronomical missions. The ordinate is the mass of the central host star and the abscissa is the semi-major axis. Red crosses represent exoplanets discovered until 2014 with a mass smaller than ten times of Earth's mass. The data were obtained at <http://exoplanet.eu>. Large black dots represent planets in the solar system. Orange lines represent 10.0, 1.0. and 0.1 times of Earth's solar constant. Thin blue lines represent 1 day, 10 days, and 100 days of the orbital period. The thick blue line represents the tidal lock radius inside which planets are considered to be synchronously rotating planets. 8

Chapter 3

- 3.1 Meridional distributions of incoming solar radiation flux. Unit is W m^{-2} . Thick solid line, dashed line and dotted line are for $S=1380 \text{ W m}^{-2}$, $S=1200 \text{ W m}^{-2}$ and $S=1800 \text{ W m}^{-2}$, respectively. Dotted-dashed line indicates the Komabayashi-Ingersoll limit (385.2 W m^{-2}), and thin solid line indicates the upper-limit value of OLR (355.0 W m^{-2}) obtained by the NHA92 model. Both of them are calculated with the parameters of the present study. From Ishiwatari et al. (2002), Fig. 1. 20
- 3.2 Time evolutions of (a) global mean OLR (W m^{-2}) and (b) global mean surface temperature (K). Dashed line, solid line, dotted line and dashed-dotted line indicate experiments S1200, S1380, S1570 and S1800, respectively. From Ishiwatari et al. (2002), Fig. 2. 22
- 3.3 The relationship between global mean SSR and global mean OLR. The values of OLR at day 1000 are plotted except for S1600 where the value is at day 2000. White circles represent the cases where the atmosphere reaches an equilibrium state, while cross marks represent the cases where the atmosphere is in a thermally runaway state. Note that the values of OLR for thermally runaway states are continuously decreasing. From Ishiwatari et al. (2002), Fig. 3..... 23
- 3.4 The meridional distributions of (a) zonal mean OLR (W m^{-2}) and (b) zonal mean surface temperature (K) of the cases in which the system reaches equilibrium states. Thick solid line, dotted line, dotted-dashed line, dashed line, and thin solid line indicate experiments S1570, S1550, S1500, S1380, and S1200, respectively. The data are temporally averaged between days 950 and 1000. From Ishiwatari et al. (2002), Fig. 4. 24
- 3.5 Vertical distributions of temperature obtained by one-dimensional model with relative humidity of 60% for the radiation scheme. The profiles are plotted by specifying the values of temperature at the bottom of atmosphere as those obtained by the experiments. Ordinates are (a) pressure (Pa) and (b) optical depth. Cross marks indicate surface temperature. From Ishiwatari et al. (2002), Fig. 5. 25
- 3.6 Vertical distributions of zonally averaged temperature at the equator for various values of solar constant. Ordinates are (a) pressure (Pa) and (b) optical depth. The profiles obtained in the experiments S1800, S1700, S1600, S1570, S1550, S1500, S1380,

	S1200 are plotted. Cross marks indicate surface temperature. From Ishiwatari et al. (2002), Fig. 6.	25
3.7	The relationship between surface temperature (K) and OLR (Wm^{-2}). Curves represent surface temperature--OLR relationship obtained by the one-dimensional radiative-convective equilibrium model with various values of relative humidity for the radiation scheme. Thin solid line, dotted line, thick solid line and dashed line indicate 100% of relative humidity (the same as the results of NHA92), 80%, 60% and 40%, respectively. Marks represent the relationship between equatorial zonal mean values of surface temperature and OLR obtained by GCM. White circles and cross marks represent the results where the system reaches an equilibrium state and where the system cannot, respectively. From Ishiwatari et al. (2002), Fig. 7.	26
3.8	Meridional structures of the zonal mean circulation fields of the experiment S1380: (a) temperature, (b) condensation heating, (c) specific humidity, (d) relative humidity, (e) mass stream function, and (f) zonal wind. Contour intervals are (a) 5 K, (b) 5×10^{-6} K day ⁻¹ , (c) 2×10^{-3} , (d) 0.05, (e) 5 m s ⁻¹ , (f) 1.0×10^{10} kg s ⁻¹ , respectively. Time mean fields between t=950 to 1000 days are plotted. From Ishiwatari et al. (2002), Fig.8.	28
3.9	Same as in Fig. 3.8 but for the experiment S1570. Contour intervals are the same as in Fig. 3.8 except for (c) 1.0×10^{-2} . From Ishiwatari et al. (2002), Fig.9.	29
3.10	Same as in Fig. 3.8 but for the experiment S1800. Time-mean fields between t=870 to 920 days are plotted. Contour intervals are the same as in Fig. 3.8 except for (b) 1.0×10^{-5} K day ⁻¹ and (c) 0.1. From Ishiwatari et al. (2002), Fig.10.	30
3.11	Meridional structure of zonal mean optical depth in the experiments (a) S1380, (b) S1570, and (c) S1800. Here, σ is used as the vertical coordinate. The contour intervals are (a) 0.05, (b) 0.2, and (c) 5.0, respectively. The shaded areas in (c) represent the area with optical depth less than 1. From Ishiwatari et al. (2002), Fig.11.	32
3.12	Meridional structure of temperature with the optical depth as the vertical coordinate in the experiments (a) S1380, (b) S1570, and (c) S1800. The areas without data correspond to the regions below the ground surface. The contour intervals are (a) 2.5K, (b) 2.5K, and (c) 5.0K, respectively. From Ishiwatari et al. (2002), Fig.12.	33
3.13	The meridional distributions of vertical energy fluxes in experiments (a) S1380, (b) S1570, and (c) S1800. Thick solid line, dashed line, dotted line, dashed-dotted line, and thin solid line indicate condensation heating (RAIN), evaporation flux (EVAP), OLR, net longwave radiation at the surface (SLR), and sensible heat flux (SENS), respectively. Unit is W m^{-2} . The condensation heating of (c) has its maximum value of 920 W m^{-2} at the equator. From Ishiwatari et al. (2002), Fig.13.	34

Chapter 4

4.1	Horizontal distribution of the incoming solar flux [W m^{-2}] given by Eq. (4.1). Contour interval is 300 Wm^{-2} . From Noda et al. (2017), Fig. 1.	39
4.2	Time series of global mean quantities. (a) Surface temperature [K] and (b) OLR [Wm^{-2}]. Green, light-blue, black, and red lines indicate $\Omega 0.0$, $\Omega 0.15$, $\Omega 0.75$, and $\Omega 1.0$, respectively. From Noda et al. (2017), Fig. 2.	40
4.3	Horizontal distributions of 1000-day mean surface temperature for all of the computed values of Ω^* . Contour interval is 5 K. From Noda et al. (2017), Fig. 3.	41
4.4	Ω^* dependences of (a) surface temperature [K] at the subsolar point, (b) surface temperature [K] at the antisolar point, (c) zonal mean equatorial zonal wind [m s^{-1}] at $\sigma = 0.17$, and (d) degree of north-south asymmetry of surface temperature defined by Eq. (4.2) in the text [K]. The values are temporal averages between day 1000 and day 2000. All 10 runs for each Ω^* case are plotted. Red and blue lines are ensemble	

	averages for the small- Ω and the large- Ω branches, respectively. From Noda et al. (2017), Fig. 4.	43
4.5	Day 1000 to day 2000 temporal mean fields for case $\Omega 0.0$. (a) Surface pressure (color shading) [Pa] and horizontal wind vectors [m s^{-1}] at the lowest level. Contour interval of surface pressure is 5×10^2 Pa, and the unit vectors of zonal and meridional wind are 20 m s^{-1} . (b) Horizontal wind vector [m s^{-1}] and geopotential [J kg^{-1}] at $\sigma = 0.17$. Unit vector indicates 25 m s^{-1} . Contour interval of geopotential is 500 J kg^{-1} . (c) Vertical wind $-\dot{\sigma}$ [s^{-1}] and zonal wind [m s^{-1}] (vector), and temperature [K] (color) in the equatorial vertical section. Unit vectors of vertical wind and zonal wind are $1.67 \times 10^{-5} \text{ s}^{-1}$ and 50 m s^{-1} , respectively. Contour interval of temperature is 5 K. (d) Specific humidity at the equator. Contour interval is 2×10^{-3} . (e) Condensation heating [W m^{-2}]. Color interval is 50 W m^{-2} . White area represents heating over 2000 W m^{-2} . (f) Horizontal distribution of surface evaporation [W m^{-2}]. Color interval is 50 W m^{-2} . (g) Vertically integrated water vapor flux [m s^{-1}] and vertically integrated water vapor mass [kg m^{-2}]. Unit vector is 0.3 m s^{-1} . Contour interval is 10 kg m^{-2} . (h) Surface temperature [K]. Contour interval is 5 K. From Noda et al. (2017), Fig. 5.....	45-46
4.6	Same as Fig. 4.5 but for case $\Omega 0.15$, except that the unit vector in (b) is 50 m s^{-1} and the unit vector of vertical wind in (c) is $2.5 \times 10^{-6} \text{ s}^{-1}$. From Noda et al. (2017), Fig 6.....	48
4.7	Mass weighted global mean zonal wind velocity for cases with Ω^* from 0.0 to 0.33 (circles). Absolute value of westward phase velocity of the zonal wavenumber one gravest Rossby normal mode is indicated by the thin line for comparison. From Noda et al. (2017), Fig. 7.....	50
4.8	Latitude--time distribution of zonal mean surface pressure [Pa] for (a) $\Omega 0.2$, (b) $\Omega 0.5$, (c) $\Omega 0.67$, and (d) $\Omega 0.75$. From Noda et al. (2017), Fig. 8.....	51
4.9	Same as Fig. 4.6 but for case $\Omega 0.75$, except that the unit vector of vertical wind in (c) is $1.3 \times 10^{-6} \text{ s}^{-1}$. From Noda et al. (2017), Fig. 9.....	53
4.10	Structure of the atmosphere averaged from day 1000 to day 2000 for case $\Omega 0.75$: (a) zonal mean zonal wind, and (b) eddy stream function at $\sigma = 0.17$. From Noda et al. (2017), Fig. 10.	54
4.11	Same as Fig. 4.9 but for case $\Omega 1.0$ except that unit vector of the vertical wind in (c) is $2.5 \times 10^{-6} \text{ s}^{-1}$. From Noda et al. (2017), Fig. 11.	56
4.12	(a) Ω^* dependences of outgoing longwave radiation on the night side, F_{OLR} (\circ), day-night dry static energy transport per unit area, $T_{sens} / (2 \pi R_p^2)$ (black triangle), and day-night latent energy transport per unit area, $T_{lat} / (2 \pi R_p^2)$ (\times). Units are [W m^{-2}]. All 10 runs for each Ω^* case are plotted. Blue and red lines represent ensemble averages for the small- Ω and the large- Ω branches, respectively. (b) Same as (a) but for global mean (\circ), day side mean (\times), and night side mean (Box) of surface temperature [K]. From Noda et al. (2017), Fig. 12.	58
4.13	Relationships between surface temperature and OLR obtained by the GCM and by the one-dimensional (vertical) radiative-convective equilibrium model. The GCM results are shown as colored dots: purple, light blue, green, and pink dots indicate runs $\Omega 0.0$, 0.15, 0.75, and 1.0, respectively. Data are from the grid points in the $120^\circ \times 120^\circ$ rectangular region centered on the subsolar point. Crosses in black circles indicate the values at the subsolar point. Black lines are the one-dimensional model results with tropospheric relative humidity of (in order from the top) 50, 60, 70, 80, 90, and 100 %, respectively. From Noda et al. (2017), Fig. 13.	60
4.14	Same as Fig. 4.7, but showing values for horizontal resolutions of T42 (squares) and T85 (triangles) in addition to those for T21 (circles). From Noda et al. (2017), Fig. A.2.	61
4.15	(a), (b) Same as Fig. 4.4c but for the T42 model (a) and T85 model (b), and (c), (d) same as Fig. 4.4d but for the T42 model (c) and T85 model (d). From Noda et al. (2017), Fig. A.1.	62

4.16	Mean surface pressure distributions for $\Omega_{0.6}$ in the T42 model (a) and T85 model (b) for 500 days during which high (low) pressure occupies the north (south) pole. From Noda et al. (2017), Fig. A.3.	63
------	--	----

Chapter 5

5.1	(a) Relationship between Ω^* and global mean OLR, (b) Relationship between Ω^* and solar constant divided by 4.0. The squares and circles represent the cases in which equilibrium states were obtained. The crosses represent the case in which the runaway greenhouse state emerged. The red marks represent the cloudy case with synchronously rotating planet distribution of solar flux. The blue marks represent the cloudy case with Earth-like distribution of solar flux. The yellow marks represent the cloud-free case with synchronously rotating planet distribution of solar flux. The green marks represent the cloudy case with Earth-like distribution of solar flux.	68
-----	---	----

List of Tables

Chapter 3

3.1	Values of the parameters used in this section.....	19
3.2	The list of experiments and the values of the solar constant. SSR is the shortwave radiation flux incoming on the surface. White circles indicate the case where the model atmosphere reaches a thermally equilibrium state, while cross marks indicate the cases where it does not. For details, see the description in Section 3.3. From Ishiwatari et al. (2002), Table 3.	20
3.3	Position of the vertical grid points used in section: k is the index of vertical level; σ_k and $\sigma_{(k+1/2)}$ indicate integer and semi-integer grids, respectively. Horizontal wind, temperature and specific humidity are evaluated at the integer grids, while vertical wind is evaluated at the semi-integer grids. From Ishiwatari et al. (2002), Table 2.	21

Numerical studies on the variety of climates of exoplanets using idealistic configurations

**Masaki Ishiwatari ¹, Kensuke Nakajima ², Shin-ichi Takehiro ³,
Yuta Kawai ⁴, Yoshiyuki O. Takahashi ⁵, George L. Hashimoto ⁶,
Youhei Sasaki ⁷ and Yoshi-Yuki Hayashi ⁵**

¹ Graduate School of Science, Hokkaido University,

² Graduate School of Science, Kyushu University,

³ Research Institute for Mathematical Studies, Kyoto University,

⁴ Computational Climate Science Research Team, RIKEN AICS,

⁵ Graduate School of Science, Kobe University,

⁶ Graduate School of Natural Science and Technology, Okayama University,

⁷ Faculty of Science and Engineering, Setsunan University

Abstract

This monograph summarizes the results of our numerical works so far on the variety of climates caused by changes in the value of solar constant and the horizontal distribution of incoming solar radiation flux. Our aim was to examine the mechanisms causing drastic changes in climate, such as the disappearance of oceans. For this aim, the following two studies were performed using the CGER supercomputer system.

One of our studies is an investigation of the dependence of the climate on the solar constant. Numerical experiments using a general circulation model (GCM) adopting a gray radiation scheme, aquaplanet condition, and cloud-free condition, were performed. The results imply that there exists an upper limit of the outgoing longwave radiation (OLR) even in a three-dimensional system, including the effects of spherical geometry and atmospheric motion, just like in vertical one-dimensional systems. The value of the upper limit of OLR corresponded to the radiation limit calculated by the one-dimensional radiative-convective equilibrium model with the relative humidity considered. In the three-dimensional system, the runaway greenhouse state appeared when the global mean incoming flux exceeded the upper limit of OLR.

The other of our studies is an investigation of the circulation structure of synchronously rotating planets that have a peculiar distribution of incoming solar radiation flux, i.e., a distribution with a perpetual dayside and nightside. A numerical experiment using a GCM adopting a gray radiation scheme, aquaplanet condition, and cloud-free condition was performed with the value of planetary rotation rate varied from zero to that of the Earth. The value of solar constant was set to be Earth's value. The results showed that the atmosphere reached statistically equilibrium states for all runs; none of the calculated cases exemplified the runaway greenhouse state. The circulation patterns obtained were classified into four types: Type-I characterized by the dominance of a day-night thermally direct circulation, Type-II characterized by a zonal wavenumber one resonant Rossby wave over a meridionally broad westerly jet on the equator, Type-III characterized by a long time scale north-south asymmetric variation, and Type-IV characterized by a pair of mid-latitude westerly jets. Despite the substantial changes in circulation, the net energy transport from the dayside to the nightside remained almost insensitive to the planetary rotation rate. The reason for this notable insensitivity is that the outgoing longwave radiation over a broad area of the dayside was constrained by the radiation limit of a moist atmosphere, so that the transport to the nightside, which was determined as the difference between the incoming solar radiation and the radiation limit, could not change greatly.

The common conclusion obtained from the above two investigations is that the existence of an upper limit of OLR is an important factor in determining the climate state. The existence of an upper limit of OLR is also shown in a preliminary experiment using GCM including a non-gray radiation scheme and a simple cloud model. The results obtained in our studies will be a basic concept for considering the variety of planetary climates.

Keywords:

exoplanets; synchronously rotating planets; runaway greenhouse state; globally ice-covered state; radiation limit; aquaplanet; general circulation model

Chapter 1

Introduction

This monograph summarizes the results of our works so far on the variety of climates using idealistic model configurations including those assuming exoplanets. Exoplanets are planets that exist around stars outside our solar system. Astronomical exploring observations so far have discovered over 4000 exoplanets¹. The observational results show that exoplanets are under different conditions from those of the planets in our solar system: for example, the host star has a luminosity different from Sun's value, and the semi-major axes of planets are much smaller than those of the planets of our solar system, and so on. Observations with space telescopes have found over 20 exoplanets that are considered to have liquid water on their surfaces and to be able to harbor life. Such planets are called habitable planets. Future observational missions such as the James Webb Space Telescope (<https://jwst.nasa.gov>) are expected to discover many habitable exoplanets. Based on this background, many climate predictions of terrestrial-type exoplanets have been performed (e.x., Heng and Vogt, 2011; Wordsworth et al., 2011). Especially, the existence conditions of liquid water on planet surfaces are focused. Such studies are not only expected to be extended to examinations of the habitability of exoplanets but are also expected to give new knowledge on the behavior of the atmosphere of planets under conditions different from Earth's. Thus, research on exoplanet climates poses new problems for climate research.

In recent years, numerical simulations of the climates of exoplanets that were discovered by astronomical observations have been attempted by some research groups using sophisticated models. When more possible climates are considered due to the increase in discoveries of terrestrial exoplanets by future missions, it will be desirable to acquire a general understanding of the maintenance mechanism and existence condition of each climate state in addition to simulations of the climate of particular exoplanets. Based on a general understanding, it will be possible to discuss the stability of each climate to the changes in external conditions, such as orbital parameters and stellar flux, and thus, the possibility of the long-term existence of liquid water on planet surfaces. As a basic theoretical framework for acquiring a general understanding, simple models that include necessary processes represented roughly can be useful. They enable us to perform parameter experiments covering a wide parameter range and can provide basic concepts for considering various climates.

We attempted to construct a possible basic theoretical framework for the general understanding of the variety of climates by examining the variety of climates of aquaplanets with grey atmosphere. A model with a gray radiation scheme cannot provide correct radiation fields like a sophisticated model but can numerically explore climates under various conditions by including the greenhouse effect and atmospheric circulation. Using an aquaplanet GCM with a gray radiation scheme, we have examined the variety of climates of aquaplanets with grey atmosphere and the mechanisms causing drastic changes in climate, such as the disappearance of oceans, using model configurations different from Earth's conditions (Supercomputer Annual Report since 2000 to 2020). Our studies are related to two problems described in the following subsections 1.1 and 1.2. In these studies, we have examined the dependencies of climate on the solar constant and horizontal distribution of incoming solar radiation flux. Although a part of the results was obtained from a paper published about twenty years ago, it provides a theoretical framework necessary for the investigation of the climate of exoplanets. We believe that it is valuable to summarize these results as a monograph.

¹ <https://exoplanetarchive.ipac.caltech.edu>

1.1 Drastic climate change caused by the change of the solar constant: occurrence of the runaway greenhouse state

The solar constant is one of the most important parameters that determine the climate of terrestrial planets. A state with oceans on the planetary surface like that of the present Earth vanishes when the value of solar constant changes by several tens of percent and the runaway greenhouse state emerges with an increased solar constant (Ishiwatari et al., 2002).

The runaway greenhouse state is the nonequilibrium atmospheric state which occurs when the incoming solar flux exceeds the limit value of outgoing longwave (infrared) radiation (OLR) of an atmosphere with a sufficient amount of liquid water on its bottom surface, as shown in Fig. 1.1 (Nakajima et al., 1992, hereafter referred to as NHA92). There are two different types of OLR limit. NHA92 clarifies them using a one-dimensional radiative-convective equilibrium model in which the atmosphere is transparent to shortwave radiation and gray to longwave radiation. One of the OLR limits is the limit constrained by the radiation flux going through the stratosphere. This limit is referred to as the Komabayashi-Ingersoll limit, since it is the key mechanism that causes runaway greenhouse states in the stratospheric models of Komabayashi (1967) and Ingersoll (1969). The other is the limit constrained by the emissivity of the troposphere. The limit of OLR that appears in a radiative-convective equilibrium model is the lower of these two. When the incoming flux exceeds the lower OLR limit, the atmospheric temperature will continue to rise until all the oceans evaporate. The runaway greenhouse state is often discussed in studies on the atmospheric evolution of Earth and Venus (Pollack, 1971; Abe and Matsui, 1988; Kasting, 1988).

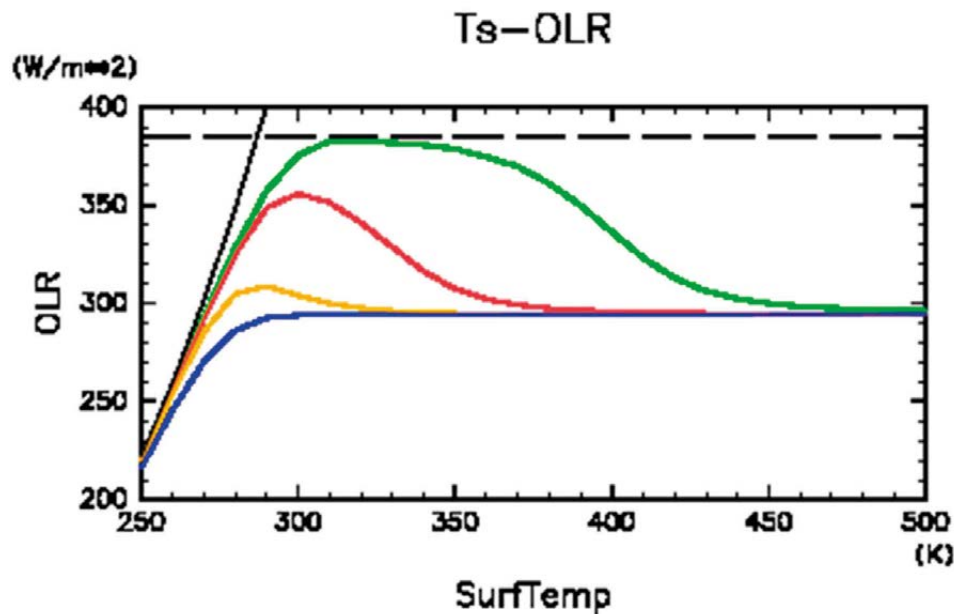


Figure 1.1 Relationships between surface temperature and OLR for gray atmosphere. The black solid line shows σT_s^4 . Other solid lines represent equilibrium solutions obtained by the vertical one-dimensional radiative-convective model. The green, red, orange, and blue lines represent the results for $p_{n0}=10^6, 10^5, 10^4, 0$ Pa, respectively. p_{n0} is the partial pressure of dry air at the surface. The solid dashed-line represents the Komabayashi-Ingersoll limit obtained by the stratosphere model. Modified from Ishiwatari (2014), Fig. 1.

As described above, the runaway greenhouse state had been discussed only by vertical one-dimensional models until around the year 2000. Ishiwatari et al. (1998, 2002) examined, for the first time, the occurrence condition of the runaway greenhouse state in a three-dimensional system. In Chapter 3, we describe the results of Ishiwatari et al. (2002).

1.2 Circulation structures of planets with a peculiar distribution of solar flux

Synchronously rotating planets are planets that exist near a central host star and have the same rotation period as the orbital period due to strong tidal force. Since a particular hemisphere always faces the central star, they have a peculiar distribution of incoming flux with a perpetual dayside and nightside. Some potentially habitable exoplanets that have been discovered are synchronously rotating planets (Fig. 1.2: Von Bloh et al., 2007). Much more exoplanets are expected to be discovered by future missions. Therefore, synchronously rotating planets are an important scientific target for considering the habitability of exoplanets.

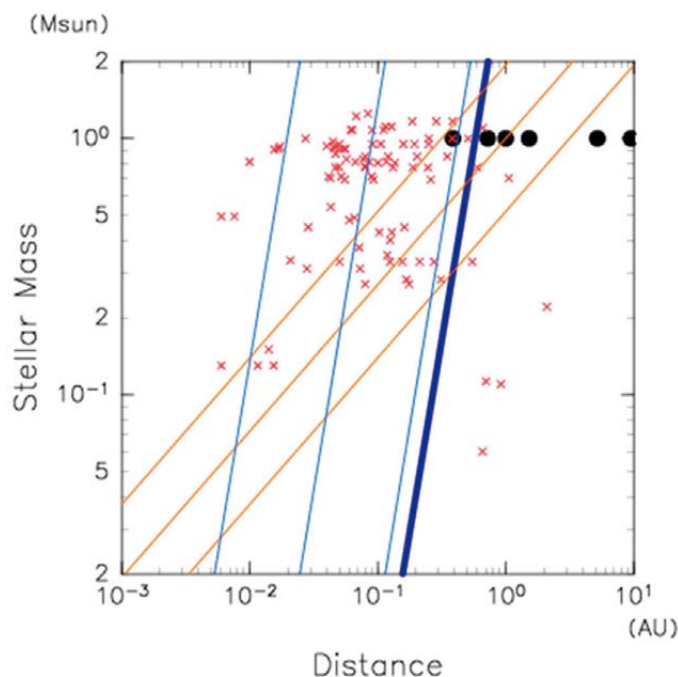


Figure 1.2 Small-mass exoplanets discovered by astronomical missions. The ordinate is the mass of the central host star and the abscissa is the semi-major axis. Red crosses represent exoplanets discovered until 2014 with a mass smaller than ten times of Earth's mass. The data were obtained at <http://exoplanet.eu>. Large black dots represent planets in the solar system. Orange lines represent 10.0, 1.0, and 0.1 times of Earth's solar constant. Thin blue lines represent 1 day, 10 days, and 100 days of the orbital period. The thick blue line represents the tidal lock radius inside which planets are considered to be synchronously rotating planets.

Even when the global mean incoming heat flux from the central star is comparable to that of the present Earth, the incoming flux on the perpetual dayside of a synchronously rotating planet can easily exceed the upper limit of OLR that a moist atmosphere can emit (NHA92). So, a synchronously rotating planet may easily enter the runaway greenhouse state if the dayside to nightside (hereafter, day-night) energy transport is insufficient. Contrary to the above naive speculation, in previous studies on atmospheres of synchronously rotating planets using general circulation models (GCMs), the runaway greenhouse state did not emerge for several different values of planetary rotation rate with the present value of the Earth's solar constant (e.g., Joshi et al., 1997; Joshi, 2003; Merlis and Schneider, 2010; Edson et al., 2011). However, in these previous studies, the mechanism that determines the amount of day-night energy transport remains to be understood and its dependence on the planetary rotation rate to be revealed. To consider these problems, Noda et al. (2017) investigated atmospheric circulation structures and day-night energy transports by performing parameter experiments for various values of planetary rotation rate. The results are presented in Chapter 4.

1.3 Contents of this monograph

The contents of this monograph are organized as follows. In Chapter 2, we briefly describe our general circulation models. In Chapter 3, we show that the occurrence condition of the runaway greenhouse state in cloud-free gray atmosphere can be described by the results obtained by a vertical one-dimensional model. In Chapter 4, we discuss the circulation structure of synchronously rotating planets. Chapter 5 presents the preliminary results of experiments in which a non-gray radiation scheme and a simple cloud model were used. The summary of this monograph is found in Chapter 6.

Chapter 2

Model description

2.1 Basic assumptions

In order to examine the variety of climates of aquaplanets whose entire surface is covered with the ocean, we used a simple setup. In our studies, moist atmospheres were considered. Based on this configuration, we used atmospheric general circulation models (AGCMs).

2.2 An overview of GCMs

In the following chapters, two GCMs are used. The GCM utilized in Chapter 3 is AGCM5.3 of GFD DENNOU CLUB¹. As described in Section 3.6, a model bug was found in AGCM5.3 in the year 2019. We are now planning to perform a re-experiment with DCAPM5 described below and the results will be updated. In this monograph, we describe the results and discussions obtained by using AGCM5.3, including the model bug. We expect that the results will be qualitatively unchanged in our future re-experiment. The GCM utilized in Chapters 4 and 5 is DCPAM5 of GFD DENNOU CLUB (Dennou-Club Planetary Atmospheric Model)². It has been developed by reconstructing AGCM5.3 to investigate the possible variety of general circulations of atmospheres of terrestrial planets in general.

Both GCMs are three-dimensional primitive systems on a sphere. The following are common descriptions of AGCM5.3 and DCPAM unless either of the two models is specified.

2.3 Discretization

The equations were discretized horizontally by using a non-alias latitude-longitude grid and integrated using the spherical spectral transform method. We used σ as the vertical coordinate, which was discretized by following the method of Arakawa and Suarez (1983). The time integration was performed by using a leap-frog scheme for the terms of dynamical processes other than dissipative processes, a backward scheme for the terms of physical processes, and an Euler scheme for the horizontal diffusion terms. The time filter of Asselin (1972) was used to remove the computational mode caused by the leap-frog scheme. In Chapter 5, the advection of water vapor and cloud water was calculated with the semi-Lagrangian scheme of Kashimura et al. (2013).

2.4 Atmospheric constituents and radiation processes

The following two types of atmospheric constituents and related radiation processes were assumed. In all cases, atmospheric gases behaved as ideal gases.

- (1) The atmosphere consists of a condensable component (water vapor) and a non-condensable component (dry air).

As for longwave radiation, we included only the absorption and emission of water with a constant absorption coefficient ($0.01 \text{ m}^2 \text{ kg}^{-1}$). The effect of scattering was not included. Dry air was assumed to be transparent; radiatively active non-condensable gases

¹ <https://www.gfd-dennou.org/library/agcm5/index.htm.en>

² <https://www.gfd-dennou.org/library/dcpam/index.htm.en>

such as ozone or carbon dioxide were excluded.

- (2) The atmosphere consists of CO₂, water vapor, and N₂, which are constituents of Earth's atmosphere.

As for the radiation processes, the schemes of Chou and Lee (1996) and Chou et al. (2001) were used. In these schemes, the absorption of longwave radiation and shortwave radiation by water vapor, CO₂, and clouds were considered. For evaluating the scattering of shortwave radiation, Rayleigh scattering was assumed.

2.5 Physical processes other than radiation processes

- Cumulus parameterization

For case (1) described in Section 2.4 (case for gray radiation), the moist convective adjustment scheme of Manabe et al. (1965) was used. Condensed water was immediately removed from the atmosphere as rain.

For case (2) described in Section 2.4 (case for Earth radiation), the relaxed Arakawa-Schubert scheme (Moorthy and Suarez, 1992) was used.

- Cloud water

For case (1) described in Section 2.4 (case for gray radiation), absorption and scattering of radiation by clouds were not incorporated.

For case (2) described in Section 2.4 (case for Earth radiation), the amount of cloud water was calculated by solving the time-dependent equation including the terms of cloud water generation calculated from the cumulus scheme, advection, turbulent diffusion, and extinction, which was assumed to be proportional to the amount of cloud water and was given an extinction time.

- Vertical mixing

Vertical turbulent mixing was represented by the level II scheme of Mellor and Yamada (1974).

- Surface flux

For case (1) described in Section 2.4 (gray radiation case), the surface fluxes of momentum, sensible heat, and latent heat were evaluated with bulk formulas, the bulk coefficients of which were evaluated by following Louis (1979).

For case (2) described in Section 2.4 (case for Earth radiation), the surface fluxes were evaluated by using the method of Beljaars and Holtslag (1991).

2.6 Surface conditions

The entire surface was assumed to be a “swamp ocean”; heat capacity was zero and the wetness was uniform (Delworth and Manabe, 1988). Heat transport by the ocean was excluded. The value of surface albedo was fixed to a constant value regardless of the value of surface temperature.

2.7 Model modification for experiments with increased solar constant

The atmospheric structure expected to be realized in the runaway greenhouse state required the following modifications of the model. The change in the total atmospheric mass had to be taken into account. A significant increase in water vapor amount was anticipated in the states with an increased solar constant. The change in the total atmospheric mass was evaluated with a surface pressure correction by the amount corresponding to the difference between evaporation and precipitation. Moreover, the model top had to be taken to a higher level, since the tropopause goes up to a higher level in experiments with an increased solar constant. In models with a higher top level, a numerical instability problem related to internal gravity waves occurs. In order to suppress the numerical instability, an upper damping layer and a vertical filter had to be introduced for some runs. The following is a detailed description of each model modification for the experiments with an increased solar constant.

2.7.1 p_s change due to evaporation and condensation

The atmospheric mass varies with the evaporation and condensation (precipitation) of water vapor. We have considered only the total variation of the mass of the vertical column at each grid point and evaluated the correction of surface pressure p_s and specific humidity q after the integration of each time step.

The correction of surface pressure Δp_s for each time step was calculated as follows (Ishiwatari et al., 2002):

$$\Delta p_s = F_{evap} \frac{g}{L} \Delta t + \hat{p}_s \int S_q^{cond} \Delta t d\sigma \quad (1)$$

The first term on the right-hand side describes the water vapor increase by evaporation and the second term describes the water vapor decrease by condensation. The value F_{evap} is the evaporative latent energy flux at the surface, Δt is the time step, S_q^{cond} is the tendency of specific humidity due to condensation, and \hat{p}_s is the surface pressure before correction.

The correction of the specific humidity was calculated by using the conservation of the mass of water vapor. The mass of water vapor should be conserved through the correction of q as follows,

$$\hat{\rho} \hat{q} = \rho q \quad (2)$$

where $\hat{\rho}$, \hat{q} are density and specific humidity, respectively, before correction, and ρ , q are those after correction. From this equation, the corrected specific humidity q is

$$q = \frac{\hat{p}_s}{\hat{p}_s + \Delta p_s} \hat{q} \quad (3)$$

2.7.2 Upper damping layer

For cases with an increased solar constant and a higher model top level, we encountered a numerical instability problem due to the amplification of internal gravity waves in the

uppermost region. In some runs described in the next chapters, we introduced a strong artificial dissipation to suppress the internal gravity waves in the upper levels. The artificial dissipation consisted of Newtonian cooling, Rayleigh damping, and a vertical filter. The vertical filter is described in section 2.7.3 below.

The Newtonian cooling adjusts temperature T to its zonal mean value. The Rayleigh friction damps the horizontal wind (u, v) toward 0. It was introduced to the seven levels from the top level of the model. The time constants of the Newtonian cooling and Rayleigh damping were set to be 10800 s at the uppermost level. The time constants increased downwards; the value at the seventh level from the top was 75600 s.

2.7.3 Vertical filter

In addition to the damping layer described in the previous section, a vertical filter was introduced for T to suppress the growth of the 2-grid noise. The filter utilized was similar to that of Shapiro (1971). Since the original form of the Shapiro filter does not conserve the total energy, we modified the filter in the following way to satisfy energy conservation. This modification was especially important in the experiments where the runaway greenhouse state emerged (Ishiwatari et al., 2002).

We determined a reference state first by using the values at half-integer grid points $T_{k+\frac{1}{2}}$, which were calculated in the model for the use of the radiation process.

$$T_{B,k} \equiv \frac{T_{k+\frac{1}{2}} + T_{k-\frac{1}{2}}}{2} \quad (4)$$

The temperature profile was then smoothed toward this reference state. From the bottom ($k=2$) to the top ($k=31$), the following scheme was applied.

$$T_{k-1} = \widehat{T}_{k-1} + F_T (T_{B,k-1} - T_{k-1}) - \frac{\sum_{k'=k-1}^{k+1} F_T (T_{B,k'} - \widehat{T}_k) \Delta p_{k'}}{\sum_{k'=k-1}^{k+1} \Delta p_{k'}} \quad (5)$$

$$T_k = \widehat{T}_k + F_T (T_{B,k} - T_k) - \frac{\sum_{k'=k-1}^{k+1} F_T (T_{B,k'} - \widehat{T}_k) \Delta p_{k'}}{\sum_{k'=k-1}^{k+1} \Delta p_{k'}} \quad (6)$$

$$T_{k+1} = \widehat{T}_{k+1} + F_T (T_{B,k+1} - T_{k+1}) - \frac{\sum_{k'=k-1}^{k+1} F_T (T_{B,k'} - \widehat{T}_k) \Delta p_{k'}}{\sum_{k'=k-1}^{k+1} \Delta p_{k'}} \quad (7)$$

where \widehat{T}_k is the temperature before the filter is applied. The value F_T is a coefficient that describes the intensity of the filter. We utilized $F_T = 0.1$ in our numerical experiments. The third term of the left-hand side in each equation is the correction of the internal energy loss. The energy loss owing to the Shapiro-type filter was distributed equally within each three-layer group.

For the cases in which the numerical instability could not be suppressed only by a vertical filter on the temperature fields, we applied a vertical filter also to the horizontal wind field. The filter for the wind field was the same as that of Shapiro (1971). We have set the intensity parameter of the filter at 0.1.

Chapter 3

Occurrence condition of the runaway greenhouse state in a three-dimensional system

This chapter is based on “Ishiwatari M., Takehiro S., Nakajima K., Hayashi Y.-Y. (2002) A Numerical Study on Appearance of the Runaway Greenhouse State of a Three-Dimensional Gray Atmosphere. Journal of the Atmospheric Sciences 59(22):3223-3238,” ©American Meteorological Society. Used with permission.

3.1 Introduction

In this section, we consider occurrence of the runaway greenhouse state of a three-dimensional spherical atmosphere in the theoretical framework established by the one-dimensional model of NHA92. Results and discussions of in this section are based on Ishiwatari et al. (1998, 2002) that is the first attempt to perform three-dimensional calculations of the appearance of the runaway greenhouse state. For three-dimensional system with meridionally non-uniform incoming solar flux and atmospheric circulations, the following two problems are examined:

- (I) Whether there exists an upper limit of the solar constant value?
- (II) If an upper limit exists, what determines the occurrence condition of the runaway greenhouse state?

The adopted configuration of the GCM is the most basic one; cloud-free atmosphere, gray radiation, swamp ocean and so on. The adopted framework is, except for the incorporation of three-dimensional atmospheric motion, basically equivalent to the one-dimensional radiative-convective equilibrium model of Nakajima et al. (1992) in which the existence of radiation limits is clarified and the runaway greenhouse state is described in terms of radiation limits. Using the swamp condition allows the system to reach a statistically equilibrium state in a shorter time than with a slab ocean and is convenient for execution of a large number of runs with a number of experiments.

We should notify that a critical model bug was found in GCM used by Ishiwatari et al. (2002). The details are described in Section 3.6. Although quantitative changes in temperature field or zonal mean field will emerge by fixing the model bug, we consider that our main result of this chapter are not changed qualitatively. Therefore, we present the results of Ishiwatari et al. (2002) in the followings.

3.2 Model configuration

As for atmospheric constituent and radiation process, case (1) (case for gray radiation) described in Section 2.2.3 is adopted. We assume that specific heat and molecular weight of water vapor are the same as dry air so that those of the atmosphere are independent of the specific humidity (mass ratio of water vapor to entire air parcel). According to NHA92, this simplification does not alter the fundamental thermodynamical structure for the occurrence of the runaway greenhouse state. This assumption makes the density of model atmosphere smaller compared to the reality, and hence the intensity of circulation may be increased. Although the difference of density does not alter equations of motion in the σ coordinate, it causes some changes in energy equation. We have assumed that the difference of circulation intensity caused by this simplification is small and the dynamical structure of the system, for instance --- existence of runaway state--- does not change. Due to the above configurations, the system utilized is basically the same as that of the one-dimensional radiative-convective equilibrium model of NHA92, except for the inclusion of atmospheric three-dimensional spherical motion. The surface albedo can be set to zero. All of the planetary surface is assumed to be “swamp ocean.”

The values of the model parameters are listed in Table 3.1. Planetary rotation rate Ω * normalized by Earth's value, $7.272 \times 10^{-5} \text{ s}^{-1}$, is set to be 1.0.

Table 3.1 Values of the parameters used in this section.

Parameters of model	Value
Latent heat of water vapor	$L=2.4253 \times 10^6 \text{ J kg}^{-1}$
Partial pressure of dry air at the bottom of atmosphere	$p_{n0}=10^5 \text{ Pa}$
Absorption coefficient of water vapor	$\kappa_v=0.01 \text{ m}^2 \text{ kg}^{-1}$
Absorption coefficient of dry air	$\kappa_n=0 \text{ m}^2 \text{ kg}^{-1}$
Radius of planet	$a=6.37 \times 10^6 \text{ m}$
acceleration of gravity	$g=9.81 \text{ m s}^{-2}$
global mean surface pressure	$\bar{p}_s=10^5 \text{ Pa}$

As listed in Table 3.2, eight experiments are performed with different values of solar constant S . Each experiment is referred to as a letter S followed by the value of solar constant specified in the experiment. Experiment S1380 is the case corresponding to the present earth. Since all of the shortwave radiation is assumed to reach the ground surface, the global mean value of incoming shortwave radiation at the surface (SSR) is equal to $S/4$.

The distribution of incoming solar flux is given by the annual and daily average evaluated with the present terrestrial orbital parameters. The diurnal and seasonal cycles are not considered. The meridional distributions of the solar flux are shown in Fig. 3.1.

The initial condition is the same for all experiments. It is a resting, isothermal (280K) atmosphere with a constant specific humidity (10^{-3}). For each experiment, the model is integrated over 1000 days during which the atmosphere reaches a thermally equilibrium state, if it can. The horizontal resolution utilized in the present study is 32×64 that corresponds to spectral truncation T21. The atmospheric structure expected to be realized in the runaway greenhouse state requires the increased number of the vertical levels in the upper atmosphere. The tropopause must be allowed to reach a very high altitude level. Correspondingly, we specify that the uppermost vertical grid is located at $\sigma=10^{-6}$ and the total number of levels is 32 (Table 3.3). This configuration of the model vertical levels ensures the accuracy of 5 W m^{-2} in the OLR calculation throughout the parameter range considered in NHA92. In order to perform experiment with increased solar constant, upper damping layer described in Section 2.7.2 is used. Time constant of the Newtonian cooling is set to be 10800 s at the uppermost level. The time constants increase downwards; the value at the seventh level from the top is 75600 s. Vertical filter is also used as in shown in Table 3.2. We utilize coefficient $F_T = 0.1$ for temperature vertical filter.

Table 3.2 The list of experiments and the values of the solar constant. SSR is the shortwave radiation flux incoming on the surface. White circles indicate the case where the model atmosphere reaches a thermally equilibrium state, while cross marks indicate the cases where it does not. For the details, see the description in Section 3.3. From Ishiwatari et al. (2002), Table 3.

Experiment name	Global mean SSR (W m^{-2})	Variables smoothed by vertical filter	Notes
S1200	300.0	T	○
S1380	345.0	T	○
S1500	375.0	T,u,v	○
S1550	387.5	T,u,v	○
S1570	392.5	T,u,v	○
S1600	400.0	T,u,v	×
S1700	425.0	T,u,v	×
S1800	450.0	T,u,v	×

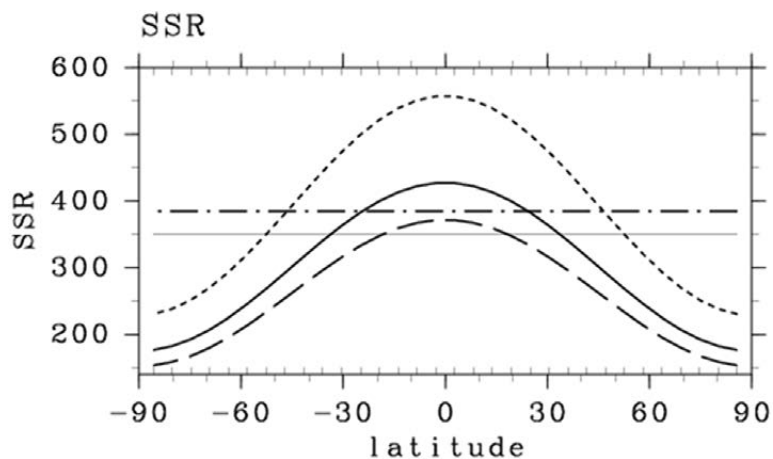


Figure 3.1 Meridional distributions of incoming solar radiation flux. Unit is W m^{-2} . Thick solid line, dashed line and dotted line are for $S=1380 \text{ W m}^{-2}$, $S=1200 \text{ W m}^{-2}$ and $S=1800 \text{ W m}^{-2}$, respectively. Dotted-dashed line indicates the Komabayashi-Ingersoll limit (385.2 W m^{-2}), and thin solid line indicates the upper-limit value of OLR (355.0 W m^{-2}) obtained by the NHA92 model. Both of them are calculated with the parameters of the present study. From Ishiwatari et al. (2002), Fig. 1.

Table 3.3 Position of the vertical grid points used in this section: k is the index of vertical level; σ_k and $\sigma_{(k+1/2)}$ indicate integer and semi-integer grids, respectively. Horizontal wind, temperature and specific humidity are evaluated at the integer grids, while vertical wind is evaluated at the semi-integer grids. From Ishiwatari et al. (2002), Table 2.

K	σ_k	$\sigma_{k+1/2}$
0		1
1	0.995	0.990
2	0.980	0.970
3	0.950	0.930
4	0.900	0.870
5	0.830	0.790
6	0.745	0.700
7	0.650	0.600
8	0.549	0.500
9	0.454	0.410
10	0.369	0.330
11	0.294	0.260
12	0.229	0.200
13	0.174	0.150
14	0.124	0.100
15	7.40×10^{-2}	5.00×10^{-2}
16	3.72×10^{-2}	2.54×10^{-2}
17	1.89×10^{-2}	1.29×10^{-2}
18	9.61×10^{-3}	6.58×10^{-3}
19	4.90×10^{-3}	3.34×10^{-3}
20	2.49×10^{-3}	1.70×10^{-3}
21	1.27×10^{-3}	8.65×10^{-4}
22	6.44×10^{-4}	4.40×10^{-4}
23	3.28×10^{-4}	2.24×10^{-4}
24	1.67×10^{-4}	1.14×10^{-4}
25	8.48×10^{-5}	5.78×10^{-5}
26	4.30×10^{-5}	2.94×10^{-5}
27	2.19×10^{-5}	1.50×10^{-5}
28	1.15×10^{-5}	7.60×10^{-6}
29	5.66×10^{-6}	3.87×10^{-6}
30	2.88×10^{-6}	1.97×10^{-6}
31	1.47×10^{-6}	1.00×10^{-6}
32	4.15×10^{-7}	0

3.3 Emergence of thermally runaway states

With GCM described in previous section, Ishiwatari et al. (2002) showed that thermally runaway states are obtained for increased solar constant. In the followings, we describe their results.

Fig. 3.2 shows the time evolution of global mean OLR and global mean surface temperature of experiments S1200, S1380, S1570 and S1800. As shown in Fig. 3.2a, for the cases with $S \leq 1570 \text{ W m}^{-2}$, the global mean OLR becomes equal to the global mean SSR, which is equal to $S/4$, in about 500 days, and the atmospheric system reaches a statistically steady state. The global mean surface temperature also settles down to an equilibrium value (Fig. 3.2b).

In the experiment S1800, on the other hand, the system goes into a thermally runaway state. The global mean surface temperature keeps increasing (dashed-dotted line in Fig. 3.2b). The atmosphere emits infrared radiation less than the incoming total solar flux, since the calculated value of global mean OLR is always less than 450 W m^{-2} (dashed-dotted line in Fig. 3.2a). Moreover, the global mean OLR decreases gradually as time goes on, and hence, the excess in the energy budget, that is, the difference between the given SSR and the global mean OLR, increases. The atmospheric system does not seem to approach any thermal equilibrium states.

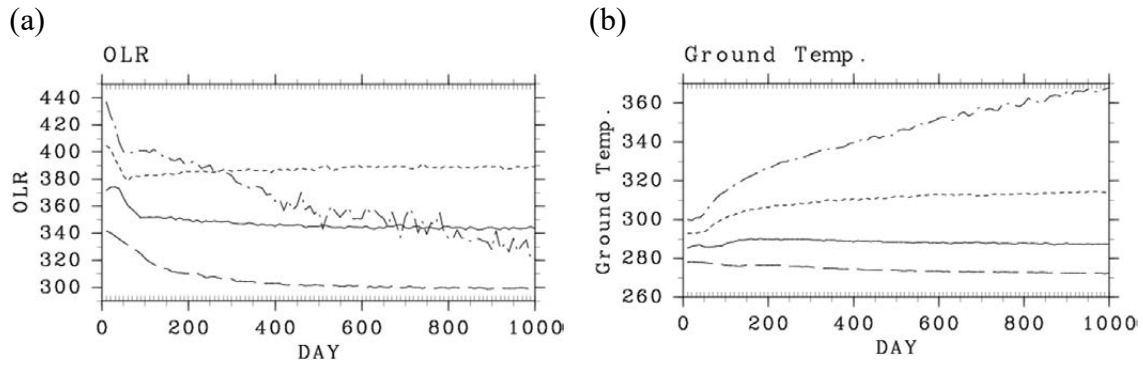


Figure 3.2 Time evolutions of (a) global mean OLR (W m^{-2}) and (b) global mean surface temperature (K). Dashed line, solid line, dotted line and dashed-dotted line indicate experiments S1200, S1380, S1570 and S1800, respectively. From Ishiwatari et al. (2002), Fig. 2.

Fig. 3.3 summarizes the relationship between the externally given global mean SSR and the global mean OLR obtained at the end of the time integration for all of the experiments. When $S < 1600 \text{ W m}^{-2}$, that is, the global mean SSR is less than 400 W m^{-2} , the global mean OLR almost exactly equals the global mean SSR, and the atmosphere reaches an equilibrium state. On the other hand, when $S \geq 1600 \text{ W m}^{-2}$, that is, the global mean SSR is 400 W m^{-2} or larger, the atmosphere cannot reach an equilibrium state. All of the results obtained with $S \geq 1600 \text{ W m}^{-2}$ are thermally runaway states characterized by continuous decrease of OLR and continuous increase of surface temperature, as is shown for the case of S1800 in Fig. 3.2.

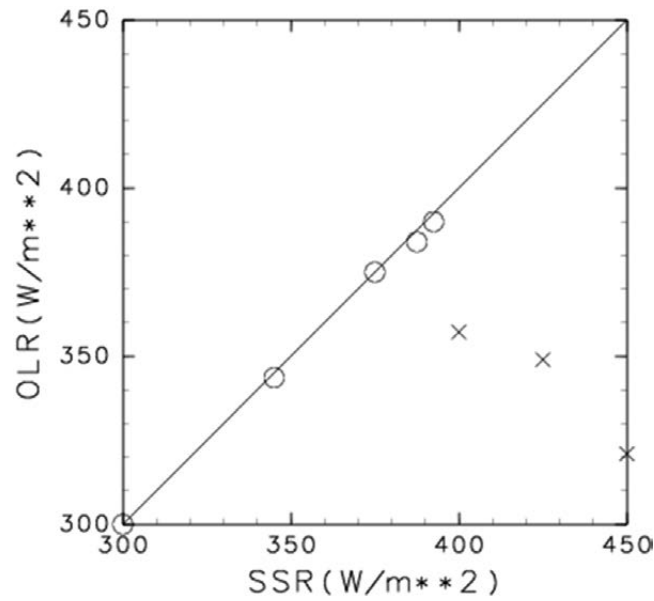


Figure 3.3 The relationship between global mean SSR and global mean OLR. The values of OLR at day 1000 are plotted except for S1600 where the value is at day 2000. White circles represent the cases where the atmosphere reaches an equilibrium state, while cross marks represent the cases where the atmosphere is in a thermally runaway state. Note that the values of OLR for thermally runaway states are continuously decreasing. From Ishiwatari et al. (2002), Fig. 3.

It is now confirmed that there exists an upper limit on the value of solar constant with which the three-dimensionally circulating atmosphere reaches a thermal equilibrium state. The value of the upper limit is about 1600 W m^{-2} , or 400 W m^{-2} as global mean SSR, in our configuration. In the following sections, we will examine the correspondence of the thermally runaway states obtained by the three-dimensional calculations with the runaway greenhouse state defined by the one-dimensional model of NHA92. An interpretation of the upper-limit value of the solar constant will also be given.

3.4 Comparison with a one-dimensional system

Fig. 3.4 shows the meridional distributions of zonal mean OLR and zonal mean surface temperature for the cases with $S \leq 1570 \text{ W m}^{-2}$ where the atmosphere can reach a thermal equilibrium state. As the incoming solar flux increases, the meridional distribution of OLR is flattened and the value of OLR approaches about 400 W m^{-2} at all latitudes. The value of OLR in the equatorial region ceases to increase at around 390 W m^{-2} when $S=1500 \text{ W m}^{-2}$ and the value hardly changes against the further increase of solar constant. In the mid- and high latitudes, the value of OLR gradually approaches 400 W m^{-2} with the increase of the solar constant. The tendency similar to that of OLR distribution appears in the meridional distribution of zonal mean surface temperature.

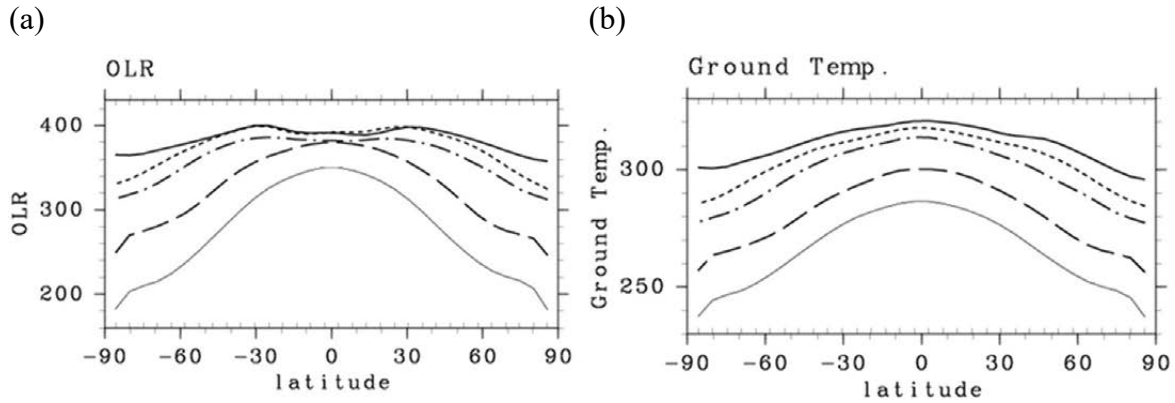


Figure 3.4 The meridional distributions of (a) zonal mean OLR (W m^{-2}) and (b) zonal mean surface temperature (K) of the cases in which the system reaches equilibrium states. Thick solid line, dotted line, dotted-dashed line, dashed line, and thin solid line indicate experiments S1570, S1550, S1500, S1380, and S1200, respectively. The data are temporally averaged between days 950 and 1000. From Ishiwatari et al. (2002), Fig. 4.

The asymptotic value of OLR is actually close to the upper limit of radiation which is constrained by the tropospheric temperature structure as discussed in NHA92. In order to apply the discussion by NHA92, it is necessary to examine the value of tropospheric relative humidity. In experiment S1570, the averaged value of relative humidity in the equatorial troposphere is about 60%. The upper limit of radiation obtained by the one-dimensional radiative-convective equilibrium model is 385 W m^{-2} when the value of relative humidity for the radiation scheme is fixed to be 60%. This value is close to 390 W m^{-2} , the equatorial value of OLR obtained in our three-dimensional calculations.

Now, we will compare the tropospheric temperature structures of the three-dimensional results with those of one-dimensional equilibrium solutions to examine whether there exists a tendency of the temperature field to approach an asymptotic profile as a function of optical depth as discussed by NHA92. Fig. 3.5 shows the temperature structures obtained by the one-dimensional radiative-convective equilibrium model in which relative humidity is fixed to be 60%. In Fig. 8a, where the temperature is plotted as a function of pressure, the asymptotic feature is not obvious; as surface temperature increases, the entire vertical profile is simply shifted to the positive direction of the temperature axis. However, in Fig. 8b, where the temperature is plotted as a function of optical depth, the temperature structures closely approach the curve determined by the saturation water vapor pressure. Especially, for the cases corresponding to S1600, S1700, S1800, the profiles almost coincide with each other. NHA92 pointed out that the existence of this asymptote is the essential feature for the appearance of runaway greenhouse state in the one-dimensional equilibrium model.

As for the three-dimensional results, the tropospheric temperature profiles as a function of optical depth τ also seem to have an asymptote (Fig. 3.6b), while the profiles as a function of pressure scatter just as one-dimensional equilibrium solutions (Fig. 3.6a). The existence of an asymptote can be observed in the deep troposphere of the thermally runaway states (experiments S1600, S1700, S1800), where $\tau \gg 1$. This is because the specific humidity there is fairly large as to ensure that temperature gradient almost coincides with that of the saturation vapor pressure curve.

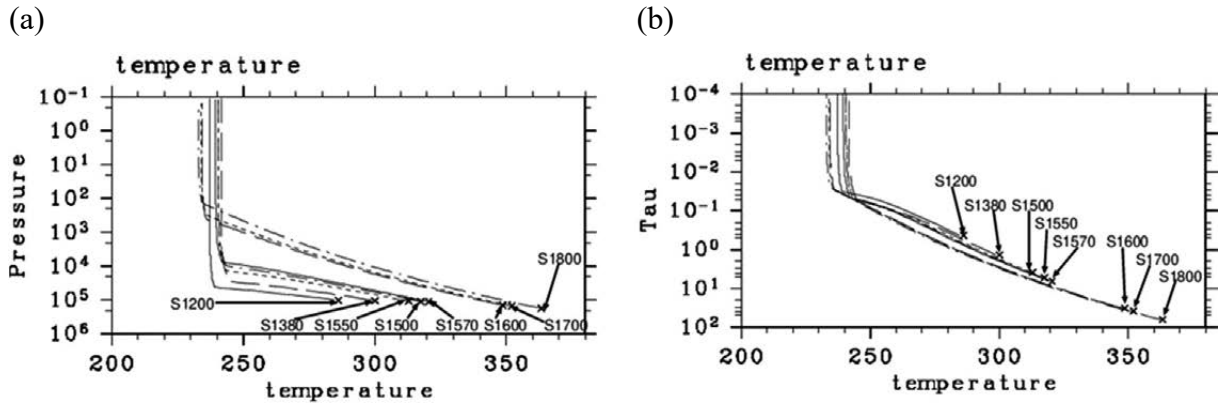


Figure 3.5 Vertical distributions of temperature obtained by one-dimensional model with relative humidity of 60% for the radiation scheme. The profiles are plotted by specifying the values of temperature at the bottom of atmosphere as those obtained by the experiments. Ordinates are (a) pressure (Pa) and (b) optical depth. Cross marks indicate surface temperature. From Ishiwatari et al. (2002), Fig. 5.

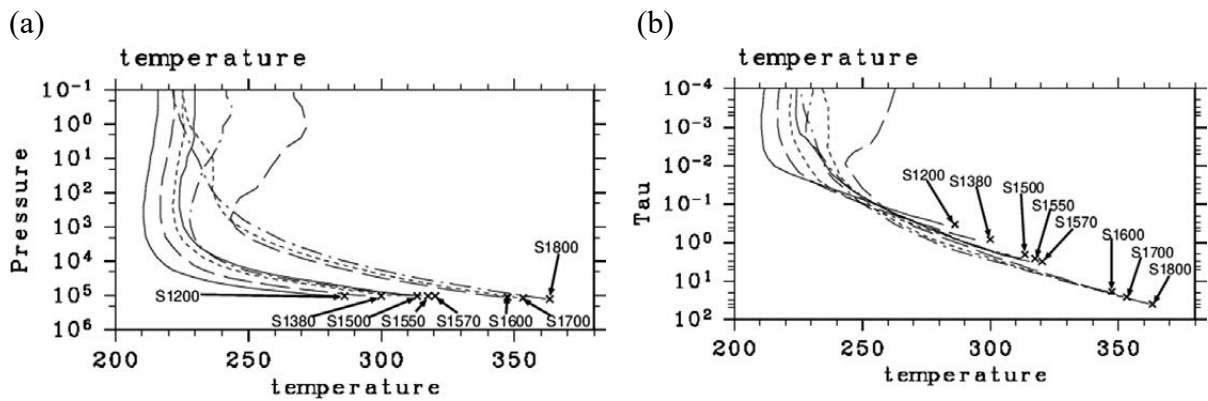


Figure 3.6 Vertical distributions of zonally averaged temperature at the equator for various values of solar constant. Ordinates are (a) pressure (Pa) and (b) optical depth. The profiles obtained in the experiments S1800, S1700, S1600, S1570, S1550, S1500, S1380, S1200 are plotted. Cross marks indicate surface temperature. From Ishiwatari et al. (2002), Fig. 6.

Fig. 3.7 shows the relationship between surface temperature and OLR obtained by the one-dimensional calculation similar to those given by NHA92 except that the value of relative humidity for the radiation calculation is varied between 40% and 100%. In Fig. 3.7, the points representing the equatorial zonal mean values of surface temperature and OLR obtained by the three-dimensional calculations are also plotted. The surface temperature-OLR relationship obtained by three-dimensional calculation is well correlated with the curve of the one-dimensional model with 60% relative humidity. There exists a slight difference. The causes of the difference are that the value of tropospheric relative humidity is larger than 60% in experiments S1200~S1500 and that the temperature gap between the surface and the lowest

level of the model, which is allowed in the three-dimensional model but not in one-dimensional calculations, becomes significant in experiments S1550 and S1570. In thermally runaway states (S1600, S1700, S1800), OLR decreases as the solar constant increases, since the relative humidity in the upper troposphere increases (not presented here).

As a result of the above discussion, it can be concluded that the asymptotic value of OLR obtained by three-dimensional calculations corresponds to the upper limit of radiation of the one-dimensional radiative-convective equilibrium solution in which the value of relative humidity is taken into account. The existence of the upper limit of OLR in the three-dimensional system means that the runaway greenhouse state can be defined also in three-dimensional system as the state realized when the incoming radiation exceeds the upper limit of OLR, that is, the runaway greenhouse state defined by NHA92.

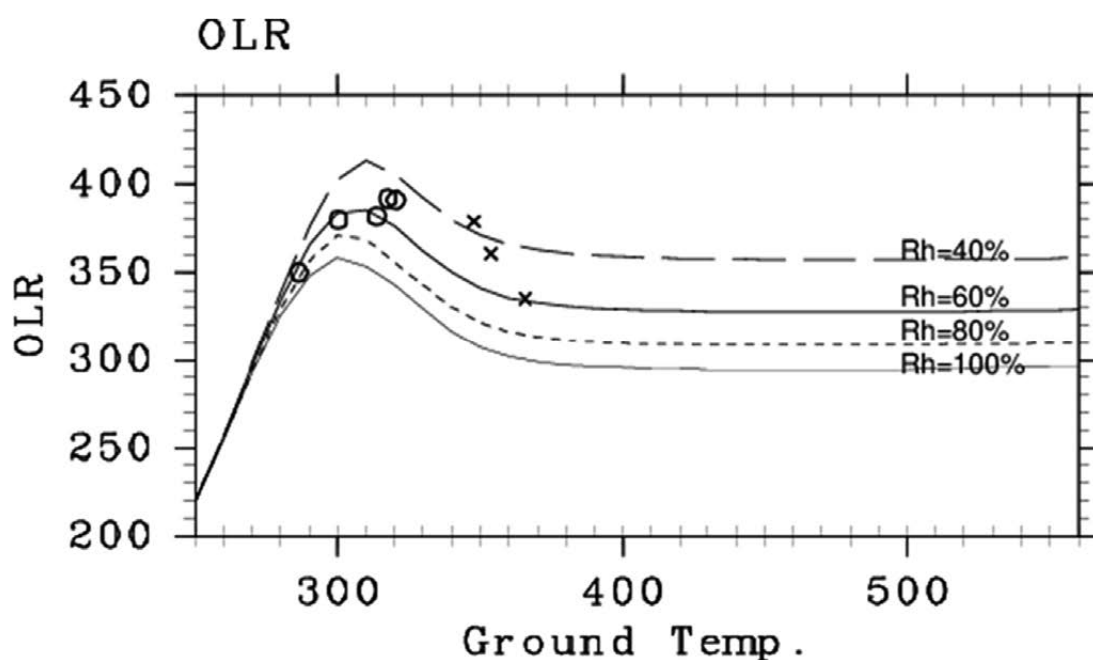


Figure 3.7 The relationship between surface temperature (K) and OLR (W m^{-2}). Curves represent surface temperature--OLR relationship obtained by the one-dimensional radiative-convective equilibrium model with various values of relative humidity for the radiation scheme. Thin solid line, dotted line, thick solid line and dashed line indicate 100% of relative humidity (the same as the results of NHA92), 80%, 60% and 40%, respectively. Marks represent the relationship between equatorial zonal mean values of surface temperature and OLR obtained by GCM. White circles and cross marks represent the results where the system reaches an equilibrium state and where the system cannot, respectively. From Ishiwatari et al. (2002), Fig. 7.

3.5 Circulation structure toward the runaway greenhouse state

In this section, we will observe the change of meridional circulation fields with the increase of solar constant to examine how the latitudinally uniform distribution of OLR becomes established and why the subtropical region is not fully dried. According to our results, the subtropical drying does appear; a careful observation of Fig. 3.4 shows that, in the cases with $S \geq 1500 \text{ W m}^{-2}$, the subtropical values of OLR are slightly greater than those at the equator. However, the subtropical drying does not proceed and the occurrence of a runaway greenhouse state is not prevented.

Figures 3.8, 3.9, and 3.10 show the zonal mean meridional circulation structures of the experiments S1380, S1570, and S1800, respectively. The plotted data are averaged for 50 days. In the experiment S1800, the temporal variation is so large that even for the zonal mean fields, 50 days is not enough to smooth out the variation. However, we cannot adapt the longer period for averaging, since the model atmosphere of the experiment S1800 is in the runaway greenhouse state and its circulation fields are secularly changing. The plotted period for S1800 is selected as the duration when the Hadley circulation shows relatively clear symmetry around the equator.

With the increase of incoming solar flux, the intensity and height of the Hadley circulation increases (Figs. 3.8e, 3.9e, 3.10e). Corresponding to this change, the amount of equatorial precipitation increases, and the peak of heating profile is shifted upward (Figs. 3.8b, 3.9b, 3.10b). It is noteworthy that the downward branch of Hadley cells remains at around $\pm 30^\circ$. The latitudinal width of Hadley cells hardly changes with the change of solar flux, which is consistent with the theory of Satoh (1994).

Subtropical drying appears for all the experiments in the sense that the values of relative humidity in the subtropics are less than those of the equatorial region. However, associated with the intensification of the Hadley circulation, the equatorial relative humidity also decreases, and hence, the difference between the subtropical and equatorial values of relative humidity decreases (Figs. 3.8d, 3.9d, 3.10d). Relative humidity of the whole Tropics decreases with the increase of the solar constant, but its value does not become extremely small. Even for the experiment S1800, the value of relative humidity in the subtropics is not less than 30%. Consequently, as is evident from the specific humidity fields (Figs. 3.8c, 3.9c, 3.10c), the absolute amount of water vapor increases steadily in all region including the subtropics. The increase of humidity in subtropical regions is caused by the increased moisture transport by eddies (figure not shown). The atmosphere becomes optically thick with the increase of incoming solar radiation as shown in the meridional distributions of optical depth (Fig. 3.11).

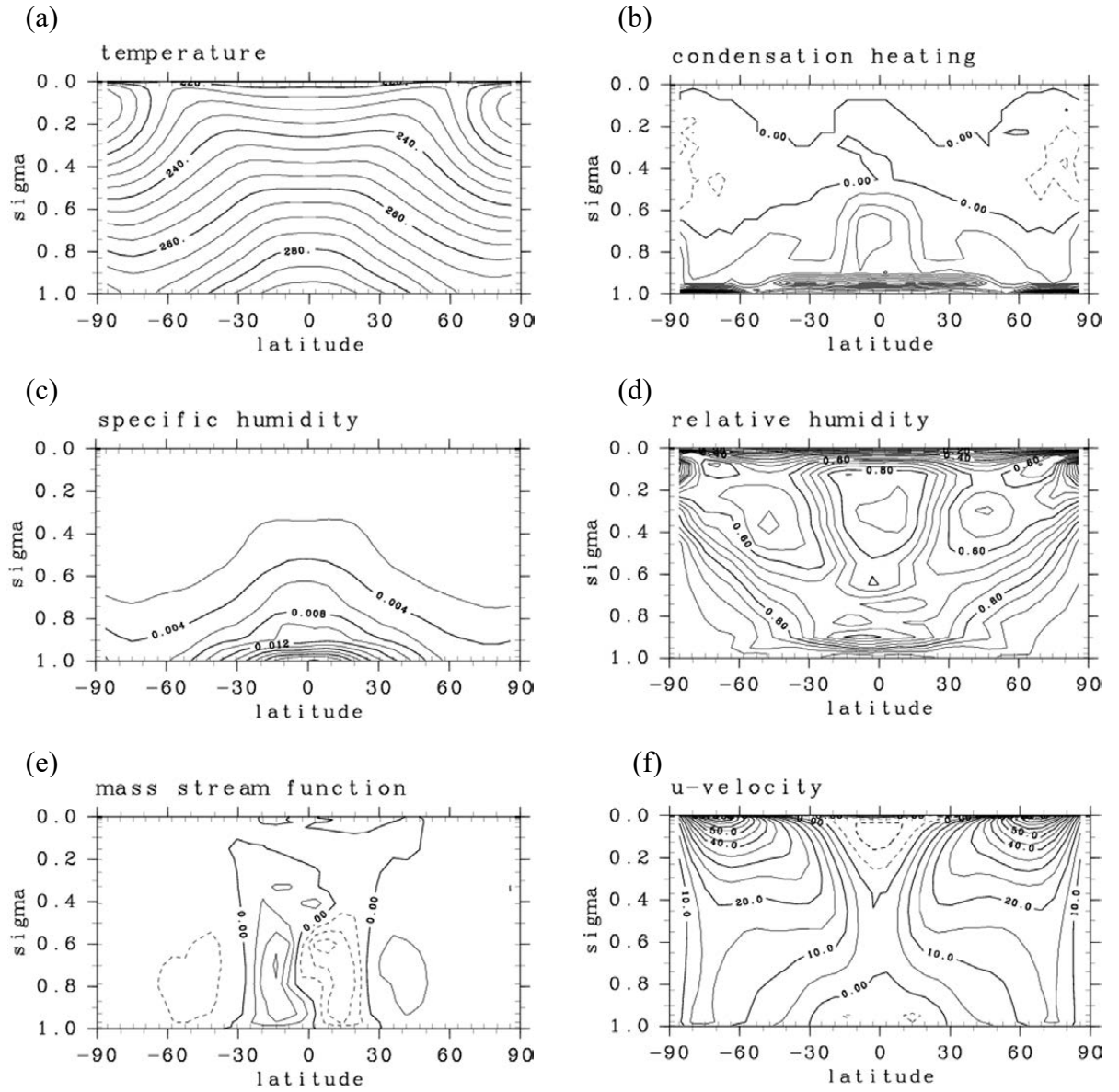


Figure 3.8 Meridional structures of the zonal mean circulation fields of the experiment S1380: (a) temperature, (b) condensation heating, (c) specific humidity, (d) relative humidity, (e) mass stream function, and (f) zonal wind. Contour intervals are (a) 5 K, (b) 5×10^{-6} K day⁻¹, (c) 2×10^{-3} , (d) 0.05, (e) 5 m s⁻¹, (f) 1.0×10^{10} kg s⁻¹, respectively. Time mean fields between t=950 to 1000 days are plotted. From Ishiwatari et al. (2002), Fig.8.

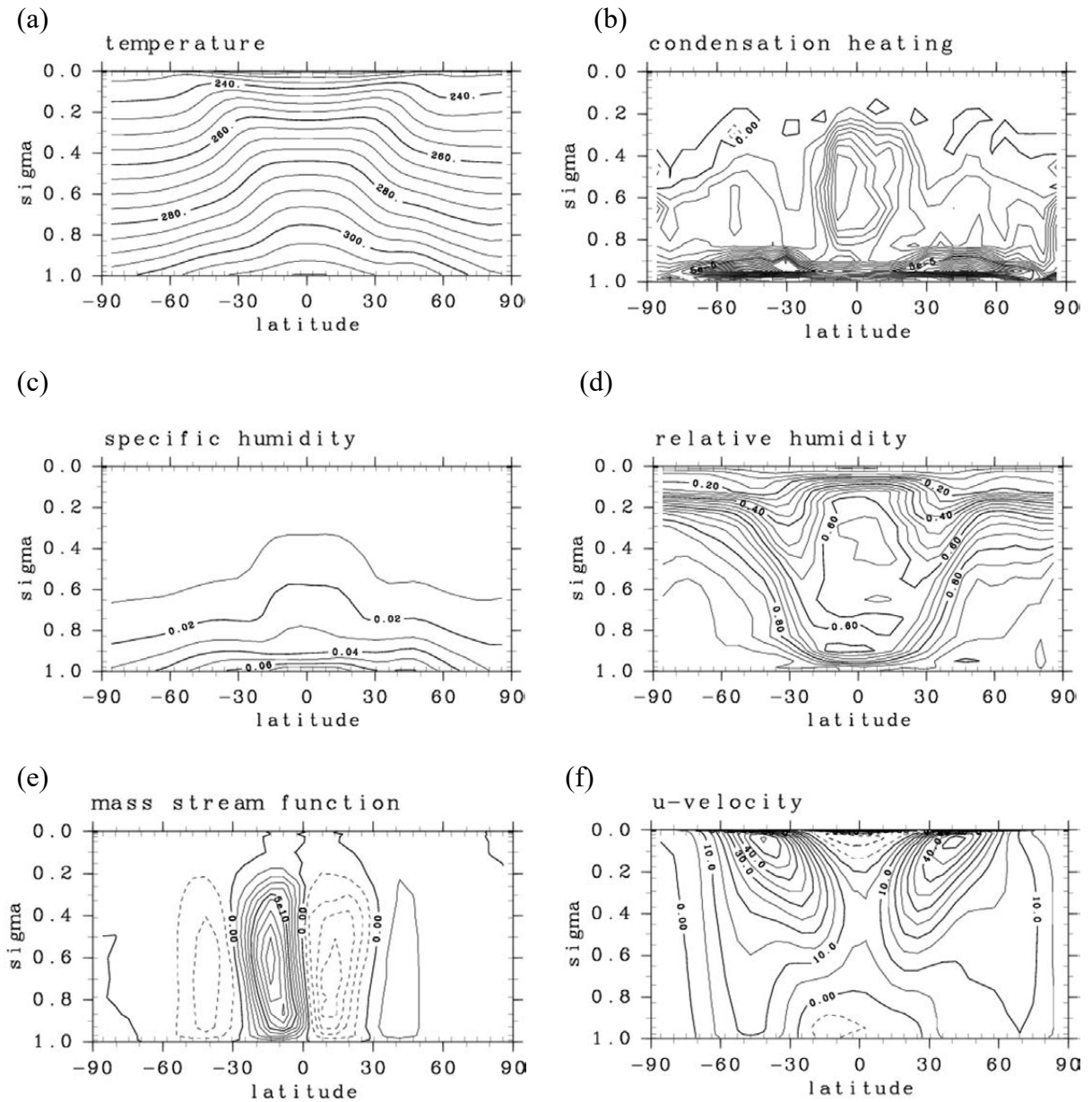


Figure 3.9 Same as in Fig. 3.8 but for the experiment S1570. Contour intervals are the same as in Fig. 3.8 except for (c) 1.0×10^{-2} . From Ishiwatari et al. (2002), Fig.9.

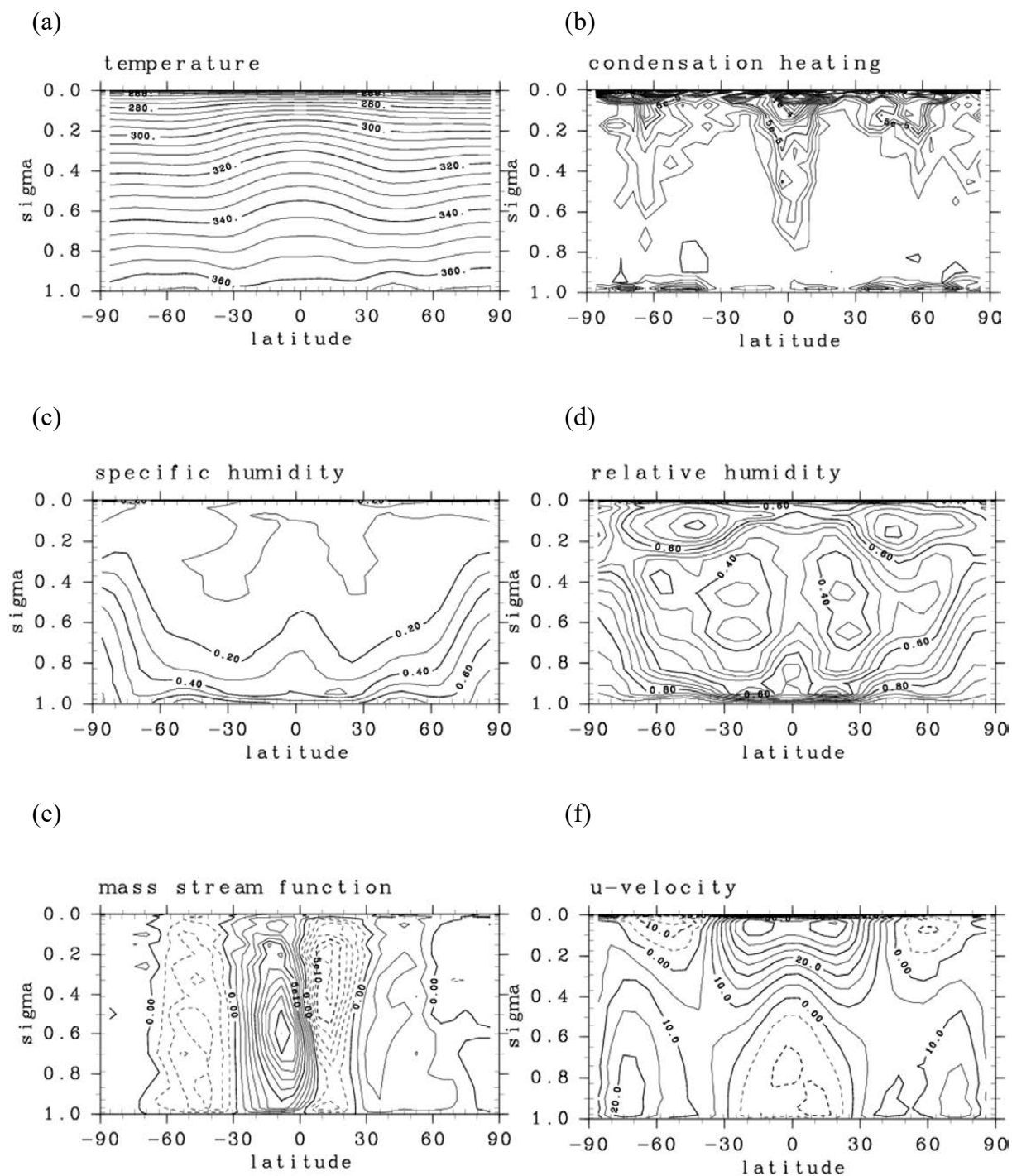


Figure 3.10 Same as in Fig. 3.8 but for the experiment S1800. Time-mean fields between $t=870$ to 920 days are plotted. Contour intervals are the same as in Fig. 3.8 except for (b) $1.0 \times 10^{-5} \text{ K day}^{-1}$ and (c) 0.1. From Ishiwatari et al. (2002), Fig.10.

As for the temperature fields, the meridional difference of temperature decreases as the solar flux increases (Figs. 3.8a, 3.9a). In the runaway greenhouse state (Fig.3.10a), the meridional difference of temperature almost disappears, which corresponds to the disappearance of meridional contrast of OLR profile. In the equilibrium states (S1570), however, detailed examination of Fig. 3.9a shows that subtropical temperature is significantly lower than that of the equator, although the meridional contrast of OLR is fairly small (Fig. 3.4a). This is because the changes of latitudinal profiles of temperature and humidity with the increase of solar flux have opposite effects on the change of subtropical OLR; cold subtropics cause OLR to be smaller, while dry subtropics cause OLR to be larger.

The results of this compensation can be observed in Fig. 3.12, which shows the meridional structure of temperature with optical depth as the vertical coordinate. For the experiment S1570, whose solar constant is just below the value for entering the runaway greenhouse state, the water vapor amount in the subtropical regions is relatively smaller than that of the equatorial region, and hence the $\tau = 1$ surface in the subtropical regions is located at the lower altitude (Fig. 3.11b). On the other hand, the temperature profile has its maximum at the equator and decreases toward both poles (Fig. 3.9a). Consequently, the temperature profile on the surface of $\tau = 1$ is more uniform than that on the surface of constants (Fig. 3.12b). The latitudinal profile of OLR tends to be flat even in the experiments where the solar constant is below runaway value, although there still exists a significant amount of latitudinal temperature difference. In those ways, the values of OLR at all latitudes gradually approach the equatorial limit as the value of the solar constant is increased toward this limit.

There should be an increase of poleward heat transport to have a latitudinally uniform OLR distribution, since the latitudinal gradient of incoming heat supply increases as the solar constant increases. This actually is achieved by the increase of latent heat flux. Figure 3.13 shows the latitudinal distributions of heat fluxes. With the increase of the solar constant, latent heat flux dominates radiation flux in the surface heat budget. This tendency is most notable in the runaway greenhouse state (Fig. 3.13c), in which the surface radiation flux almost vanishes and most of the incoming heat is supplied to the atmosphere in the form of latent heat flux. Correspondingly, in the profile of precipitation, in addition to the increase at equatorial peak (Figs. 3.13b,c), there appear new precipitation peaks around latitude $\pm 60^\circ$. The large amount of latent heat release caused by precipitation in those higher latitudes contributes to the realization of the meridional homogenization of temperature.

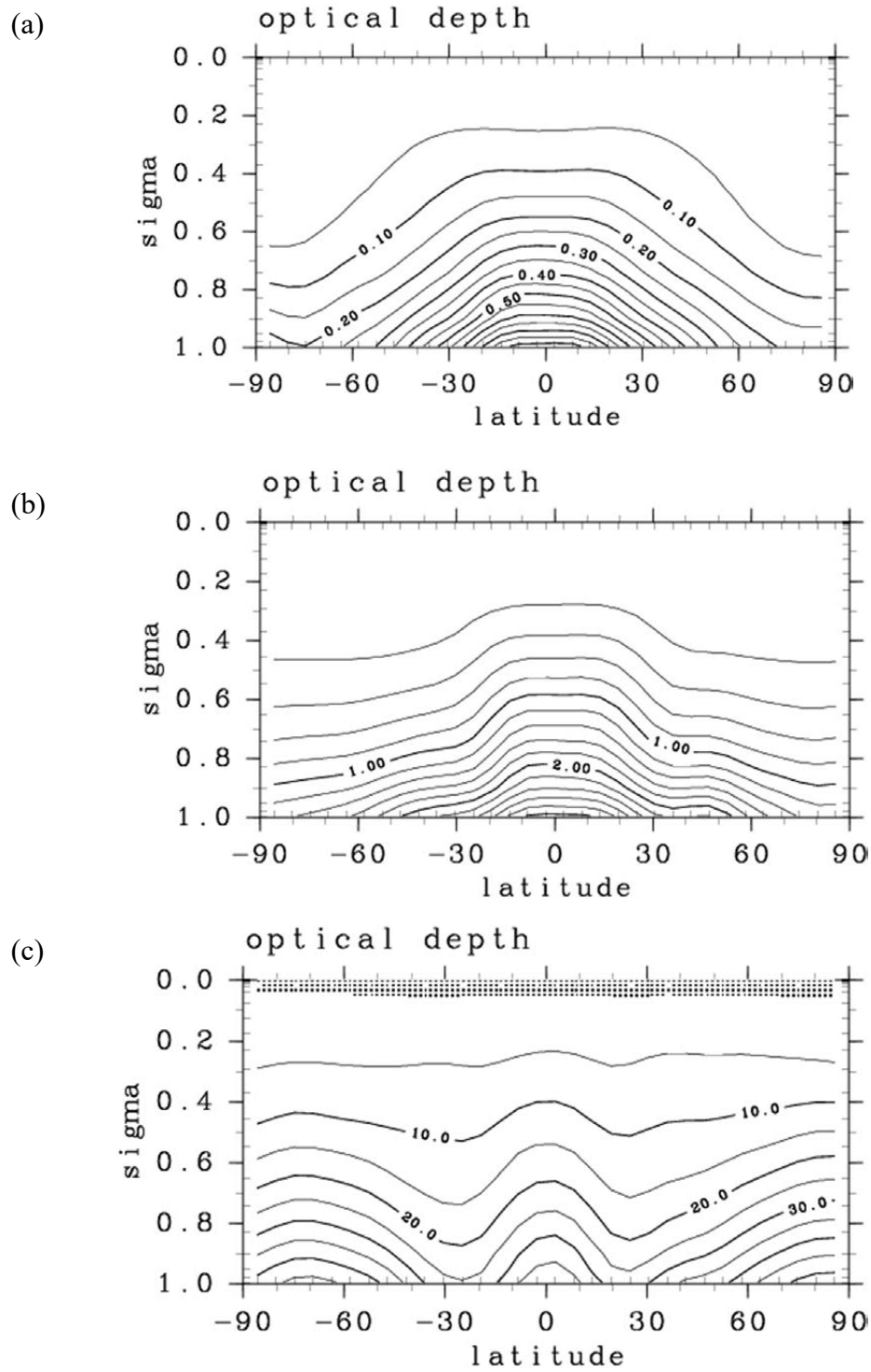


Figure 3.11 Meridional structure of zonal mean optical depth in the experiments (a) S1380, (b) S1570, and (c) S1800. Here, σ is used as the vertical coordinate. The contour intervals are (a) 0.05, (b) 0.2, and (c) 5.0, respectively. The shaded areas in (c) represent the area with optical depth less than 1. From Ishiwatari et al. (2002), Fig.11.

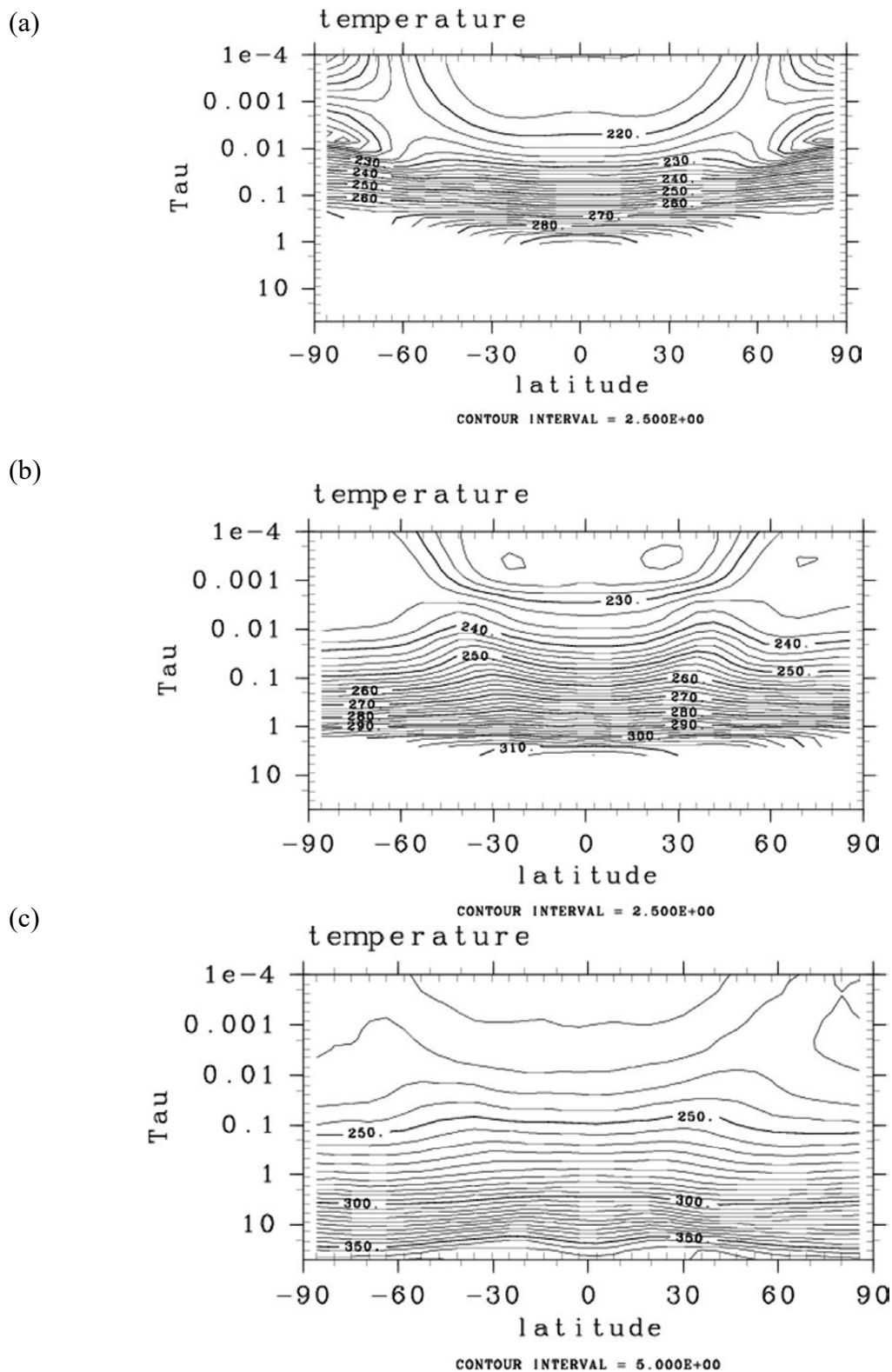


Figure 3.12 Meridional structure of temperature with the optical depth as the vertical coordinate in the experiments (a) S1380, (b) S1570, and (c) S1800. The areas without data correspond to the regions below the ground surface. The contour intervals are (a) 2.5K, (b) 2.5K, and (c) 5.0K, respectively. From Ishiwatari et al. (2002), Fig.12.

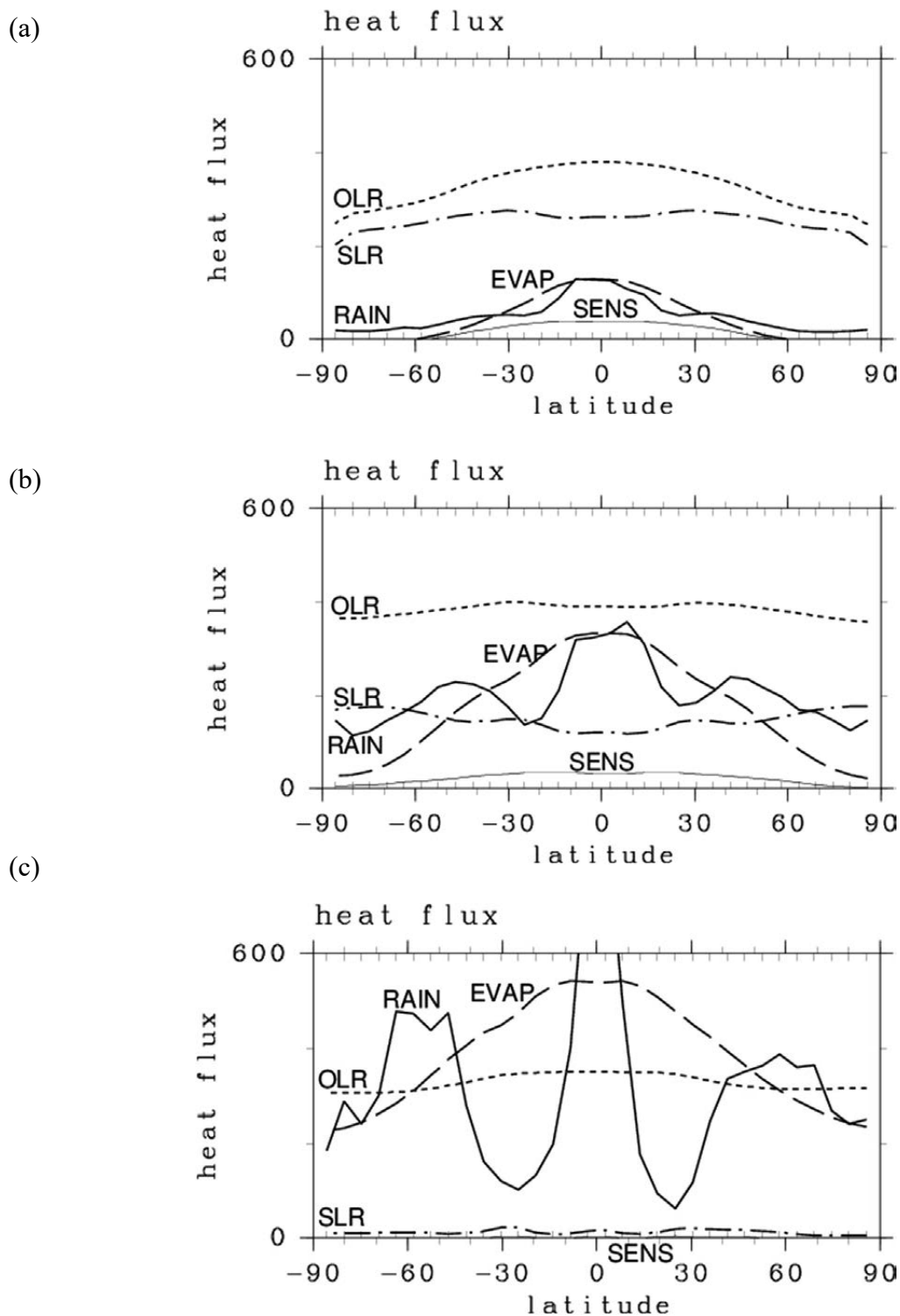


Figure 3.13 The meridional distributions of vertical energy fluxes in experiments (a) S1380, (b) S1570, and (c) S1800. Thick solid line, dashed line, dotted line, dashed-dotted line, and thin solid line indicate condensation heating (RAIN), evaporation flux (EVAP), OLR, net longwave radiation at the surface (SLR), and sensible heat flux (SENS), respectively. Unit is W m^{-2} . The condensation heating of (c) has its maximum value of 920 W m^{-2} at the equator. From Ishiwatari et al. (2002), Fig.13.

3.6 Remarks

As mentioned in Section 3.1, we found a critical bug in the implementation of moist convective adjustment (MCA) scheme in the general circulation model used by Ishiwatari et al. (2002). That is, the sign of the switching-on condition of MCA scheme was opposite: MCA was activated at the saturated grid point where the vertical stratification was more stable than the moist adiabat. Moreover, in the course of performing re-experiments for bug-fix, it was found that integration periods were insufficient for reaching statistically equilibrium states in the experiment of Ishiwatari et al. (2002). We performed some re-experiments with a bug-fixed model and found that the results are not changed qualitatively although quantitative changes in temperature field or zonal mean field emerged. Therefore, we consider that our main results of this chapter are not changed qualitatively.

3.7 Summary

We have performed a series of numerical experiments using a GCM with a gray atmosphere to investigate a possible three-dimensional counterpart of the runaway greenhouse state defined by NHA92 with a one-dimensional radiative-convective equilibrium model. The experimental results show that, even when the effects of spherical geometry and atmospheric motion are included, there exists an upper limit of OLR which the atmosphere with water vapor as an infrared absorber can emit. The experiments also show that when the value of the solar constant exceeds the upper limit of OLR, the atmosphere sets into a thermally runaway state. The upper-limit value is constrained by the vertical structure of the atmosphere in the equatorial region. As the solar constant increases, the thermal structure becomes uniform in the latitudinal direction, and the values of OLR at all latitudes approach the equatorial limit. The equatorial vertical structure of temperature and radiation can be well described by the one-dimensional radiative-convective equilibrium model of NHA92 by considering the actual value of relative humidity realized in the three-dimensional system. This fact indicates that the thermally runaway state obtained by the three-dimensional calculation is the realization of the runaway greenhouse state defined by NHA92. It is concluded that we can predict the emergence of the runaway greenhouse state by comparing the value of global mean SSR with the upper limit of OLR calculated by the use of the one-dimensional radiative-convective equilibrium model with the relative humidity considered. The condition for the occurrence of runaway greenhouse state in the three-dimensional system is that the global mean value of incoming flux, neither the maximum nor the minimum of the latitudinal distribution of incoming flux, exceeds the upper limit of OLR.

Chapter 4

Circulation structure of planets with a peculiar distribution of incoming solar radiation flux: climate of synchronously rotating planets

*This chapter is based on “Noda S., Ishiwatari M., Nakajima K., Takahashi Y.O., Takehiro S., Onishi M., Hashimoto G.L., Kuramoto K., Hayashi Y.-Y. (2017) The circulation pattern and day-night heat transport in the atmosphere of a synchronously rotating aquaplanet: Dependence on planetary rotation rate. Icarus 282., 1-18,” ©The author(s), Published by Elsevier Inc. This is an open access article under the CC BY license.
(<http://creativecommons.org/licenses/by/4.0/>)*

4.1 Introduction

In this chapter, we present the result of Noda et al. (2017) who investigate the climate of synchronously rotating planets which have fixed day-side and night-side. Noda et al. (2017) focused on the dependence of circulation structure on planetary rotation rate Ω^* . The atmospheric circulation structure, which should be related to day-night energy transport, has been shown to depend on the planetary rotation rate (Showman et al., 2013). Using a GCM with a slab ocean, Merlis and Schneider (2010) obtains a day-night thermally direct circulation in the case with $\Omega^*=1/365$, whereas high-latitude westerlies emerge in the case with $\Omega^*=1$. The latter circulation pattern is similar to that obtained earlier by Joshi (2003) with $\Omega^*=1$. Merlis and Schneider (2010) names the two circulation regimes the “slowly rotating regime” and the “rapidly rotating regime”, respectively. However, there is little information on the transition between these two regimes. Edson et al.(2011) explores the Ω^* dependence of the atmospheric circulation structures of both dry and moist planets, and shows that, in addition to the two regimes similar to those identified by Merlis and Schneider (2010), a regime with a strong westerly zonal wind in low latitudes appears with intermediate values of Ω^* . It is also shown that, for the dry planet condition, an abrupt change of zonal wind velocity occurs and multiple equilibria with hysteretic behavior exist between $\Omega^*=0.109$ and $\Omega^*=0.25$. However, corresponding multiple equilibria for the aquaplanet have not been described clearly.

As for day-night energy transport, Merlis and Schneider (2010) shows that the amounts of moist static energy transport are almost the same for the two cases with $\Omega^*=1/365$ and $\Omega^*=1$, but there is no information about energy transport for intermediate values of Ω^* . Edson et al.(2011) describes Ω^* dependences of minimum, maximum, and globally averaged mean surface temperature, but does not present that of energy transport. The dependence of day-night energy transport on Ω^* , together with possible constraints on it, remain to be explored.

In Noda et al. (2017), a series of GCM runs with Ω^* incremented by small steps is performed under a simple setup considering a moist planet that rotates synchronously. They confirmed that, for the same value of incoming solar flux as that of the present Earth's, statistically equilibrium states are obtained and the runaway greenhouse state does not occur for various values of Ω^* including those that are not closely examined in the previous studies. Noda et al. (2017) also examined how Ω^* affects the atmospheric circulation structure and day-night energy transport, and consider what determines the amount of day-night energy transport. In the followings, details of the results obtained by Noda et al. (2017) are presented.

4.2 Model configuration

As for atmospheric constituent and radiation process, the same configuration as Section 3.2 (case (1), case for gray radiation, described in Section 2.4) is used. The values of molecular weight and specific heat of dry air are set to $28.964 \times 10^{-3} \text{ kg mol}^{-1}$ and $1004.6 \text{ J K}^{-1} \text{ kg}^{-1}$, respectively. The values of molecular weight and specific heat of water vapor are set to $18.0 \times 10^{-3} \text{ kg mol}^{-1}$ and $1810.0 \text{ J K}^{-1} \text{ kg}^{-1}$, respectively.

Same as Section 3.2, all of the planetary surface is assumed to be “swamp ocean.” The surface albedo is set to zero. Same configurations as Section 3.2 are used except for planetary rotation rate. We use 16 values of planetary rotation rate, Ω^* : $\Omega^* = 0, 0.05, 0.1, 0.15, 0.2, 0.25, 0.33, 0.5, 0.6, 0.67, 0.7, 0.75, 0.8, 0.85, 0.9$, and 1.0 . Hereafter each case will be referred to as character Ω followed by the value of Ω^* . For example, $\Omega 0.05$ is the case with orbital period of 20 Earth days. Note that changing Ω^* with fixed solar constant means changing the luminosity of the central star. Although no planet with $\Omega^* = 0$ exists in reality, we examine the circulation structure of this idealized non-rotating planet as the limiting case of small Ω^* . The synchronously rotating planet is configured with the obliquity set to zero, and the distribution of incoming solar flux fixed to the planetary surface (Fig. 4.1) according to

$$S_{\text{solar}} = S_0 \max[0, \cos \phi \cos(\lambda - \lambda_0)] \quad (4.1)$$

where ϕ is latitude and λ is longitude, with subsolar longitude $\lambda_0 = 90^\circ$ and solar constant $S_0 = 1380 \text{ W m}^{-2}$, which is about 88% of the threshold value ($S_0 = 1570 \text{ W m}^{-2}$) to enter the runaway greenhouse state obtained by the non-synchronously rotating aquaplanet experiment by Ishiwatari et al. (2002).

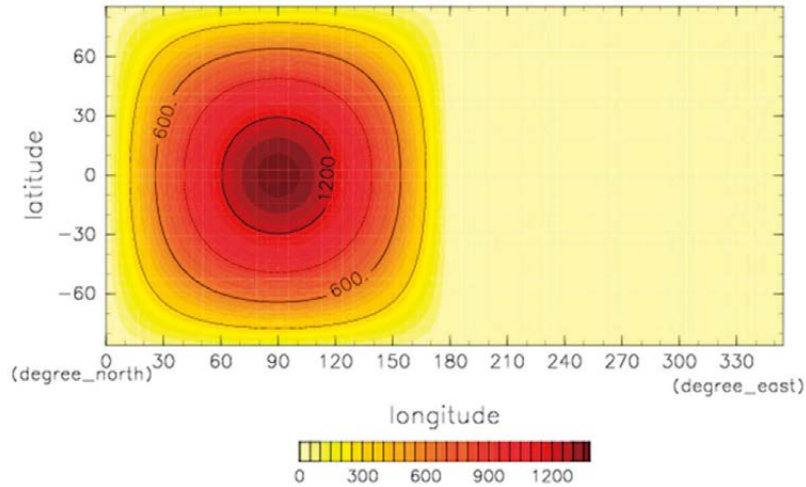


Figure 4.1 Horizontal distribution of the incoming solar flux [W m^{-2}] given by Eq. (4.1). Contour interval is 300 W m^{-2} . From Noda et al. (2017), Fig. 1.

For each Ω^* , we perform 10 runs. As will be discussed in the following sections, we have recognized that initial condition dependence appears for certain values of Ω^* ; different types of circulation patterns result from slightly different initial conditions. The initial condition for each run is an isothermal (280K) resting atmosphere with a small temperature perturbation in the form of random noise with amplitude of 0.1 K added to all grid-points; we prepare ten

different perturbation fields for the ten runs. Each run is integrated for 2000 Earth days, and the data from the last 1000 days are used for analysis. The horizontal resolution utilized in the present study is 32×64 that corresponds to spectral truncation T21. The number of vertical levels is set to 16. The model top level is set to $\sigma=0.02$. We performed test runs for several values of Ω^* employing 32 vertical levels with the top level of $\sigma=9.2 \times 10^{-5}$. The results show no qualitative change in either the atmospheric circulation characteristics or the energy budget compared with those with 16 vertical levels; the change in day side averaged OLR is at most 10 W m^{-2} (figures not shown), which is negligibly small compared to the value of OLR itself. We also conducted a high resolution test experiment up to T341 with $\Omega^* = 1$, and confirmed that the large scale circulation and the surface temperature patterns are mostly unchanged. These sensitivity tests show that the vertical and horizontal resolutions are adequate for the present purpose.

4.3 Dependence of the atmospheric circulation characteristics on the planetary rotation rate

In all runs the atmosphere reaches a statistically equilibrium state; the runaway greenhouse state does not emerge. Fig. 4.2 shows temporal changes of the global mean values of surface temperature and OLR obtained in four typical runs with different values of Ω^* . In every case, the atmosphere settles down after about 300 days to a statistically equilibrium state in which both global mean surface temperature and OLR fluctuate around their equilibrium values. The temporal mean values of global mean surface temperature and the magnitudes of temperature fluctuation differ among runs.

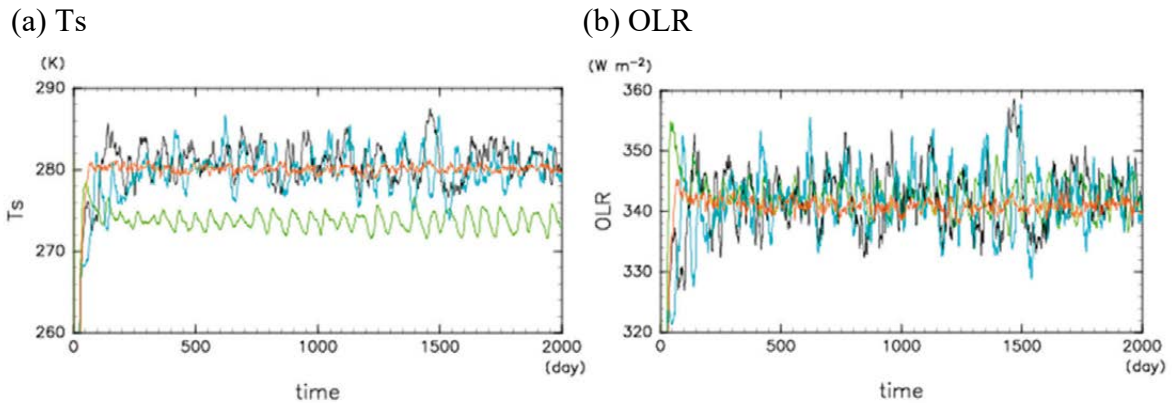


Figure 4.2 Time series of global mean quantities. (a) Surface temperature [K] and (b) OLR [W m^{-2}]. Green, light-blue, black, and red lines indicate $\Omega_{0.0}$, $\Omega_{0.15}$, $\Omega_{0.75}$, and $\Omega_{1.0}$, respectively. From Noda et al. (2017), Fig. 2.

The structure of the atmospheric circulation varies with Ω^* . Fig. 4.3 summarizes the variety of global distributions of time mean surface temperature for various values of Ω^* . For

each value of Ω^* , the result of a single run arbitrarily chosen from the ten runs is plotted. In Fig. 4.3, we can identify at least three features that characterize the variety of surface temperature. First, an equatorial warm belt in the night hemisphere is present in $\Omega 0.05$ - $\Omega 0.8$ (Fig. 4.3b-m), while it is absent in the other cases. Second, the equatorial region is generally warmer in $\Omega 0.0$ - $\Omega 0.8$ (Fig. 4.3a-m), while the mid-latitude regions are warmer in the other cases. These two features above reflect the meridional structures of zonal mean zonal wind, as will be shown later. Third, a north-south asymmetry is evident in $\Omega 0.6$ - $\Omega 0.8$ (Fig. 4.3i-m), while it is absent or weak in the other cases. This last feature reflects the presence of north-south asymmetric variability with long time scales, as will be described in Section 4.4.3.

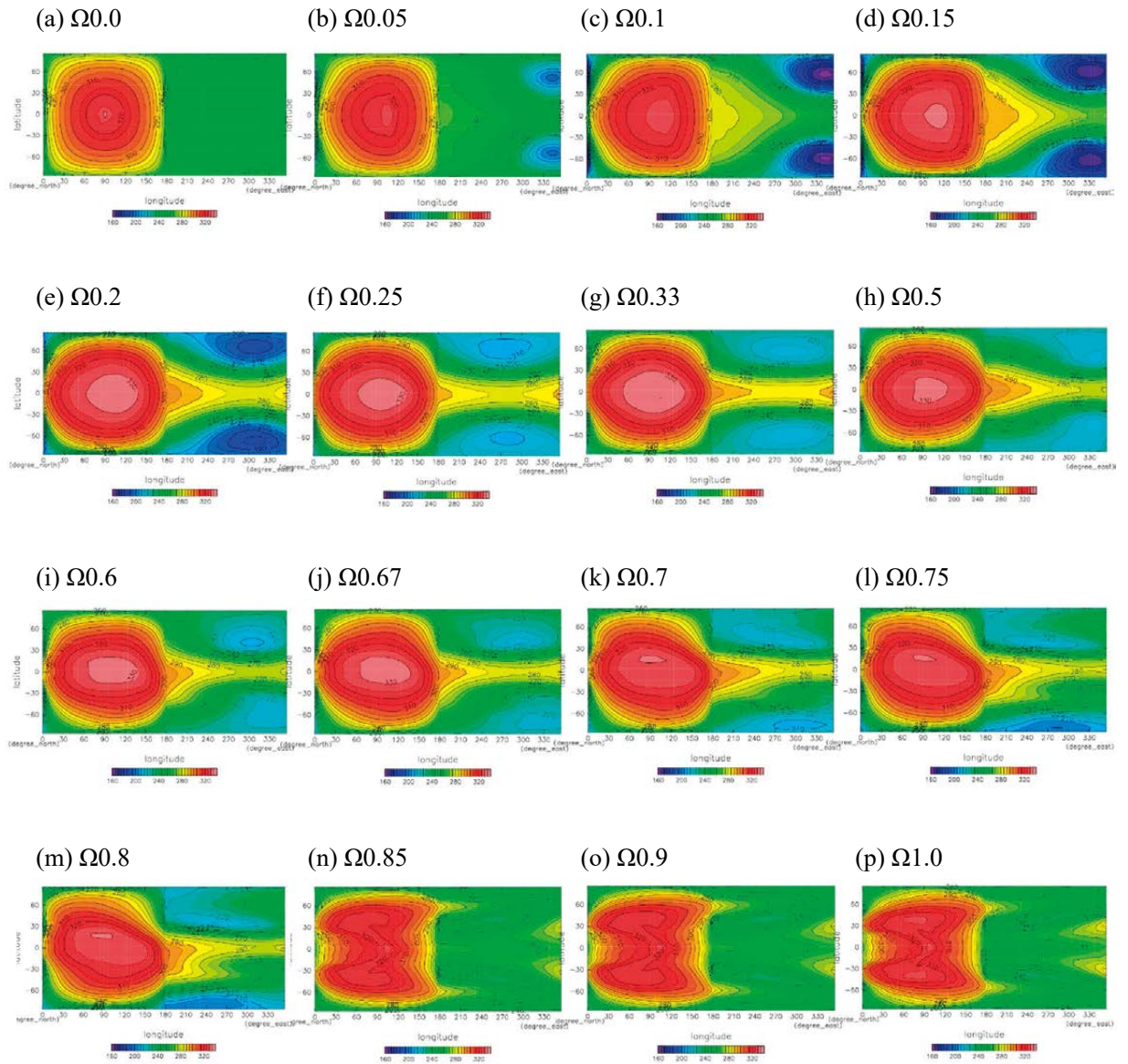


Figure 4.3 Horizontal distributions of 1000-day mean surface temperature for all of the computed values of Ω^* . Contour interval is 5 K. From Noda et al. (2017), Fig. 3.

For a more quantitative description of the general dependence of the atmospheric circulation structure on Ω^* , bearing in mind the three features of the surface temperature fields identified above, we examine the Ω^* -dependences of four quantities. These are the surface temperatures at the subsolar and antisolar points, the upper tropospheric zonal mean zonal wind at the equator, and a measure of north-south asymmetry in the surface temperature with short time scale transients filtered out defined by

$$\Delta_{NS} [T_s] \equiv \frac{1}{2\pi} \int_0^{\pi/2} \int_0^{2\pi} |\overline{T_s}(\lambda, \phi) - \overline{T_s}(\lambda, -\phi)| d\lambda \cos \phi d\phi \quad (4.2)$$

where $\overline{T_s}$ is the 50 day running average of surface temperature, and the overbar means the temporal average over 1000 days. Fig. 19 shows the Ω^* dependences of these four quantities. Note that the ten runs for each value of Ω^* are plotted separately. Now we can identify two separate branches of atmospheric states: one extending from $\Omega^*=0.0$ to $\Omega^*=0.8$ (hereafter, the small- Ω branch), and the other from $\Omega^*=0.7$ to $\Omega^*=1.0$ (hereafter, the large- Ω branch). Between $\Omega^*=0.7$ and $\Omega^*=0.8$, these two branches coexist, giving multiple equilibria. The preference between the two branches in the range of the multiple equilibria seems to depend on the value of Ω^* ; the ratio of runs on the large- Ω branch increases from 10% for $\Omega^* = 0.7$ to 80% for $\Omega^* = 0.8$. The branch taken by a particular run depends on small differences in the initial conditions. It is determined in the first ~ 500 days of the model integration, and there is no switching to the other branch after that. Note that those shown in Fig. 4.3k-m belong to the small- Ω branch by chance; there are also runs belonging to the large- Ω branch for this range of Ω^* , with surface temperature structure similar to those shown in Fig. 4.3n-p.

In Fig. 4.4 we observe that the atmospheric circulation characteristics change continuously but markedly on the small- Ω branch. When $\Omega^*=0$, both zonal mean zonal wind and north-south asymmetry are negligible. As Ω^* increases, the westerly wind intensifies rapidly, and the night side surface temperature rises rapidly, both of which are tied to the appearance of the equatorial warm belt identified in Fig. 18b-m. The temperature at the subsolar point falls at first, then rises. The north-south asymmetry remains small. Around $\Omega^*=0.5$, the north-south asymmetry increases, and continues to increase with increase of Ω^* . The asymmetry has been identified in Fig. 4.3i-m, but is not evident in cases $\Omega^*0.2$ - $\Omega^*0.5$ (Fig. 4.3e-h), where, as will be shown later, the temporal scale of the variability is short compared with the averaging period of 1000-days. Until the end of the small- Ω branch at $\Omega^*=0.8$, the values of temperature at the subsolar and antisolar points remain high, and the zonal mean wind at the equator maintains its strength. On the large- Ω branch, the upper tropospheric zonal mean wind is easterly. The temperature is lower than that of the small- Ω branch at both the subsolar and antisolar points, and north-south asymmetry is weak. Changes in the four circulation characteristics are rather small over the entire range ($0.7 \lesssim \Omega^* \lesssim 1$) of the large- Ω branch.

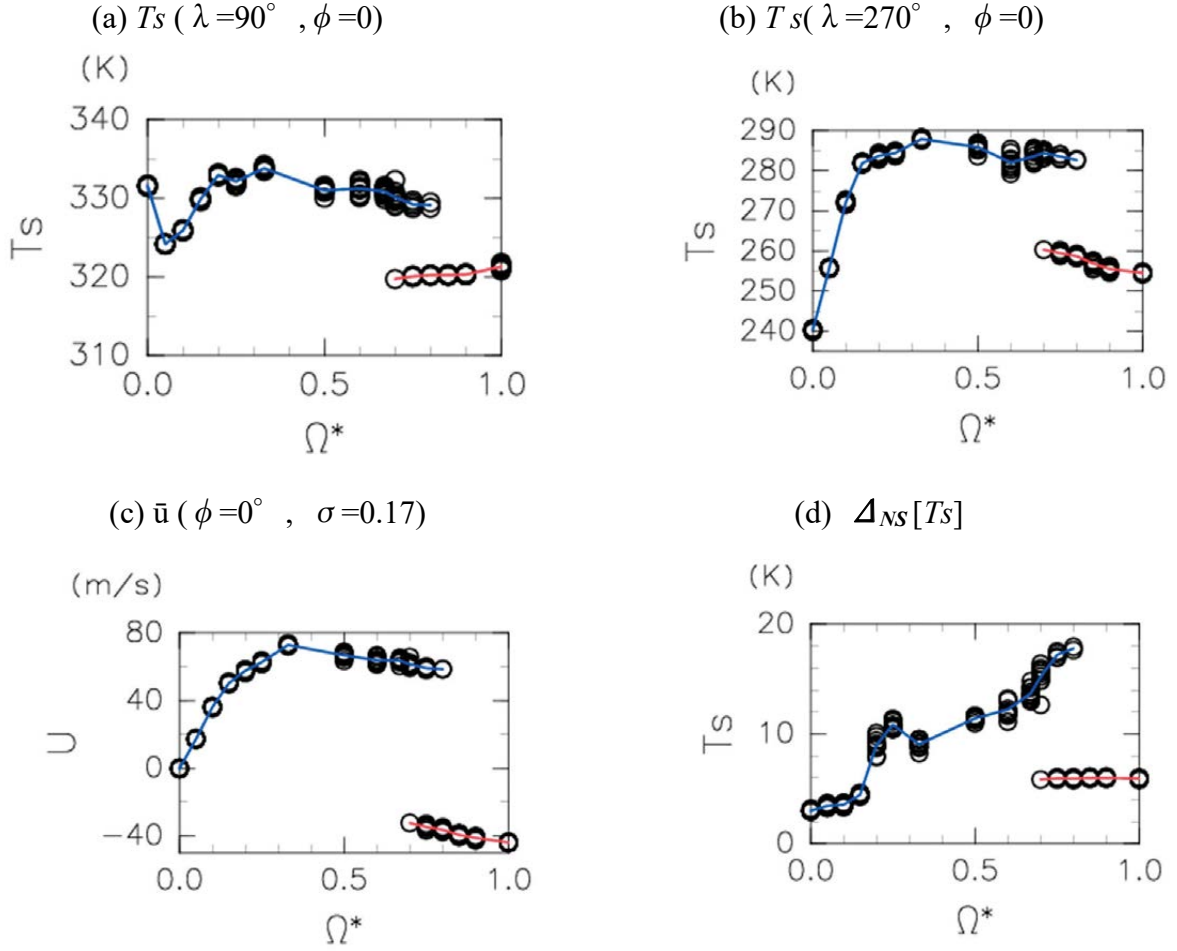


Figure 4.4 Ω^* dependences of (a) surface temperature [K] at the subsolar point, (b) surface temperature [K] at the antisolar point, (c) zonal mean equatorial zonal wind [m s^{-1}] at $\sigma=0.17$, and (d) degree of north-south asymmetry of surface temperature defined by Eq. (4.2) in the text [K]. The values are temporal averages between day 1000 and day 2000. All 10 runs for each Ω^* case are plotted. Red and blue lines are ensemble averages for the small- Ω and the large- Ω branches, respectively. From Noda et al. (2017), Fig. 4.

4.4 Typical atmospheric circulation structures

In order to understand the atmospheric circulation and its dependence on Ω^* on the synchronously rotating planet, we examine here the spatial structures and temporal variation of the solutions in detail. Although the circulation structure changes more or less continuously as Ω^* changes on the small- Ω branch as implied in Figs. 4.3 and 4.4, we can classify the circulation structures into three types according to the zonal wind structure and the temporal variability. They are, in order of the planetary rotation rate where they appear, Type-I, characterized by day-night convection, Type-II, characterized by a broad equatorial westerly jet and a north-south symmetric stationary wave-like pattern that turns out to be a stationary

Rossby wave, and Type-III, characterized by long time scale north-south asymmetric variability. In the large- Ω branch we can classify the circulation structure as Type-IV, characterized by a pair of mid-latitude deep westerly jets. For each of the four types, we choose one case and examine it in detail below.

4.4.1 Type-I: Day-night convection (Case $\Omega 0.0$)

The Type-I circulation appears in cases with very small values of Ω^* , and is characterized by day-night convection; it is similar to those obtained with small Ω^* in earlier studies (Merlis and Schneider, 2010; Edson et al., 2011). We examine Case $\Omega 0.0$ as a representative case of Type-I.

The time mean structure of the atmospheric circulation in case $\Omega 0.0$ is shown in Fig. 4.5. Upper tropospheric horizontal flow diverges toward the night side (Fig. 4.5b) from the concentrated upward motion at the subsolar point, where intense precipitation develops (Fig. 4.5e). The outflow is strong not only in the upper troposphere ($\sigma \sim 0.23$) but also at the middle levels around $\sigma \sim 0.55$ (Fig. 4.5c). In the middle troposphere, the entire planet except at the subsolar point is covered with a widespread, weak, and almost homogeneous downward flow (Fig. 4.5c). In the lower troposphere ($\sigma \sim 0.9$), the air flow diverges from the antisolar point and returns to the day side, connected to the flow converging toward the subsolar point.

The surface temperature distribution (Fig. 4.5h) closely follows the incoming solar flux distribution (Fig. 4.1). The night side surface temperature is almost homogeneous; its variation is as small as 10 K, being by far the smallest among all the experiments. The surface pressure distribution (Fig. 4.5a) can be interpreted as a direct response to the surface temperature distribution; a notable feature is the heat low in the lower troposphere of the day side (Figs. 4.5a and 4.5c). Temperature on the night side is generally highest in the middle levels ($\sigma \sim 0.6$) and lower nearer the surface (Fig. 4.5c). In contrast, temperature in the heat low around the subsolar point ($20^\circ \leq \lambda \leq 160^\circ$), increases with decreasing altitude.

The hydrological cycle is governed by the direct day-night circulation. Surface evaporation has its maximum at the subsolar point, and is very small over the whole night side (Fig. 4.5f). Rainfall occurs almost exclusively around the subsolar point (Fig. 4.5e). The middle level outflow from the subsolar point (Fig. 4.5c) advects moist air into the night side, producing relatively moist tongues ($0.45 \leq \sigma \leq 0.65$, $\lambda < 210^\circ$ and $\lambda > 320^\circ$) (Fig. 4.5d). However, the magnitude of the vertically integrated water vapor flux (Fig. 4.5g) is fairly small compared to those for the other circulation types.

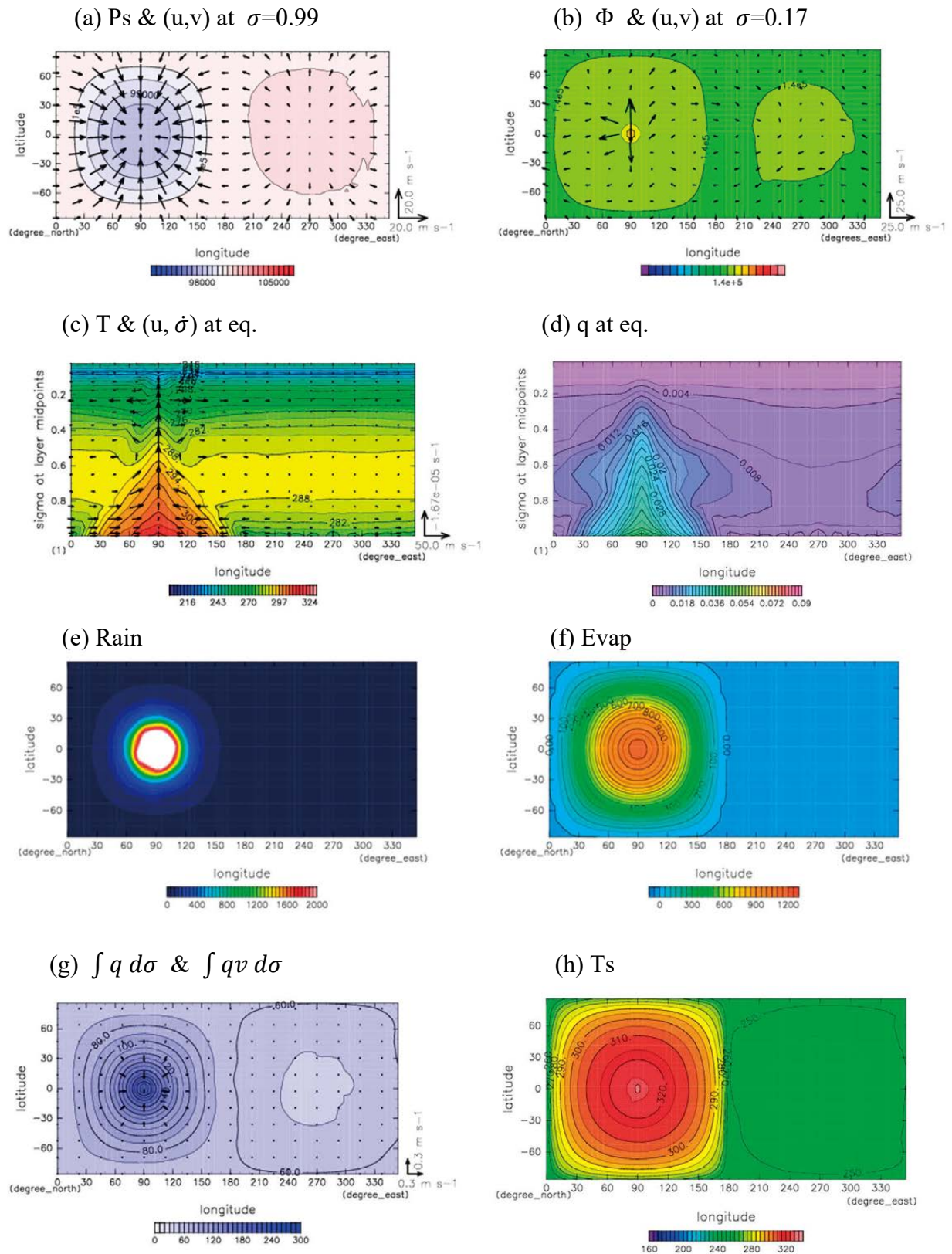


Figure 4.5 Day 1000 to day 2000 temporal mean fields for case $\Omega 0.0$. (a) Surface pressure (color shading) [Pa] and horizontal wind vectors [m s^{-1}] at the lowest level. Contour interval of surface pressure is 5×10^2 Pa, and the unit vectors of zonal and meridional wind are

20 m s⁻¹. (b) Horizontal wind vector [m s⁻¹] and geopotential [J kg⁻¹] at $\sigma=0.17$. Unit vector indicates 25 m s⁻¹. Contour interval of geopotential is 500 J kg⁻¹. (c) Vertical wind $-\dot{\sigma}$ [s⁻¹] and zonal wind [m s⁻¹] (vector), and temperature [K] (color) in the equatorial vertical section. Unit vectors of vertical wind and zonal wind are 1.67×10^{-5} s⁻¹ and 50 m s⁻¹, respectively. Contour interval of temperature is 5 K. (d) Specific humidity at the equator. Contour interval is 2×10^{-3} . (e) Condensation heating [W m⁻²]. Color interval is 50 W m⁻². White area represents heating over 2000 W m⁻². (f) Horizontal distribution of surface evaporation [W m⁻²]. Color interval is 50 W m⁻². (g) Vertically integrated water vapor flux [m s⁻¹] and vertically integrated water vapor mass [kg m⁻²]. Unit vector is 0.3 m s⁻¹. Contour interval is 10 kg m⁻². (h) Surface temperature [K]. Contour interval is 5 K. From Noda et al. (2017), Fig. 5.

4.4.2 Type-II: Stationary Rossby wave on broad equatorial westerly jet (Case $\Omega 0.15$)

The Type-II atmospheric circulation structure appears for $0.05 \lesssim \Omega^* \lesssim 0.2$ and is characterized by a warm region on the night side (Fig. 4.3b-d) below an intense broad equatorial westerly wind as shown in Fig. 4.4c, and large amplitude wavenumber one stationary waves in the higher latitudes. These features are also seen in the circulations obtained in an intermediate range of Ω^* by Edson et al. (2011). We examine Case $\Omega 0.15$ as a representative case of Type-II.

The time mean structure of the atmospheric circulation in case $\Omega 0.15$ is shown in Fig. 4.6. The most notable feature is the emergence of a broad and deep westerly wind that covers almost the whole depth of the troposphere (Fig. 4.6c) of the low-latitudinal region (Fig. 4.6b). In the bottom layer near the surface, a trace signature of day-night circulation can still be noted (Fig. 4.6a). The location of maximum rainfall and the associated deep updraft are shifted eastward from the subsolar point by about 20° (Fig. 4.6c and Fig. 4.6e), possibly due to moisture advection by the deep westerly wind. The surface temperature peak is also shifted eastward from the subsolar point by 25° (Fig. 4.6h). A similar eastward shift emerges also in the other cases on the small Ω branch, explaining the drop in subsolar point surface temperature at $\Omega^* \sim 0$ (Fig. 4.4a). The peak of evaporation remains at the subsolar point (Fig. 4.6f). In fact, the latent heat flux around the equator on the day side changes little over the range of Ω^* examined in this study. The insensitivity to Ω^* results from the employment of the swamp surface condition and cloud free condition; the incoming shortwave radiation reaching the ground surface has fixed geographical distribution, and must be approximately balanced by the energy loss by latent heat of evaporation. The surface pressure minima are located at $(\lambda, \phi) \sim (120^\circ, \pm 15^\circ)$; these are not only to the east of the subsolar point, but also off the equator (Fig. 4.6a). The higher-latitude regions are characterized by intense wavenumber one stationary waves manifested as the ridge around $\lambda \sim 150^\circ$ and the cyclones around $(\lambda, \phi) \sim (330^\circ, \pm 60^\circ)$ (Fig. 4.6b). The pressure signatures are generally geostrophic, and have an equivalent barotropic vertical structure suggested by the low surface pressure signatures below the upper level low pressure area (Fig. 4.6a).

The deep, broad equatorial westerly wind transports a large amount of sensible and latent heat to the night side, which is manifested as the warm and moist tongue in the lower to the middle troposphere extending eastward crossing the terminator at $\lambda=180^\circ$ (Figs. 4.6c and

4.6d). A considerable portion (about one fourth) of the water vapor transported to the night side at $\lambda = 180^\circ$ returns to the day side at $\lambda = 360^\circ$ (figure not shown). At $\lambda = 180^\circ$, water vapor transport to the night side is more intense in the high-latitudinal regions than in the equatorial region, resulting from the meandering of the eastward wind associated with the intense wavenumber one stationary waves and near surface westward wind near the equator. Rainfall is no longer focused at the subsolar point, as it is associated with the moisture transport, and some amount of rainfall occurs even in the night hemisphere (Fig. 4.6e) despite the negligibly small amount of surface evaporation. Also due to the enhanced water vapor transport, the column integrated moisture content around the antisolar point reaches about three times that in Case $\Omega 0.0$ (Fig. 4.6g). Actually, column integrated moisture content increases considerably also on the day side; the peak value near the subsolar point in Case $\Omega 0.15$ is about 1.5 times the value of that in Case $\Omega 0.0$, and its associated greenhouse effect results in the rise of surface temperature following the drop near $\Omega^* \sim 0$ (Fig. 4.4a).

It is notable that the horizontal distribution of surface temperature closely follows that of column moisture content on the night side (Figs. 4.6g and 4.6h); in an extensive region of high column water vapor content in the low latitudes, surface temperature is high, whereas it is very low in the dry regions located around the low pressure centers of wavenumber one structure at higher latitudes. The energy budget at the ground surface explains this close relationship; because incoming solar flux is absent and both latent ($\sim 2 \text{ W m}^{-2}$) and sensible ($\sim -4 \text{ W m}^{-2}$) heat fluxes are negligibly small on the night side, the upward thermal radiation flux ($\sim 230 \text{ W m}^{-2}$) at the surface almost balances the downward longwave radiation from the atmosphere that is exclusively emitted by water vapor, the only radiatively active component in this model.

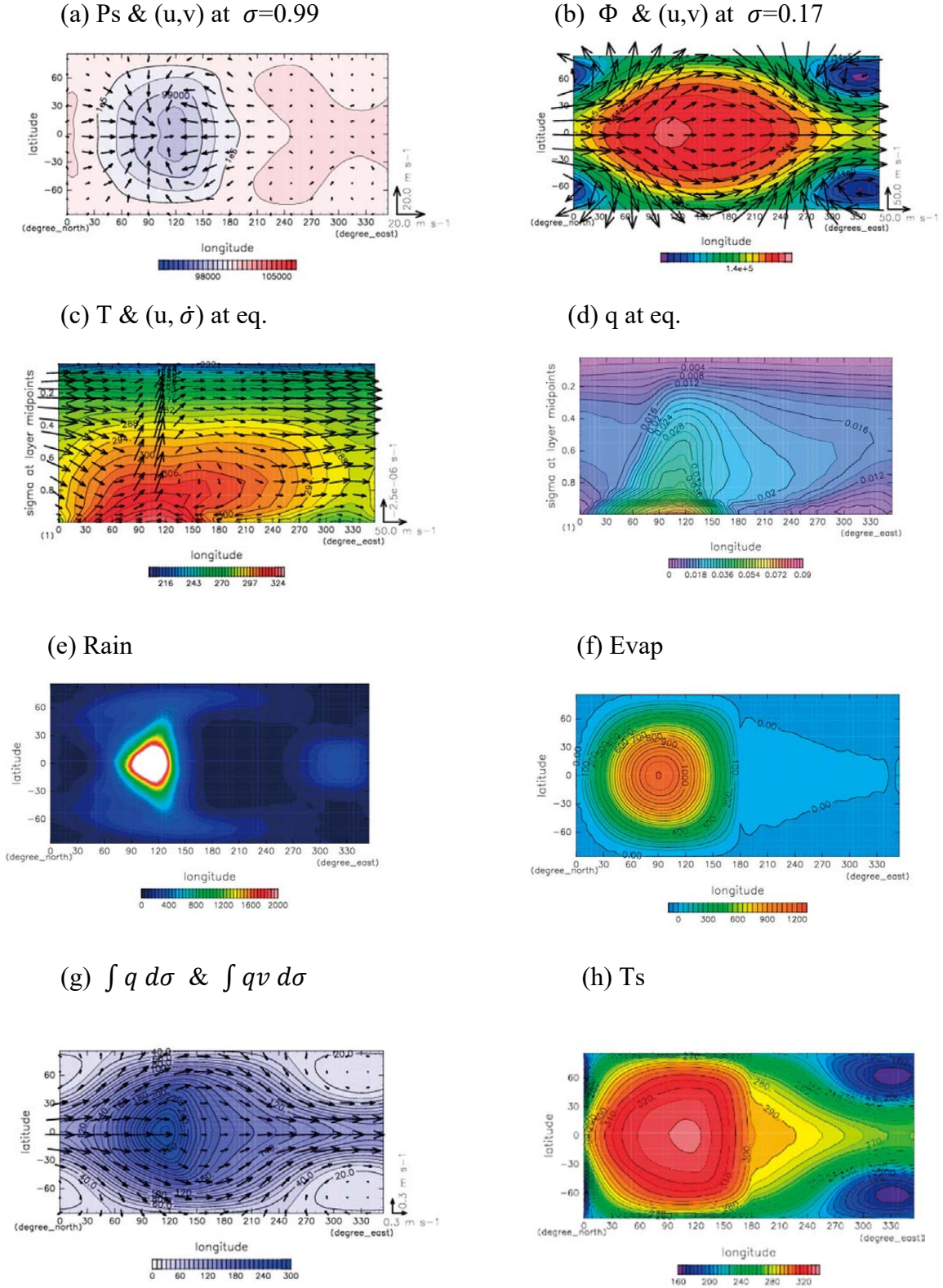


Figure 4.6 Same as Fig. 4.5 but for case $\Omega 0.15$, except that the unit vector in (b) is 50 m s^{-1} and the unit vector of vertical wind in (c) is $2.5 \times 10^{-6} \text{ s}^{-1}$. From Noda et al. (2017), Fig 6.

When all Type-II cases are compared, the broad equatorial jet is stronger for the cases with larger value of Ω^* as indicated in Fig. 4.7, where the values of mass weighted global mean zonal wind velocity in Type-II are shown. Moreover, for $\Omega^* \geq 0.2$, the wind speed is close to the absolute values of the intrinsic phase speed of the normal mode Rossby wave of Longuet-Higgins (1968). The thin line in Fig. 4.7 shows the intrinsic phase speed of the meridionally gravest normal mode Rossby wave with wave number one, which we calculate with the spectral method of Kasahara (1976). Considering the vertical structure of the waves appearing in Type-II, we assume an equivalent depth of 10000 m, which is the value for the barotropic mode in an isothermal atmosphere of 245 K. The rough coincidence of the speed of the broad eastward equatorial jet and that of the intrinsically westward propagating normal mode Rossby wave for each Ω^* suggests that the wavenumber one planetary scale stationary wave in Type-II is resonantly excited on the broad westerly jet. Other evidence for the resonant excitation is the Ω^* -dependence of the amplitude and phase of the stationary wavenumber one waves. The cyclonic regions associated with the waves are expressed as the north-south symmetric cold regions in the night side mid to high latitudes (Fig. 4.3). For Ω^* from 0.05 to 0.2, the amplitude of the cyclonic regions is generally large. The longitudinal phase difference between the precipitation maximum and the cyclonic centers is about 270° for $\Omega^*=0.05$. This is the largest eastward phase shift of the upper Rossby wave response to a wavenumber one thermal forcing in a westerly flow faster than the resonant speed. As Ω^* increases, the phase difference decreases, dropping below 180° for $\Omega^*=0.25$ and 0.33 .

For $\Omega^* \geq 0.25$, the westerly wind does not reach the normal mode Rossby wave speed. Our preliminary analysis reveals that, in these cases, mid-latitude transient disturbances, which may originate from baroclinic instability given the development of meridional temperature gradient (not shown), transport westerly momentum poleward and decelerate the broad westerly jet. Detailed analysis on the nature of the transient disturbances and their possible role as the “governor” of the equatorial jet remains to be performed.

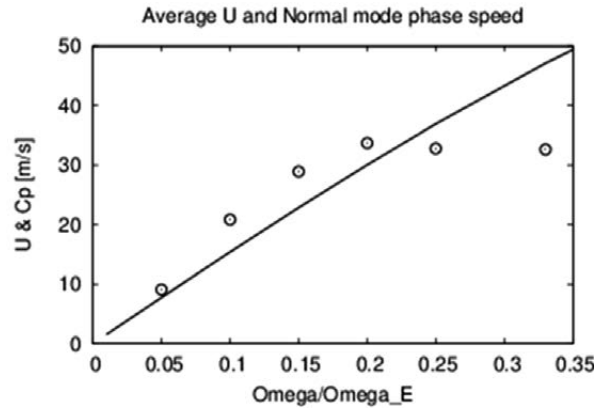


Figure 4.7 Mass weighted global mean zonal wind velocity for cases with Ω^* from 0.0 to 0.33 (circles). Absolute value of westward phase velocity of the zonal wavenumber one gravest Rossby normal mode is indicated by the thin line for comparison. From Noda et al. (2017), Fig. 7.

4.4.3 Type-III: Long time scale north-south asymmetric variability (Case $\Omega 0.75$)

The Type-III atmospheric circulation structure appears on the small- Ω branch for $0.5 \leq \Omega^* \leq 0.8$. The temporally averaged characteristics of Type-III are similar to those of Type-II in terms of the strong eastward equatorial jet, but, as shown in Fig. 4.4d, differ in the presence of significant north-south asymmetric long time scale variability.

Before considering the Type-III circulation structure in detail, we summarize the Ω^* dependences of the amplitude and the typical oscillation period of the north-south asymmetric variability. Fig. 4.8 compares the time series of zonal mean surface pressure in four cases with different values of Ω^* . In Case $\Omega 0.2$, where Type-II structure develops, a quasi periodic oscillation with amplitude of ~ 20 hPa and a temporal scale of ~ 10 days is notable. In Case $\Omega 0.5$, in addition to an oscillation with ~ 20 day period, a slower, north-south asymmetric variability is evident; its period and amplitude are ~ 40 -100 days and ~ 45 hPa, respectively. In cases with larger Ω^* , the slow, north-south asymmetric variability is more intense and its characteristic period is longer; in Case $\Omega 0.67$, the amplitude is ~ 80 hPa, and the period is ~ 1000 days. In Case $\Omega 0.75$, the amplitude is as large as ~ 160 hPa, and, looks almost permanent in Fig. 4.8d. However, by conducting several extended experiments, we have confirmed that the asymmetry does change its sign over a long time; the pressure deviation reverses at around $t=25000$ days for the run shown in Fig. 4.8d. Furthermore, the sign of the asymmetry is determined by chance; in the ten runs conducted for $\Omega 0.75$, Type-III structure appears in four runs (not shown), and, during the period shown in Fig. 4.8d, two of them have a positive pressure anomaly in the northern high latitudes, and the remaining two are negative. We conclude that, despite the development of the distinct long time scale north-south asymmetric variation, the structure of the atmospheric circulation is, in a statistical sense, north-

south symmetric, consistent with the symmetry of the applied solar flux.

Considering the characteristics of the north-south variation, we examine Case $\Omega 0.75$ as representative of Type-III, where the north-south asymmetry appears as a quasi stationary structure that persists throughout the 1000 days of the temporal average. As shown in Fig. 4.8d, northern (southern) high latitudes are occupied by high (low) pressure throughout the averaging period. The north-south asymmetric features discussed below are naturally reversed in the time period when the surface pressure in the northern (southern) hemisphere is low (high). We also note that the north-south asymmetric atmospheric circulation features develop also in GCM experiments with higher horizontal resolution (T42 and T85), although they appear in slightly different ranges of Ω^* (see Section 4.6), so we believe their emergence itself is insensitive to model resolution.

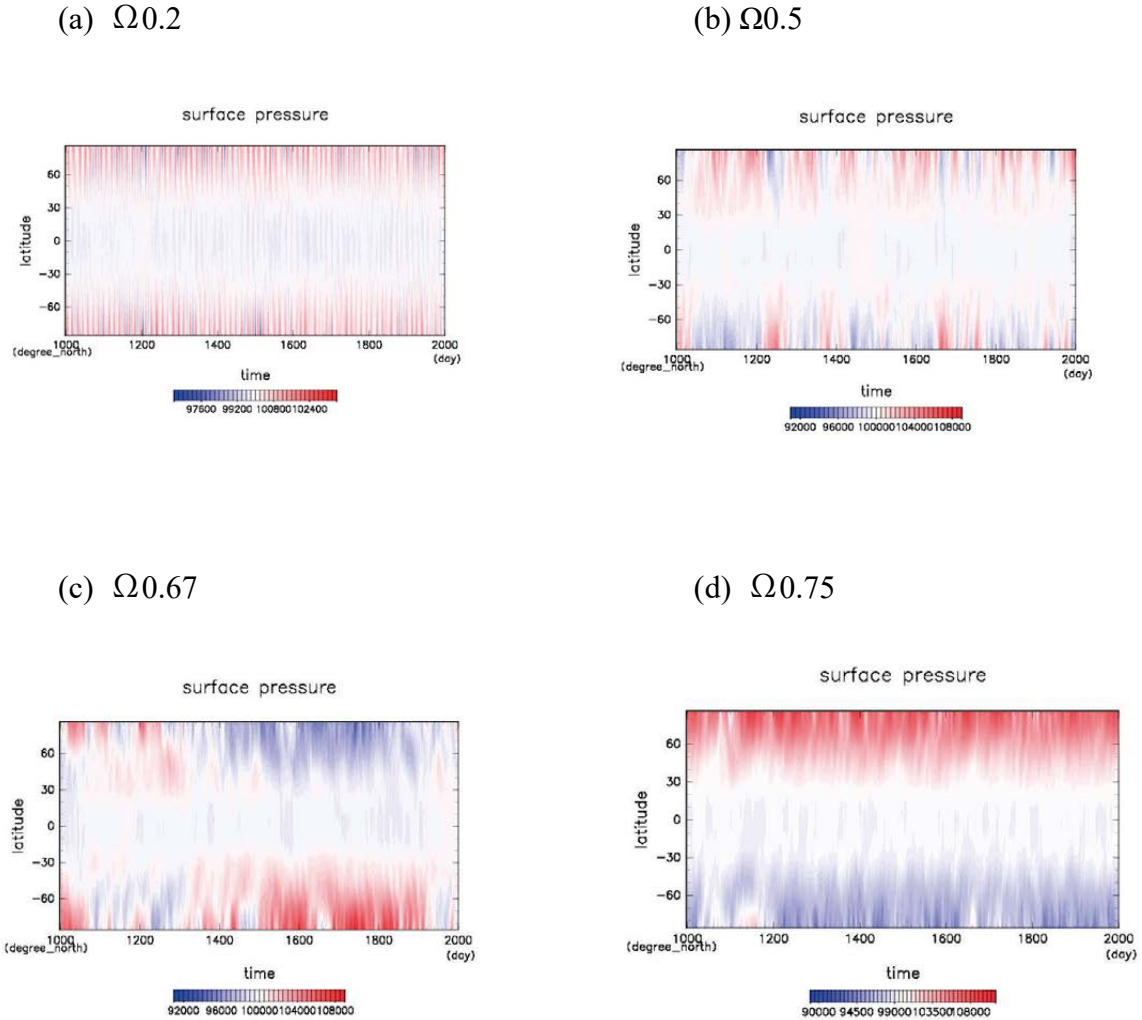
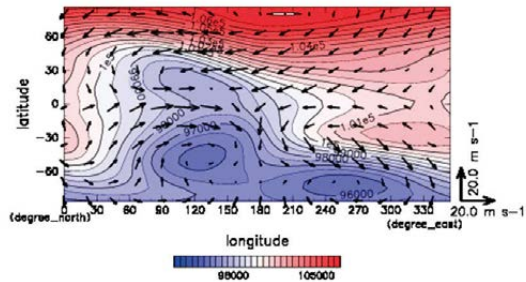
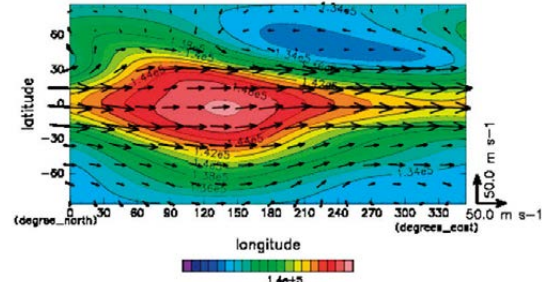
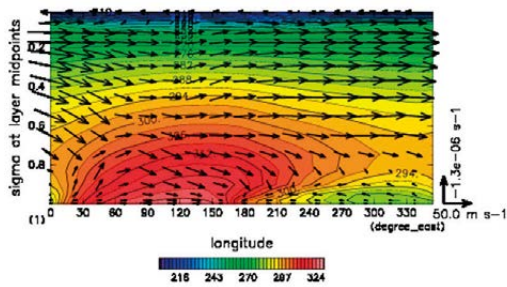


Figure 4.8 Latitude--time distribution of zonal mean surface pressure [Pa] for (a) $\Omega 0.2$, (b) $\Omega 0.5$, (c) $\Omega 0.67$, and (d) $\Omega 0.75$. From Noda et al. (2017), Fig. 8.

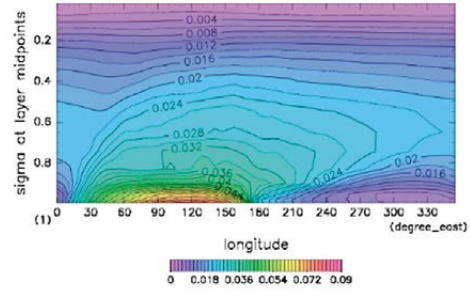
The time mean structure of the atmospheric circulation in case $\Omega 0.75$ is shown in Fig. 4.9. The deep westerly flow along the equator (Fig. 4.9bc), and the associated eastward advection of water vapor (Fig. 4.9dg) resulting in a warm belt along the equator in the night hemisphere (Fig. 4.9h), are features similar to those in Type-II (Fig. 4.6). However, except for the distribution of evaporation, which is strongly constrained by insolation as was discussed for Type-II, most of the off-equatorial features exhibit north-south asymmetry in contrast to the north-south symmetry in Type-II. Northern (southern) high latitudes are covered with surface high (low) pressure (Fig. 4.9a). The low pressure area in the day hemisphere also exhibits north-south asymmetry; the low pressure center in the southern hemisphere is much more intense than its counterpart in the northern hemisphere. Being in geostrophic balance with the pressure gradient around the polar pressure anomalies, north-easterly (north-westerly) wind prevails at the surface in northern (southern) mid latitude (arrows in Fig. 4.9a). This brings dry (moist) air into the mid latitudes of the day (night) hemisphere (Fig. 4.9g) crossing the day-night boundary at $\lambda=180^\circ$, inducing the north-westward (south-eastward) development of the mid-latitude precipitation zone (Fig. 4.9e) and the north-south asymmetry of surface temperature in both the day and night hemispheres (Fig. 4.9h) through the anomaly in downward thermal radiation.

Two additional features characterize the north-south asymmetry. First, the westerly region extends farther poleward in the southern hemisphere than in the northern hemisphere (Fig. 4.10a), where intense baroclinic disturbances develop (not shown here), presumably transporting westerly momentum downward. Second, there is a baroclinic zonal wavenumber one feature (Fig. 4.9ab) which has markedly north-south asymmetric meridional phase tilt (Fig. 4.10b); the phase lines tilt from northwest to southeast in a wide latitudinal zone from the northern high latitudes ($\phi \sim +70^\circ$) to southern mid latitudes ($\phi \sim -40^\circ$), crossing the equator. The phase tilt of the zonal wavenumber one feature, which implies southward transport of westerly momentum from northern to southern hemispheres, presumably contributes to driving the mid-latitude westerly jet in the southern hemisphere noted above (Fig. 4.10a).

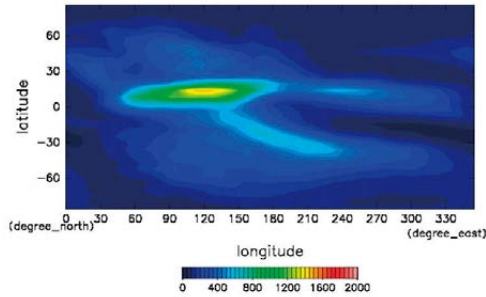
According to our preliminary analysis (not shown here) of the vorticity sources following the formulation of Sardeshmukh and Hoskins (1988), the meridionally tilted wavenumber one feature seems to be forced jointly by tropical and extratropical precipitation (Fig. 4.9e); the heating near the subsolar point, which is distributed mainly in the northern tropics around $(\lambda, \phi)=(120^\circ, +12^\circ)$, can be regarded as an excitation source of a Rossby wave that contributes the northern half of the wavenumber one structure. Meanwhile the latent heating associated with the precipitation band in southern mid latitudes distributed around $(\lambda, \phi)=(180^\circ, -30^\circ)$, can be regarded as an excitation source of a Rossby wave that contributes the southern half. Upward cascade of baroclinic eddies developing in the westerly jet could also contribute to the southern half. The distribution of mid-latitude precipitation seems to be, in turn, induced by the north-south asymmetry of moisture flux associated with surface pressure as described in the previous paragraph. Combining these features, the north-south asymmetry may possibly be maintained through a positive feedback loop, so that the asymmetry tends to have long life time. Quantitative examination of the dynamics of this possible feedback loop remains for future studies.

(a) Ps & (u,v) at $\sigma=0.99$ (b) Φ & (u,v) at $\sigma=0.17$ (c) T & (u, σ) at eq.

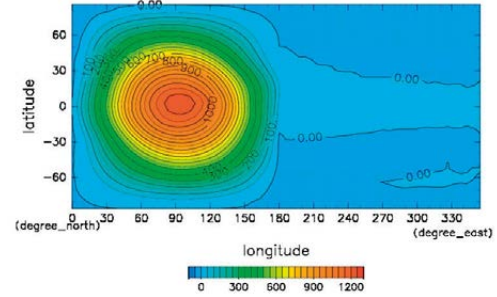
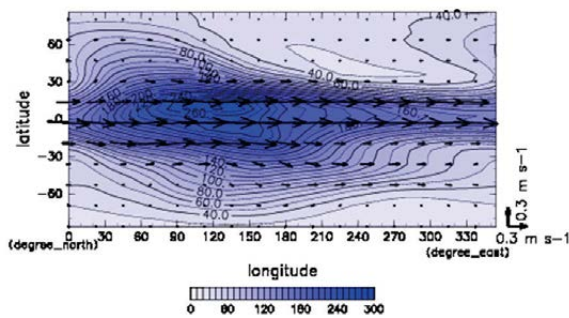
(d) q at eq.



(e) Rain



(f) Evap

(g) $\int q d\sigma$ & $\int qv d\sigma$ 

(h) Ts

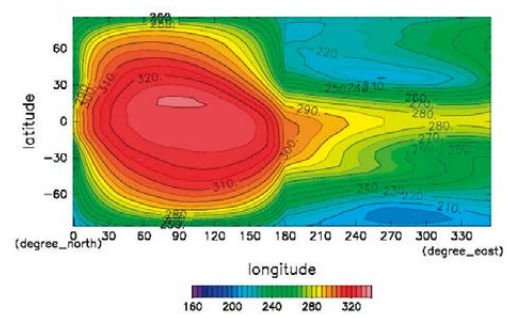
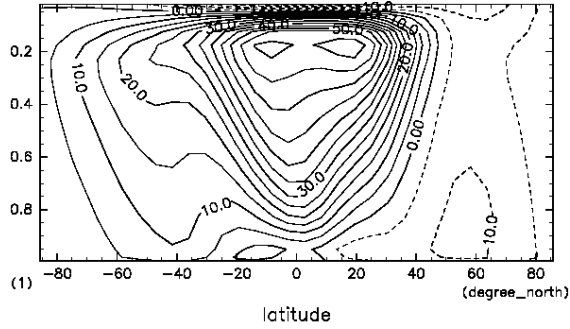


Figure 4.9 Same as Fig. 4.6 but for case $\Omega 0.75$, except that the unit vector of vertical wind in (c) is $1.3 \times 10^{-6} \text{ s}^{-1}$. From Noda et al. (2017), Fig. 9.

(a) Zonal mean zonal wind



(b) Eddy Stream Function at $\sigma=0.17$

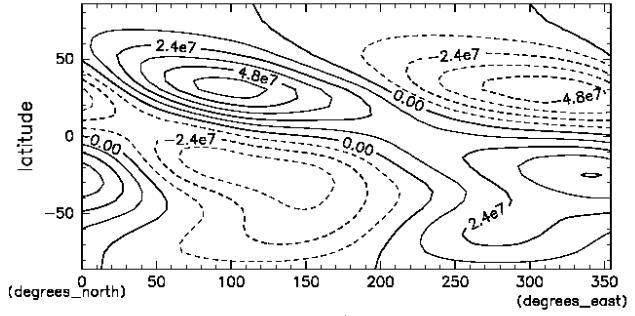


Figure 4.10 Structure of the atmosphere averaged from day 1000 to day 2000 for case $\Omega 0.75$: (a) zonal mean zonal wind, and (b) eddy stream function at $\sigma=0.17$. From Noda et al. (2017), Fig. 10.

4.4.4 Type-IV : Mid-latitude westerly jets (Case $\Omega 1.0$)

The Type-IV atmospheric circulation structure is found over the entire large- Ω branch for $\Omega^* \gtrsim 0.7$, and is characterized by somewhat Earth-like mid- to high- latitudes westerly jets. This is similar to the structures obtained by Merlis and Schneider (2010) and Edson et al. (2011) with $\Omega^* = 1$. We examine Case $\Omega 1.0$ as a representative case of Type-IV.

The time mean structure of the atmospheric circulation in case $\Omega 1.0$ is shown in Fig. 4.11. The mid latitudes are occupied by westerly winds through the whole depth of the troposphere (Fig. 4.11a and Fig. 4.11b). The low latitudes are occupied by easterly wind, but only in the upper troposphere. The lower tropospheric circulation along the equator (Fig. 4.11c) is more strongly controlled by the day-night contrast; zonal wind near the surface converges to form the upward motion at the subsolar point, and diverges around the antisolar point compensated by the broad downward motion. In the off-equatorial latitudes, latitudinal tilting of zonal wavenumber one wave features are notable, but these have generally baroclinic vertical structure, in contrast to the barotropic Rossby wave in Type-II. Polar regions are covered with deep low pressure areas. The precipitation and water vapor distributions are more complicated than those on the small- Ω branch. Precipitation (Fig. 4.11e) is most intense in a zonally aligned V-shaped region extending from the equatorial point $(\lambda, \phi) \sim (110^\circ, 0^\circ)$ to $(\lambda, \phi) \sim (30^\circ, \pm 25^\circ)$, loosely overlapping the low pressure area in the western part of the day hemisphere (contours in Fig. 4.11a). The wings of the V-shaped precipitation region intrude into the night side from the regions around $\phi = \pm 25^\circ$ at $\lambda = 360^\circ$. There is also a pair of zonally elongated precipitation zone in the higher latitudes, which start at $(\lambda, \phi) \sim (45^\circ, \pm 45^\circ)$ and extend to $(\lambda, \phi) \sim (330^\circ, \pm 80^\circ)$ on the night side. The distribution of column integrated water vapor content roughly follows that of precipitation (Fig. 4.11g), but the areas of greatest moisture content are located far from the equator, poleward of the high-latitude parts of the equatorial V-shaped strong precipitation area at $(\lambda, \phi) \sim (30^\circ, \pm 30^\circ)$.

The distribution of night side surface temperature (Fig. 4.11h) closely follows that of the atmospheric water vapor content (Fig. 4.11g) as in the cases on the small- Ω branch. However, reflecting the complex structure of humidity, temperature varies longitudinally; it is warmer to the east along $\phi \sim \pm 30^\circ$, whereas it is warmer to the west along $\phi \sim \pm 50^\circ$. Also the distribution of surface temperature on the day side is affected by the distribution of water vapor content; the highest surface temperature appears at $(\lambda, \phi) \sim (80^\circ, \pm 40^\circ)$, the locations that are quite far from the subsolar point and below the belts of large water content (deep blue colors of Fig. 4.11g). The values of surface temperature at the subsolar and antisolar points are lower than the respective values in Types -II or -III (Figs. 4.4a and 4.4b) resulting from the reduction of atmospheric water content compared to those cases.

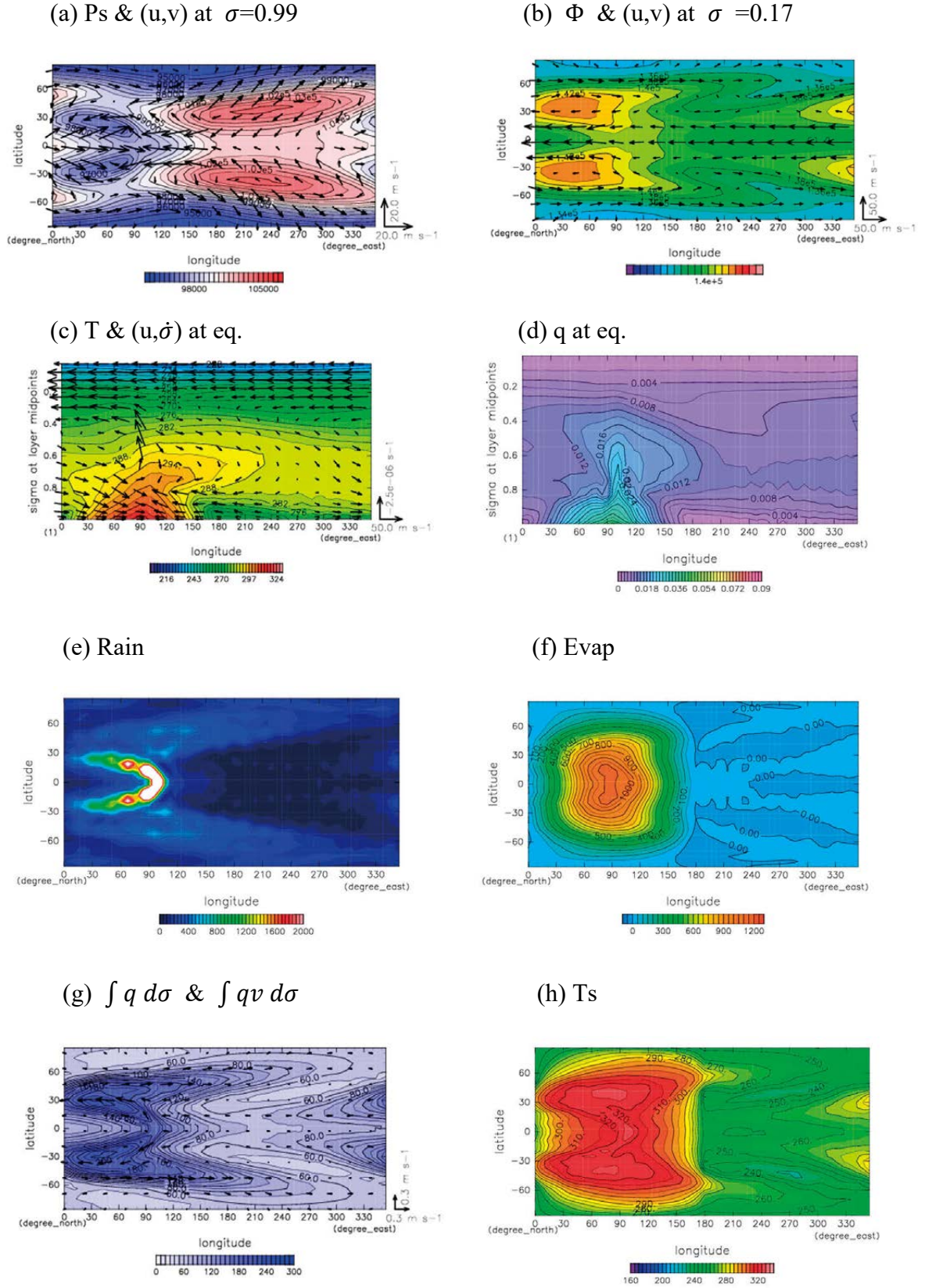


Figure 4.11 Same as Fig. 4.9 but for case $\Omega 1.0$ except that unit vector of the vertical wind in (c) is $2.5 \times 10^{-6} \text{ s}^{-1}$. From Noda et al. (2017), Fig. 11.

4.5 Day-night energy transport

4.5.1 Dependence on Ω^*

In this section, we examine how day-night energy transport changes with Ω^* , responding to the considerable variation of the atmospheric circulation structure described in the previous section. We analyze OLR on the night side, F_{OLR} , day-night dry static energy transport, F_{sens} , and day-night latent energy transport, F_{lat} , which, in equilibrium states, satisfy the energy balance of the night side:

$$T_{sens} + T_{lat} - 2 \pi R_p^2 F_{OLR} = 0 \quad (4.3)$$

T_{sens} and T_{lat} are calculated assuming the approximate balances of heat and moisture budgets in the night side atmosphere, which are

$$2 \pi R_p^2 (F_{SLR} + F_{sens} - F_{OLR} + LP) + T_{sens} = 0 \quad (4.4)$$

$$2 \pi R_p^2 (F_{evap} - P) + T_{lat} / L = 0 \quad (4.5)$$

where F_{evap} is surface evaporation flux, F_{SLR} is net upward longwave radiation flux at the surface, F_{sens} is surface sensible heat flux, P is precipitation, and L is latent heat of water vapor. All of the terms are 1000-day mean values spatially averaged over the night side.

Fig. 4.12 shows Ω^* dependences of, F_{OLR} , $T_{sens} / (2 \pi R_p^2)$, and $T_{lat} / (2 \pi R_p^2)$. All 10 runs are plotted for each value of Ω^* . The most remarkable feature is that total energy transport is almost unchanged regardless of the branch of the solution and the value of Ω^* , while the partition into F_{sens} and F_{lat} changes. For $\Omega^* \sim 0$, where the Type-I structure appears, F_{lat} is negligible, as atmospheric water vapor content is very small (Fig. 4.5g). As Ω^* increases and the Type-II structure appears, F_{lat} rapidly increases, but F_{sens} decreases correspondingly, keeping the sum of the two (F_{OLR}) almost unchanged. The increase of F_{lat} results from the development of the deep broad westerly wind (Figs. 4.6b and 4.6c) together with the increase of moisture in the day hemisphere (Fig. 4.6d). Further increase of F_{lat} and decrease of F_{sens} continue for larger Ω^* as the Type-III with north-south asymmetric variability appears. F_{lat} exceeds F_{sens} at $\Omega^* = 0.33$ and F_{lat} reaches about twice F_{sens} at the large- Ω end of the small- Ω branch ($\Omega^* = 0.8$). Still, the sum of the two (F_{OLR}) is kept almost constant. At the transition from the small- Ω branch to the large- Ω branch around $\Omega^* \sim 0.75$, F_{lat} suddenly reduces by about half. Nevertheless, an equally abrupt increase of F_{sens} means that total heat transport changes only a little. The decline of F_{lat} at the transition results from the associated disappearance of the broad westerly wind at low latitudes. The type-IV structure has a pair of deep mid-latitude westerly jets blowing through the day and night sides (Fig. 4.11b), but they cannot transport as much water vapor as the broad equatorial westerly wind in the Type-II or Type-III cases, because the water vapor mixing ratio in the mid latitudes is smaller than in the lower latitudes. The variation of total day-night energy transport is less than 2% over the wide range of Ω^* , while the atmospheric circulation structure varies

considerably. Day-night total energy transport scarcely depends on the atmospheric circulation structure.

We have already seen in Fig. 4.4b that surface temperature at the antisolar point changes greatly with the change of Ω^* . This seems perplexing, since day-night total energy transport is almost constant. However, if we examine the hemispherically averaged temperature, the change is only modest. Fig. 4.12b shows Ω^* dependences of surface temperature averaged over the night side, the day side, and the whole globe. The range of the variation of night side average temperature is around 10 K, which is much smaller than the variation at the antisolar point of almost 50 K (Fig. 4.4b). This results from the compensation between the temperature variations in the lower and higher latitudes; in Type-II and Type-III, surface temperature in the low latitudes including the antisolar point is high, while regions of low surface temperature appear in the higher latitudes associated with the large amplitude Rossby waves (Fig. 4.3b-m). The remaining modest changes of averaged temperatures can be explained mainly by the change of mean column water vapor content.

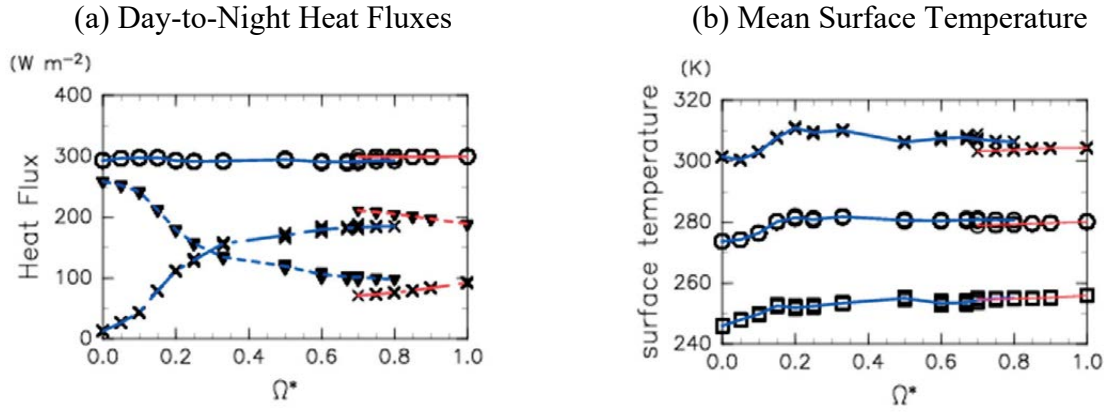


Figure 4.12 (a) Ω^* dependences of outgoing longwave radiation on the night side, F_{OLR} (\circ), day-night dry static energy transport per unit area, $T_{sens} / (2\pi R_p^2)$ (black triangle), and day-night latent energy transport per unit area, $T_{lat} / (2\pi R_p^2)$ (\times). Units are [W m^{-2}]. All 10 runs for each Ω^* case are plotted. Blue and red lines represent ensemble averages for the small- Ω and the large- Ω branches, respectively. (b) Same as (a) but for global mean (\circ), day side mean (\times), and night side mean (Box) of surface temperature [K]. From Noda et al. (2017), Fig. 12.

4.5.2 Moist atmosphere radiation limit constraint

As described in the previous subsection, the total amount of day-night energy transport is found to be insensitive to the change of Ω^* and to the associated change of atmospheric circulation structure. The invariance of day-night total energy transport is equivalent to the invariance of day side OLR, because the day-night total energy transport is equal to the difference between the day side OLR and the incoming solar flux; the latter is constant in the present study. It has been recognized that, in the framework of a one-dimensional radiative convective equilibrium model, the value of OLR from the atmosphere on a water covered planet can not exceed the radiation limit. In the following, we attempt to understand the invariance of day-night energy transport in relation to the constraint on the day side OLR from the radiation limit of a moist atmosphere.

Fig. 4.13 shows the relationship between surface temperature and OLR on the day side obtained by the present GCM calculations superposed on the relations obtained by the one-dimensional radiative convective equilibrium model described in Chapter 3 with several specified values of tropospheric relative humidity. The relationship between surface temperature and OLR is sampled at the grid points within the $120^\circ \times 120^\circ$ rectangular region centered on the subsolar point from the run for each Ω^* described in the previous section.

In all the GCM runs, the maximum values of OLR are between 400 and 430 W m^{-2} , and lie under the values of the radiation limits in the one-dimensional calculation, given that the values of relative humidity averaged over the troposphere on the day side of the GCM runs are within the range 60-80%. Moreover, in each of the GCM results, the relationship between surface temperature and OLR roughly follows those obtained in the one-dimensional calculations. These results imply that the day side OLR in the present GCM calculations is constrained by the radiation limit of a moist atmosphere on a water covered planet. Now recalling that the system is in a statistically equilibrium state, the amount of day-night total energy transport should be equal to the difference between the incoming solar flux and the radiation limit of a moist atmosphere. The results of our GCM calculations indicate that the change in atmospheric circulation structure associated with the change of Ω^* does not modify drastically the mean value of atmospheric humidity, and hence does not affect the value of the radiation limit. This explains the general insensitivity of day-night energy transport to Ω^* obtained in the present GCM calculations.

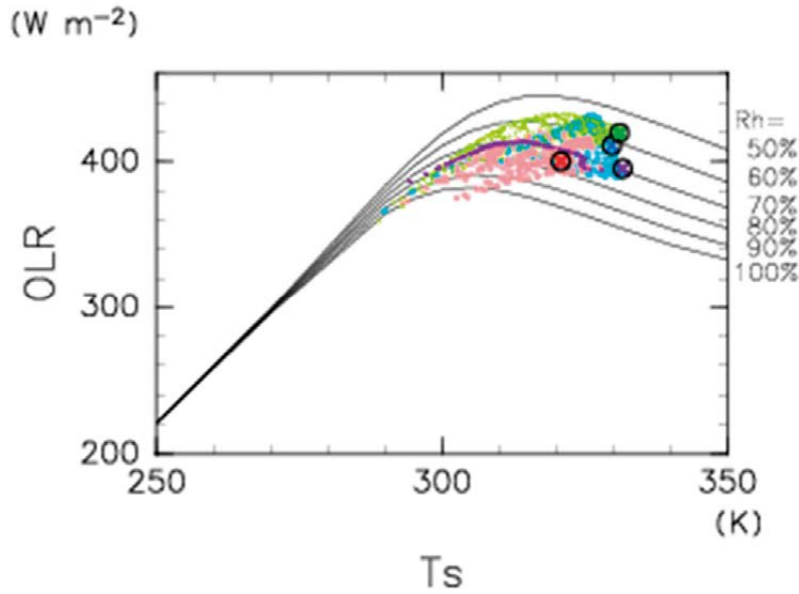


Figure 4.13 Relationships between surface temperature and OLR obtained by the GCM and by the one-dimensional (vertical) radiative-convective equilibrium model. The GCM results are shown as colored dots: purple, light blue, green, and pink dots indicate runs $\Omega = 0.0, 0.15, 0.75$, and 1.0 , respectively. Data are from the grid points in the $120^\circ \times 120^\circ$ rectangular region centered on the subsolar point. Crosses in black circles indicate the values at the subsolar point. Black lines are the one-dimensional model results with tropospheric relative humidity of (in order from the top) 50, 60, 70, 80, 90, and 100 %, respectively. From Noda et al. (2017), Fig. 13.

4.6 Dependence on resolution

Because of the large number of experiments required to examine the Ω^* dependence of circulation structures, including the possibility of multiple equilibrium solutions, the horizontal resolution of the GCM used in this study is limited to T21. In this section, we check the resolution dependence of the results, by briefly describing the results obtained in models with higher resolution, T42 and T85, focusing on some of the features that may be resolution sensitive. For T42, we have performed 10 runs for each of several selected values of Ω^* . For T85, only one run was performed for each values of Ω^* . In a qualitative sense the main results, namely the existence of the four types of solutions, are not sensitive to the model's resolution, as shown below. Figs.4.15a and 4.15b show the upper tropospheric zonal mean zonal wind at the equator for various values of Ω^* in the T42 and T85 models, respectively; for T42, all runs for each Ω^* are plotted. These figures share the main features seen with T21 resolution (Fig.4.4c): there are two branches of solutions, and the equatorial zonal wind velocity for each Ω^* is insensitive to the resolution. And, at least in the T42 model, the two branches coexist over a range of Ω^* giving multiple equilibria, although the values of Ω^* with multiple

equilibria are about 0.1 smaller than in the T21 model. In the case of the T85 model, as we can only perform one run for each Ω^* , the existence of multiple equilibria cannot be confirmed. However, the overall behavior is not inconsistent with that in T42; the value of Ω^* for the upper end of the small Ω branch is the same.

Fig. 4.14 shows the values of mass weighted zonal mean wind speed for different values of Ω^* obtained in the runs with T21, T42 and T85 resolutions, compared with the intrinsic phase speed of the Rossby wave normal mode. In a qualitative sense, we can confirm the main features described in Section 4.4.2; i.e., the mass weighted zonal mean wind speed closely follows or slightly exceeds the Rossby wave phase speed for $0.0 \lesssim \Omega^* \lesssim 0.2$, and levels off for larger Ω^* . The only slight exception is $\Omega^* 0.15$ in T85, where the zonal mean wind is decelerated by transient disturbance whose nature is unclear.

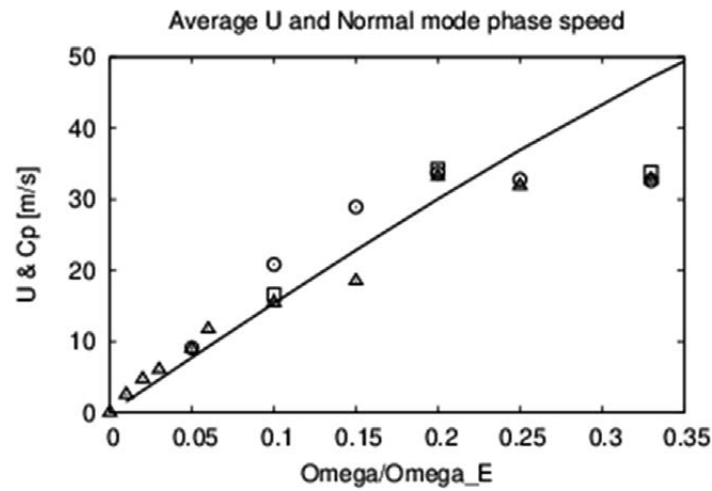


Figure 4.14 Same as Fig. 4.7, but showing values for horizontal resolutions of T42 (squares) and T85 (triangles) in addition to those for T21 (circles). From Noda et al. (2017), Fig. A.2.

Figs. 4.15c and 4.15d show the measure of the north-south asymmetry of surface temperature defined by Eq. 4.2 for various values of Ω^* in the T42 and T85 models, respectively; for T42, all runs for each Ω^* are plotted. Compared to the corresponding figure for T21 resolution (Fig. 4.15d), the degree of north-south asymmetry seems to be weaker in higher resolution models. Still, we can identify features largely free from resolution dependence: the monotonic increase of the degree of north-south asymmetry on the small- Ω branch, and the smaller degree of north-south asymmetry on the large- Ω branch. The temporal scales of the north-south asymmetric variability are of the same order of magnitude for all model resolutions (not shown). The spatial structure of the north-south asymmetric variability in Type III, i.e., toward the large- Ω^* end of the small- Ω branch, is also common to all model resolutions. Fig. 4.16 shows the horizontal structures of surface pressure in the T42 and T85

models for $\Omega^* = 0.6$ averaged for 500 days during which high (low) pressure occupies the north (south) pole. A comparison with Fig. 4.9a showing the structure of the variability for $\Omega^* = 0.75$ in the T21 model confirms that all resolutions share the same major features, such as the longitudes of the low pressure area in the southern day hemisphere and the high pressure area in the southern night hemisphere.

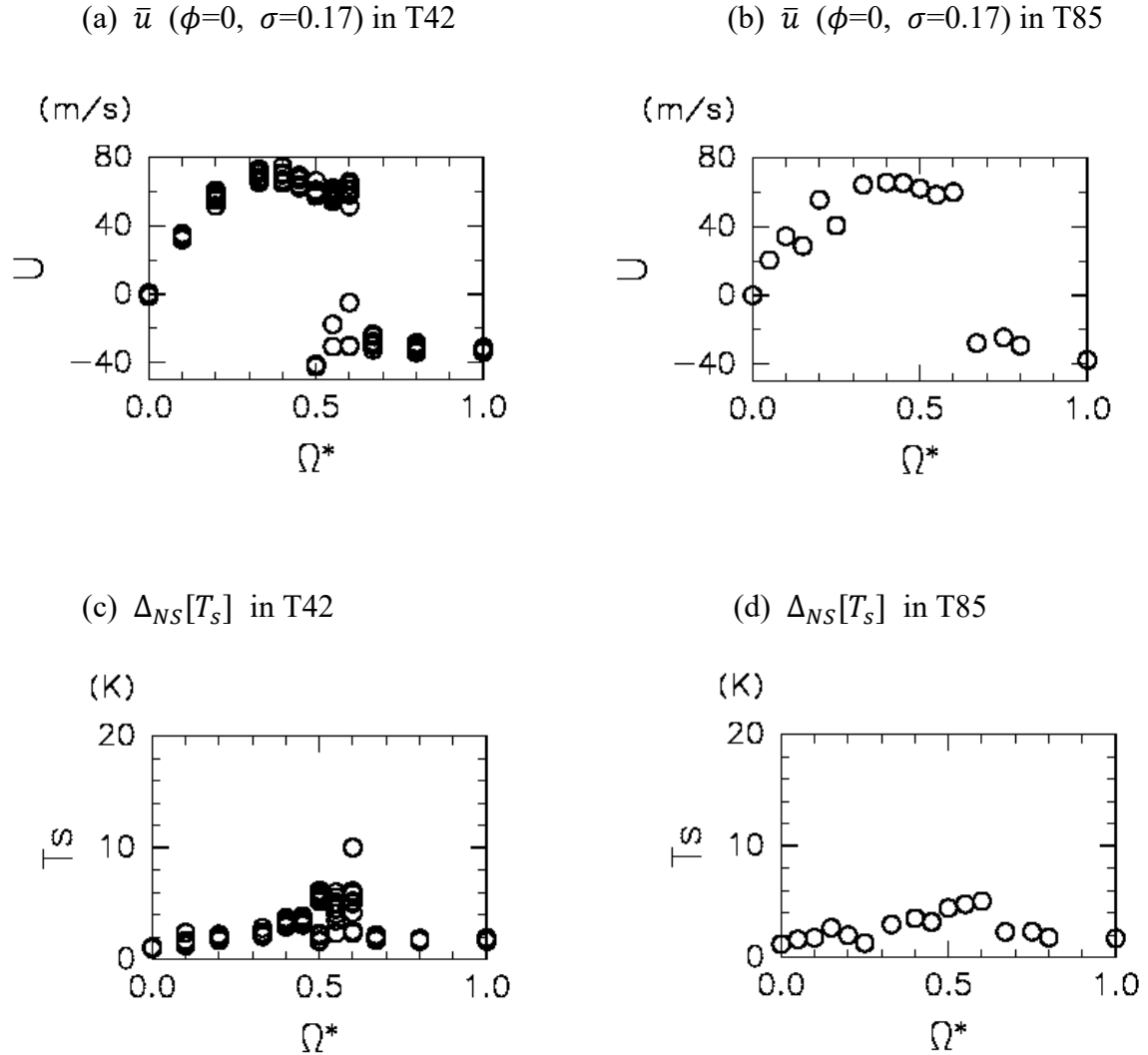


Figure 4.15 (a), (b) Same as Fig. 4.4c but for the T42 model (a) and T85 model (b), and (c), (d) same as Fig. 4.4d but for the T42 model (c) and T85 model (d). From Noda et al. (2017), Fig. A.1.

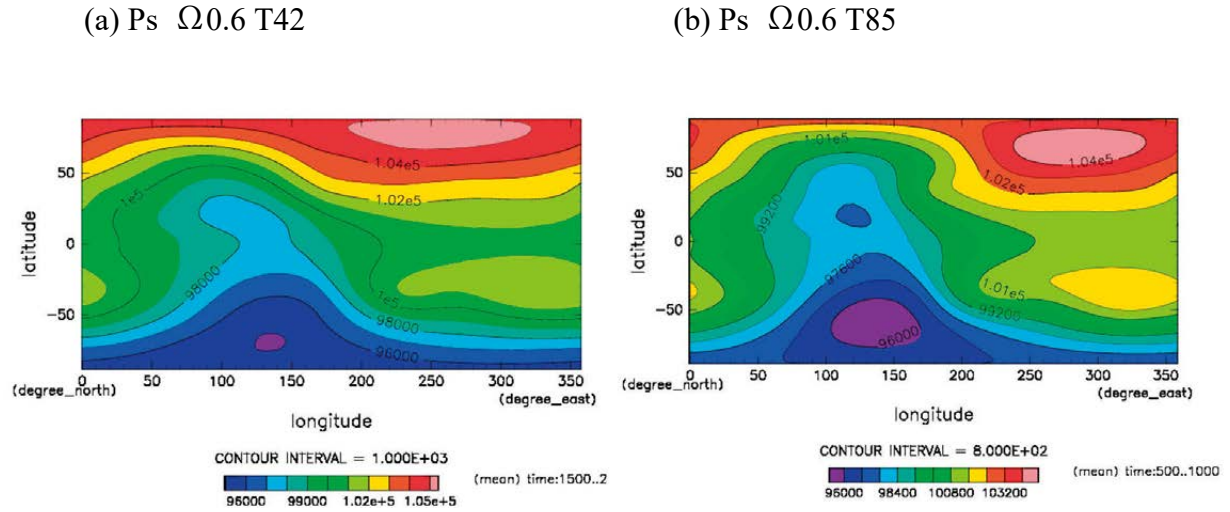


Figure 4.16 Mean surface pressure distributions for $\Omega 0.6$ in the T42 model (a) and T85 model (b) for 500 days during which high (low) pressure occupies the north (south) pole. From Noda et al. (2017), Fig. A.3.

4.7 Summary

Numerical experiments are performed using a cloud-free, swamp aquaplanet GCM with a gray absorption coefficient for longwave radiation and with the Earth's solar constant. The value of planetary rotation rate normalized by the Earth's value, Ω^* , is varied from 0 to 1. For all Ω^* cases, statistically equilibrium states are obtained; the runaway greenhouse state does not emerge. The circulation structures obtained are classified into four types: Type-I characterized by day-night convection, Type-II characterized by a broad equatorial westerly jet and a stationary Rossby wave, Type-III characterized by a long time scale north-south asymmetric variability, and Type-IV characterized by a pair of mid-latitudinal westerly jets. Types-I, II, and III evolve continuously from one to another as Ω^* increases, constituting one branch of the solution referred to as the small- Ω branch, whereas Type-IV belongs to a different branch referred to as the large- Ω branch (Fig.4.4). For $0.7 \lesssim \Omega^* \lesssim 0.8$, multiple equilibrium states emerge; both Type-III and Type-IV are allowed. The dependence of the amount of day-night energy transport on Ω^* is analyzed. It is confirmed that the amount is large enough to prevent the day side atmosphere from entering a runaway greenhouse state. Moreover, the amount is found to be almost insensitive to Ω^* despite the drastic change in the structure of the atmospheric circulation, although the partition into latent and sensible energy transports varies. Day side OLR in the experiments is analyzed and compared with the values obtained with a one-dimensional radiative convective model. The results strongly suggest that day side OLR is constrained by the radiation limit of a moist atmosphere; the details of the circulation structure do not greatly change atmospheric humidity, so the value of the radiation limit is unchanged. This explains the invariance of day-night energy transport, as it is equal to the difference

between incoming solar flux and day side OLR. The former is a constant prescribed amount in this study, and the latter is constrained by the radiation limit.

It should be useful to re-examine the circulation characteristics obtained in previous studies from the present viewpoint, since this study has performed a more complete investigation on their sensitivity to Ω^* than previous studies. The "slowly rotating regime" and the "rapidly rotating regime" identified by Merlis and Schneider (2010) presumably correspond to the small- Ω branch and the large- Ω branch in the present study, respectively. However, the correspondence is not certain because they present the horizontal distributions of atmospheric variables for only two values of Ω^* . Circulation structures similar to those of Type-I and Type-IV are obtained for those two values of Ω^* , but it remains unclear whether they obtained atmospheric structures similar to Type-II and Type-III. The dependence of the circulation structure on Ω^* obtained by Edson et al.(2011) can be compared with the results of the present study with more confidence. They observed two separate branches of solutions with multiple equilibria, and solutions with planetary waves of zonal wavenumber one superposed on broad westerly wind in the low latitudes for intermediate values of Ω^* . These features are similar to those obtained in the present study.

Chapter 5

Preliminary results obtained for cloudy atmosphere with non-gray radiation

5.1 Introduction

In Chapter 3, the occurrence condition of the runaway greenhouse state and the dependence of the climate on the solar constant were investigated using a gray radiation scheme. In this chapter, the preliminary results obtained by a GCM with a non-gray radiation scheme are presented shortly. The following two problems were examined:

- (I) Does an OLR upper limit exist also in non-gray radiation?
- (II) If an OLR upper limit exists, what determines the limit value?

Some experiments on the runaway greenhouse state in non-gray atmosphere have been performed using GCMs. Yang et al. (2013) discuss the occurrence condition of the runaway greenhouse state of synchronously rotating planets. Yang et al. (2013) showed that, with an atmosphere-ocean coupled model, the threshold value of solar constant for the occurrence of the runaway greenhouse state on synchronously rotating planets was larger than that for planets with an incoming solar flux distribution similar to that of the Earth's which have a diurnal change. As the reason for the difference in the threshold value, they proposed that the increase of albedo was caused by the generation of dense cloud around the subsolar point. Leconte et al. (2013) performed a GCM experiment with an increased solar constant for Earth's incoming solar flux distribution in order to consider the climate in the distant future when the value of solar constant will increase due to the time evolution of the Sun. They showed that equilibrium states were obtained with 375 W m^{-2} of the global mean incoming solar flux, which is a larger value than the OLR limit obtained by one-dimensional models. As the reason for the difference, they proposed that the intensification of drying in the subtropical region caused the increase in infrared radiation, which balanced the increased incoming solar flux. The results of these two studies seem to suggest that the occurrence condition of the runaway greenhouse state is determined in a complicated way according to model configuration.

However, we consider that the occurrence condition of the runaway greenhouse state is determined in a simpler way. From the results of Chapters 3 and 4, we suggest that the occurrence of the runaway greenhouse state is determined by whether the global mean incoming solar flux exceeds the OLR limit in all cases, although the threshold value of the solar constant for the occurrence of the runaway greenhouse state will change according to cloud distribution and/or incoming solar flux distribution. In this section, we examine the effect of cloud on the occurrence condition of the runaway greenhouse state using a GCM including a non-gray radiation scheme and a simple cloud model.

5.2 Model configuration

As for atmospheric constituents and radiation processes, case (2) (case for Earth's radiation) described in Section 2.4 was adopted. The amount of cloud water was calculated by solving the time-dependent equation of cloud water with a given cloud extinction time, as described in Section 2.5. The value of the cloud extinction time was set to 1500 sec for the cloudy case and 0 sec for the cloudless case. The value of the solar constant S was varied in the range between 1366 W m^{-2} and 2200 W m^{-2} . The value of planetary rotation rate Ω was varied in the range between 0.0 and 1.0. Two kinds of the distribution of incoming solar flux were considered:

- (1) Earth radiation case: distributions evaluated with the present terrestrial orbital parameters. The diurnal and seasonal cycles were considered.
- (2) Synchronously rotating planet radiation case: distribution shown in (Fig. 4.1). The entire surface was assumed to be a swamp ocean. The value of surface albedo was set to be 0.15. The resolution of GCM was T42L26.

5.3 Results

A numerical experiment with changing solar constant was performed for two kinds of distributions of incoming solar flux: cases (1) and (2) described in the previous section. Fig. 5.1 shows the results of all runs. The cross mark represents the result in which the value of the global mean OLR was smaller than the global mean absorbed solar flux and the global mean surface temperature kept increasing. These cases are considered to correspond to the runaway greenhouse state. The threshold values of the occurrence of the runaway greenhouse state were about 1600 W m^{-2} for the cloudless cases regardless of solar flux distributions. On the other hand, for the cloudy cases, the threshold values changed according to the solar flux distribution. The threshold values for the Earth radiation distribution cases were similar both for the cloudless case and the cloudy case. These values were almost the same as the value obtained by Leconte et al. (2013), 1500 W m^{-2} . The threshold values for the synchronously rotating planet distribution cases exceeded 2000 W m^{-2} .

As described above, the threshold value for the occurrence of the runaway greenhouse state changed according to model configuration, and the global mean incoming solar flux ranged from 450 W m^{-2} to 550 W m^{-2} . Contrary to the incoming solar flux, the difference in the threshold value of OLR was much smaller (Fig. 5.1b). The threshold values of OLR were about 300 W m^{-2} for all cases. It is considered that an upper limit of OLR exists also for cloudy atmospheres with non-gray radiation, and that the runaway greenhouse state emerges when the global mean incoming solar flux exceeds the OLR threshold value, i.e., 300 W m^{-2} . The values of relative humidity became small for cases in which the amount of absorbed solar flux increased. It is considered that the threshold values obtained in this experiment correspond to the OLR maximum value determined according to the values of relative humidity, since the OLR maximum value which an atmosphere can emit has a negative dependence on relative humidity. The difference in threshold values was larger than the difference in the maximum absorbed incoming solar flux and is considered to be caused by the difference in albedo. For the cloudy cases with $S=1366 \text{ W m}^{-2}$, the global mean albedo was 0.36 and 0.42 for the Earth radiation case and the synchronously rotating planet radiation case, respectively. The amount of cloud water at subsolar point for the synchronously rotating planet radiation case was larger than that for the Earth radiation case. The difference in the amount of cloud water caused the difference in albedo. The result that cloud water amount and albedo increase for the synchronously rotating planet radiation case is consistent with the results obtained by Yang et al. (2013).

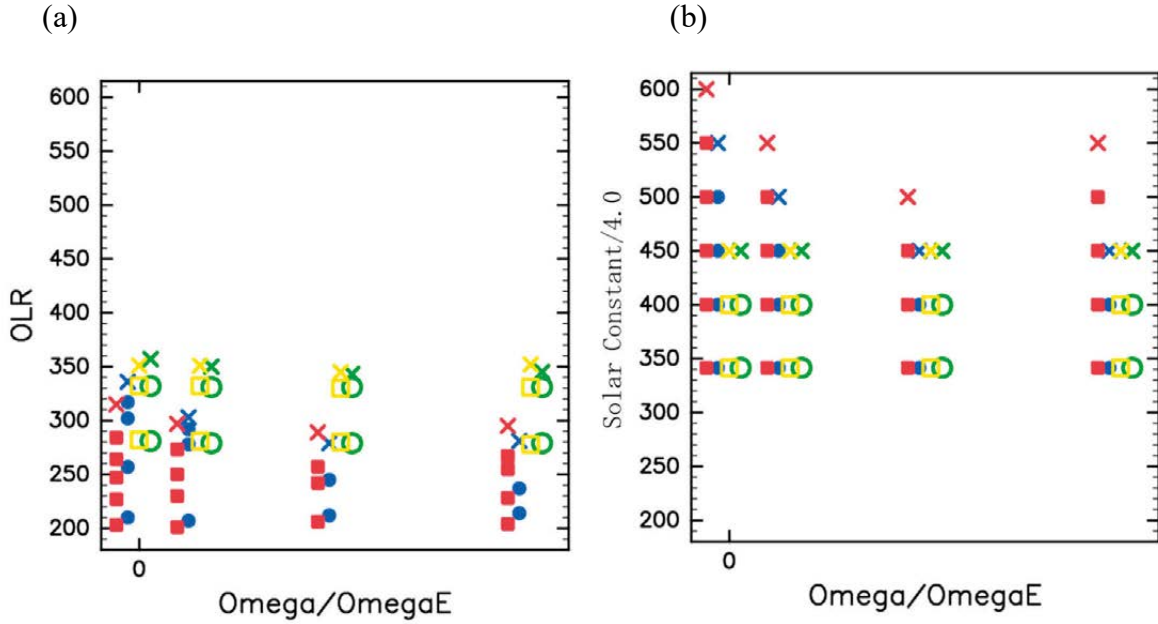


Figure 5.1 (a) Relationship between Ω^* and global mean OLR, (b) Relationship between Ω^* and solar constant divided by 4.0. The squares and circles represent the cases in which equilibrium states were obtained. The crosses represent the case in which the runaway greenhouse state emerged. The red marks represent the cloudy case with synchronously rotating planet distribution of solar flux. The blue marks represent the cloudy case with Earth-like distribution of solar flux. The yellow marks represent the cloud-free case with synchronously rotating planet distribution of solar flux. The green marks represent the cloudy case with Earth-like distribution of solar flux.

5.4 Summary

It is shown that, for the non-gray radiation cases, there exist OLR maximum values regardless of the existence of cloud or the distribution of incoming solar flux. The runaway greenhouse state emerges when the global mean incoming solar flux exceeds the OLR maximum value. This condition is the same as the occurrence condition of the runaway greenhouse state for gray atmosphere discussed in Chapter 3. These results suggest that the occurrence of the runaway greenhouse state is determined by a common condition regardless of model configuration.

It should be noted that there remains an important problem of the occurrence condition of the runaway greenhouse state for the non-gray radiation cases. The problem is to determine the radiation limit by using a vertical one-dimensional model with a non-gray radiation scheme used in this section, as discussed in Chapter 3, and to examine the correspondence of the threshold value obtained by the GCM experiment to the radiation limit.

Chapter 6

Conclusion and discussion

6.1 Summary

In this monograph, the results of numerical experiments using GCMs for various values of solar constant and two types of horizontal distribution of incoming solar radiation flux are described. With a simple model configuration such as gray radiation and swamp ocean, the following results were obtained.

- (a) The condition for the occurrence of runaway greenhouse state in the three-dimensional system is that the global mean value of incoming flux – i.e., not the maximum or the minimum of the latitudinal distribution of incoming flux – exceeds the upper limit of OLR. The results of a preliminary experiment using a non-gray radiation scheme also suggest that the occurrence of the runaway greenhouse state is determined by a common condition regardless of model configuration, that is, excess of the global mean incoming solar flux over the OLR maximum value.
- (b) Climate states of synchronously rotating planets were obtained for Earth's value of the solar constant. Statistically equilibrium states were obtained regardless of the value of planetary rotation rate, but the circulation structure changed drastically according to the values of planetary rotation rate. The amount of day-night energy transport was large enough to prevent the dayside atmosphere from entering a runaway greenhouse state and was almost insensitive to Ω^* . The invariance of the day-night energy transport was caused by the fact that the dayside OLR was constrained by the radiation limit.

The common conclusion for the above results is that the radiation limit is important for determining the climate of planets under various conditions: the radiation limit determines the value of the runaway threshold of solar constant even in three-dimensional systems and the amount of the day-night energy transport in synchronously rotating planets.

6.2 Ongoing problem and future plans

In numerical experiments described in this monograph, values of the solar constant larger than Earth's value were used. A drastic change in climate occurs also when the value of the solar constant is decreased from that of the present Earth, in which case a globally ice-covered state will occur. The globally ice-covered state has been discussed for examining the possibility of a snowball Earth state in the Neoproterozoic Era (e.g., Hoffman et al., 1998; Baum and Crowley, 2001).

One-dimensional energy balance models (EBMs) show that a slight decrease in the solar constant results in an ice-covered Earth (Budyko, 1969; Sellers, 1969). Budyko (1969) and Sellers (1969) discuss multiple equilibrium solutions: ice-free state, globally ice-covered state, and partially ice-covered state, using climate regime diagrams that show the existence ranges of climate states in the solar constant – ice-line latitude plane. In their model, Earth's radiation is parameterized in a very simple way and the runaway greenhouse state is not considered. The dependence of climate on the value of solar constant had not been examined with a model that includes both the runaway greenhouse state and globally ice-covered state until around the year 2000. Ishiwatari et al. (2007) is the first attempt to draw a climate regime diagram including the runaway greenhouse state. Ishiwatari et al. (2007) present a climate regime diagram

including both the runaway greenhouse state and globally ice-covered state, and they show the possibility of the coexistence of the ice-covered state, the partially ice-covered state, and the runaway greenhouse state for a given, common solar constant value. However, a model bug described in Chapter 3 was found in 2019, and the paper has been retracted. Therefore, we could not include the results of Ishiwatari et al. (2007) in this monograph. We have submitted the corrected paper (Ishiwatari et al., submitted to J. Geophys. Res.) based on a re-experiment with an appropriately corrected GCM.

In addition to the results described in this monograph, a new climate regime diagram that will be presented in the corrected paper (Ishiwatari et al., submitted to J. Geophys. Res.) will be a basic concept for considering the variety of climates and the habitability of exoplanets. However, the critical values of the occurrence of drastic climate changes may vary according to model configuration, such as the value of albedo, the details of the radiation scheme, the radiation effect of clouds, and so on. Especially, the dynamics of the ocean is undoubtedly an important element to be examined when considering the variety of climates. We are now preparing a paper on a solar constant dependence experiment for a horizontal distribution of solar flux adopted in Chapter 3 using an atmosphere-ocean coupled model (Kawai et al., in preparation). For the habitability of synchronously rotating exoplanets, the effect of ocean dynamics has been considered. Hu and Yang (2014) performed a series of climate simulations using a coupled atmosphere-ocean model with parameters following Gliese 581g. They found that the ocean contributed greatly to the day-night hemisphere energy transport and that the partition of the heat transport into atmospheric and oceanic transport varied considerably depending on the atmospheric CO₂ concentration and the incoming shortwave flux from the central star. The inclusion of a dynamically active ocean may possibly affect the insensitivity of day-night energy transport to the planetary rotation rate. This issue remains as a focus of future studies.

Acknowledgements

The numerical integrations were performed using the supercomputer (NEC SX series) of the Center for Global Environmental Research, National Institute for Environmental Studies, and the computational resources of RIKEN Center for Computational Science. The software and local computation/information environments were constructed by using the resources of GFD-DENNOU CLUB (URL; <http://www.gfd-dennou.org>). The source codes of the atmospheric general circulation model and the energy balance model are available at <http://doi.org/10.5281/zenodo.3514110>.

This study was supported by MEXT KAKENHI Grant Number JP23103003 of the Ministry of Education, Culture, Sports, Science and Technology, Japan JSPS KAKENHI Grant Numbers JP15740286, JP20540223, JP25400219, JP19H01947, the Astrobiology Center Program of the National Institute of Natural Sciences (NINS) (Grant Number AB311025), global COE program G11 "Foundation of International Center for Planetary Science" of the Japan Society for the Promotion of Science.

References

- Abe, Y., Matsui, T. (1988) Evolution of an impact-generated H₂O-CO₂ atmosphere and formation of a hot proto-ocean on earth. *J. Atmos. Sci.*, 45, 3081-3101.
- Arakawa, A., Suarez, M.J. (1983) Vertical differencing of the primitive equations in sigma coordinates. *Mon. Wea. Rev.*, 111, 34-45.
- Asselin, R. (1972) Frequency filter for time integrations. *Mon. Wea. Rev.*, 100, 487-490.
- Baum, S. K., Crowley, T. J. (2001) GCM response to Late Precambrian (~ 590Ma) ice-covered continents. *Geophys. Res. Lett.*, 28, 583-586.
- Beljaars A. C. M., Holtslag A. A. M. (1991) Flux parameterization overland surfaces for atmospheric models. *J. Appl. Meteor.*, 30, 327-341.
- Budyko, M. I. (1969) The effect of solar radiation variations on the climate of the Earth. *Tellus*, 21, 611-619.
- Chou M.-D., Lee K.-T. (1996) Parameterizations for the absorption of solar radiation by water vapor and ozone. *J. Atmos. Sci.*, 53, 1203-1208.
- Chou M.-D., Suarez M.J., Liang X.-Z., Yan M.M.-H. (2001) A thermal infrared radiation parameterization for atmospheric studies. 19, NASA/TM-2001-104606.
- Delworth, T. L., Manabe, S. (1988) The influence of potential evaporation on the variabilities of simulated soil wetness and climate. *J. Clim.*, 1, 523-547.
- Edson, A., Lee, S., Bannon, P., Kasting, J.F., Pollard, D. (2011) Atmospheric circulations of terrestrial planets orbiting low-mass stars. *Icarus*, 212, 1-13. doi:10.1016/j.icarus.2010.11.023
- GFD Dennou Club dcm model project (2020) AGCM5.3, <https://dennou.org/library/agcm5/index.htm.en>
- GFD Dennou Club dcm model project (2020) Dennou-Club Planetary Atmospheric model.
- Heng, K., Vogt, S.S., (2011) Gliese 581g as a scaled-up version of Earth: atmospheric circulation simulations. *Mon. Not. R. Astron. Soc.*, 415, 2145-2157. doi:10.1111/j.1365-2966.2011.18853.x
- Hoffman, P. F., Kaufman, A. J., Halverson, G. P., Schrag, D. P. (1998) A neoproterozoic snowball Earth. *Science*, 281, 1342-1346.
- Hu, Y., Yang, J. (2014) Role of ocean heat transport in climates of tidally locked exoplanets around M dwarf stars. *Proc. Natl. Acad. Sci. USA*, 111, 629-634. doi:10.1073/pnas.1315215111
- Ingersoll, A. P. (1969) The runaway greenhouse: A history of water on Venus. *J. Atmos. Sci.*, 26, 1191-1198.
- Ishiwatari, M., Nakajima, K., Takehiro, S., Hayashi, Y.-Y. (1998) The dependency of the structure of the three-dimensional gray atmosphere on the solar constant and the runaway greenhouse states. *Nagare Multimedia*, 17, pap.3, <http://www.nagare.or.jp/mm/98/ishiwata/index.htm>
- Ishiwatari, M., Takehiro, S., Nakajima, K., Hayashi, Y.-Y. (2002) A numerical study on appearance of the runaway greenhouse state of a three-dimensional atmosphere. *J. Atmos. Sci.*, 59, 3223-3238. doi:10.1175/1520-0469(2002)059<3223:ANSOAO>2.0.CO;2

- Ishiwatari, M., Nakajima, K., Takehiro, S. I., Hayashi, Y.-Y. (2007) Dependence of climate states of gray atmosphere on solar constant: From the runaway greenhouse to the snowball states. *J. Geophys. Res.*, 112, D13. doi:10.1029/2006JD007368, retracted.
- Ishiwatari M. (2014) The runaway greenhouse state. *Tenki*, 61, 123-124 (in Japanese).
- Ishiwatari, M., Nakajima, K., Takehiro, S. I., Hayashi, Y.-Y., Y. Kawai, Y.O. Takahashi, Revision of "Dependence of climate states of gray atmosphere on solar constant: From the runaway greenhouse to the snowball states" by Ishiwatari et al. (2007). submitted to *J. Geophys. Res.*
- Joshi, M. M., Haberle, R. M., Reynolds, R. T. (1997) Simulations of the atmospheres of synchronously rotating terrestrial planets orbiting M Dwarfs: conditions for atmospheric collapse and the implications for habitability. *Icarus*, 129, 450-465. doi:10.1006/icar.1997.5793
- Joshi, M. M. (2003) Climate Model Studies of Synchronously Rotating Planets. *Astrobiol.*, 3, 415-427. doi:10.1089/153110703769016488
- Kasahara, A. (1976) Normal modes of ultralong waves in the atmosphere. *Mon. Wea. Rev.*, 104, 669-690. doi:10.1175/1520-0493(1976)104<0669:NMOUWI>2.0.CO;2
- Kashimura H., Enomoto T., Takahashi Y.O. (2013) Non-negative filter using arcsine transformation for tracer advection with semi-Lagrangian scheme. *SOLA*, 9, 125-128.
- Kasting, J. F. (1988) Runaway and moist greenhouse atmospheres and the evolution of Earth and Venus. *Icarus*, 74, 472-494.
- Kawai, Y., Takahashi, Y. O., Ishiwatari, M., Nakajima, K., Takehiro, S., Kashimura, H., Nishizawa, S., Tomita, H., Hayashi, Y.-Y. (2020) Solar constant dependence of climate states of an ocean planet with gray atmosphere: Effect of heat capacity and heat transport of the ocean. in preparation.
- Komabayashi, M. (1967) Discrete equilibrium temperatures of a hypothetical planet with the atmosphere and the hydrosphere of one component-two phase system under constant solar radiation. *J. Meteorol. Soc. Jpn.*, 45, 137-139.
- Leconte J., Forget F., Charnay B., Wordsworth R., Pottier A. (2013) Increased insolation threshold for runaway greenhouse processes on Earth-like planets. *Nature*, 504, 268-271.
- Longuet-Higgins, M.S. (1968) The eigenfunctions of Laplace's tidal equations over a sphere. *Phil. Trans. Royal Soc. London A: Math. Phys. Eng. Sci.*, 262, 511-607. doi:10.1098/rsta.1968.0003
- Louis, J.-F. (1979) A parametric model of vertical eddy fluxes in the atmosphere. *Bound.-Layer Meteor.*, 17, 187-202.
- Manabe, S., Smagorinsky, J., Strickler, R. F. (1965) Simulated climatology of a general circulation model with a hydrologic cycle., *Mon. Wea. Rev.*, 93, 769-798. doi:10.1175/1520-0493(1965)093<0769:SCOAGC>2.3.CO;2
- Mellor G.L., Yamada T. (1974) A hierarchy of turbulence closure models for planetary boundary layers. *J. Atmos. Sci.*, 31, 1791-1806.
- Merlis, T. M. and T. Schneider (2010) Atmospheric dynamics of Earth-like tidally locked aquaplanets. *J. Adv. Model. Earth Syst.*, 2, Art. #13, 17 pp. doi:10.1029/JAMES.2010.2.13
- Moorthi S., Suarez M. J. (1992) Relaxed Arakawa-Schubert: A parameterization of moist convection for general circulation models. *Mon. Wea. Rev.*, 120, 978-1002.
- Nakajima, S., Hayashi, Y.-Y., Abe, Y. (1992) A study on the "runaway greenhouse effect" with a one dimensional radiative convective equilibrium model. *J. Atmos. Sci.*, 49, 2256-2266. doi:10.1175/1520-0469(1992)049<2256:ASOTGE>2.0.CO;2
- Noda, S., Ishiwatari, M., Nakajima, K., Takahashia, Y.O., Takehiro, S., Onishi, M., Hashimoto, G.L., Kuramoto, K., Hayashi, Y.-Y. (2017) The circulation pattern and day-night heat transport in the atmosphere of a synchronously rotating aquaplanet: dependence on planetary rotation rate, *Icarus*, 282, 1-18. doi:10.1016/j.icarus.2016.09.004
- Pollack, J. B. (1971) A nongrey calculation of the runaway greenhouse: Implications for Venus' past and present. *Icarus*, 14, 295-306.
- Sardeshmukh, P.D., Hoskins, B.J. (1988) The generation of global rotational flow by steady idealized tropical divergence. *J. Atmos. Sci.*, 45, 1228-1251. doi:10.1175/JAS-D-14-0235.1
- Satoh, M. (1994) Hadley circulations in radiative-convective equilibrium in an axially symmetric atmosphere. *J. Atmos. Sci.*, 51, 1947-1968.
- Sellers, W. D. (1969) A climate model based on the energy balance of the Earth-atmosphere system. *J. Appl. Meteorol.*, 8, 392-400.
- Shapiro, R., 1971: The use of linear filtering as a parameterization of atmospheric diffusion. *J. Atmos. Sci.*, 28, 523-531.
- Showman, A. P., Wordsworth, R. D., Merlis, T. M., Kaspi, Y. (2013) Atmospheric Circulation of Terrestrial Planets. *Comparative Climatology of Terrestrial Planets*, 1, 277-326.

- Von Bloh, W., Bounama, C., Cuntz, M., Franck, S. (2007) The habitability of super-Earth in Gliese 581. *Astron. Astrophys.*, 476 (3), 1365-1371. doi:10.1051/0004-6361:20077939
- Wordsworth, R.D., Forget, F., Selsis, F., Millour, E., Charnay, B., Madeleine, J.-B. (2011) Gliese 581d is the first discovered terrestrial-mass exoplanet in the habitable zone. *Astrophys. J. Lett.*, 733, L48. doi:10.1088/2041-8205/733/2/L48
- Yang, J., Cowan, N.B., Abbot, D.S. (2013) Stabilizing cloud feedback dramatically expands the habitable zone of tidally locked planets. *Astrophys. J. Lett.*, 771, L45. doi:10.1088/2041-8205/771/2/L45

Contact person

Masaki Ishiwatari
Graduate School of Science, Hokkaido University
Kita 8, Nishi 5, Kita-ku, Sapporo, Hokkaido, 060-0808 Japan
Phone: +81-11-706-3564, E-mail: momoko@gfd-dennou.org
<https://www.gfd-dennou.org/index.html.en>

CGER'S SUPERCOMPUTER ACTIVITY REPORT (Out of stock)

Vol. 1-1992 (CGER-I010-1994)	Vol. 8-1999 (CGER-I043-2000)
Vol. 2-1993 (CGER-I016-1994)	Vol. 9-2000 (CGER-I050-2002)
Vol. 3-1994 (CGER-I020-1995)	Vol.10-2001 (CGER-I054-2002)
Vol. 4-1995 (CGER-I024-1996)	Vol.11-2002 (CGER-I058-2004)
Vol. 5-1996 (CGER-I030-1997)	Vol.12-2003 (CGER-I061-2005)
Vol. 6-1997 (CGER-I034-1999)	Vol.13-2004 (CGER-I064-2006)
Vol. 7-1998 (CGER-I039-2000)	Vol.14-2005 (CGER-I070-2007)

.....

国立環境研究所スーパーコンピュータ利用研究年報 NIES Supercomputer Annual Report

平成 18 年度 2006 (CGER-I078-2008) Out of stock
 平成 19 年度 2007 (CGER-I086-2008) Out of stock
 平成 20 年度 2008 (CGER-I090-2009) Out of stock
 平成 21 年度 2009 (CGER-I095-2010) Out of stock
 平成 22 年度 2010 (CGER-I099-2011) Out of stock
 平成 23 年度 2011 (CGER-I106-2012) Out of stock
 平成 24 年度 2012 (CGER-I113-2013) Out of stock
 平成 25 年度 2013 (CGER-I119-2014) Out of stock
 平成 26 年度 2014 (CGER-I125-2015)
 平成 27 年度 2015 (CGER-I130-2016)
 平成 28 年度 2016 (CGER-I136-2017)
 平成 29 年度 2017 (CGER-I141-2018)
 平成 30 年度 2018 (CGER-I146-2019)
 令和元年度 2019 (CGER-I151-2020)

.....

CGER'S SUPERCOMPUTER MONOGRAPH REPORT

- Vol. 1 CGER-I021-'96 (Out of stock)
KOMORI S.: Turbulence Structure and CO₂ Transfer at the Air-Sea Interface and Turbulent Diffusion in Thermally-Stratified Flows
- Vol. 2 CGER-I022-'96 (Out of stock)
TOKIOKA T., NODA A., KITO H. A., NIKAI DOU Y., NAKAGAWA S., MOTOI T., YUKIMOTO S., TAKATA K.: A Transient CO₂ Experiment with the MRI CGCM -Annual Mean Response-
- Vol. 3 CGER-I025-'97 (Out of stock)
NUMAGUTI A., SUGATA S., TAKAHASHI M., NAKAJIMA T., SUMI A.: Study on the Climate System and Mass Transport by a Climate Model
- Vol. 4 CGER-I028-'97 (Out of stock)
AKIYOSHI H.: Development of a Global 1-D Chemically Radiatively Coupled Model and an Introduction to the Development of a Chemically Coupled General Circulation Model
- Vol. 5 CGER-I035-'99 (Out of stock)
WATANABE M., AMANO K., KOHATA K.: Three-Dimensional Circulation Model Driven by Wind, Density, and Tidal Force for Ecosystem Analysis of Coastal Seas

- Vol. 6 CGER-I040-2000 (Out of stock)
HAYASHI Y.Y., TOYODA E., HOSAKA M., TAKEHIRO S., NAKAJIMA K., ISHIWATARI M.: Tropical Precipitation Patterns in Response to a Local Warm SST Area Placed at the Equator of an Aqua Planet
- Vol. 7 CGER-I045-2001 (Out of stock)
NODA A., YUKIMOTO S., MAEDA S., UCHIYAMA T., SHIBATA K., YAMAKI S.: A New Meteorological Research Institute Coupled GCM (MRI-CGCM2) -Transient Response to Greenhouse Gas and Aerosol Scenarios-
- Vol. 8 CGER-I055-2003 (Out of stock)
NOZAWA T., EMORI S., NUMAGUTI A., TSUSHIMA Y., TAKEMURA T., NAKAJIMA T., ABE-OUCHI A., KIMOTO M.: Transient Climate Change Simulations in the 21st Century with the CCSR/NIES CGCM under a New Set of IPCC Scenarios
- Vol. 9 CGER-I057-2004 (Out of stock)
MIYAZAKI T., FUJISHIMA S., YAMAMOTO M., WEI Q., HANAZAKI H.: Vortices, Waves and Turbulence in a Rotating Stratified Fluid
- Vol. 10 CGER-I060-2005 (Out of stock)
HAYASHI S., MURAKAMI S., XU K., WATANABE M.: Modeling of Daily Runoff in the Changjiang (Yangtze) River Basin and Its Application to Evaluating the Flood Control Effect of the Three Gorges Project
- Vol. 11 CGER-I063-2006 (Out of stock)
NAKAYAMA T., WATANABE M.: Development of Process-based NICE Model and Simulation of Ecosystem Dynamics in the Catchment of East Asia (Part I)
- Vol. 12 CGER-I073-2007 (Out of stock)
NOZAWA T., NAGASHIMA T., OGURA T., YOKOHATA T., OKADA N., SHIOGAMA H.: Climate Change Simulations with a Coupled Ocean-Atmosphere GCM Called the Model for Interdisciplinary Research on Climate: MIROC
- Vol. 13 CGER-I080-2008 (Out of stock)
SHIBATA K., DEUSHI M.: Simulations of the Stratospheric Circulation and Ozone during the Recent Past (1980-2004) with the MRI Chemistry-Climate Model
- Vol. 14 CGER-I083-2008 (Out of stock)
NAKAYAMA T.: Development of Process-based NICE Model and Simulation of Ecosystem Dynamics in the Catchment of East Asia (Part II)
- Vol. 15 CGER-I092-2010 (Out of stock)
MAKSYUTOV, S., NAKATSUKA Y., VALSALA V., SAITO M., KADYGROV N., AOKI T., EGUCHI N., HIRATA R., IKEDA M., INOUE G., NAKAZAWA T., ONISHI R., PATRA P.K., RICHARDSON A.D., SAEKI T., YOKOTA T.: Algorithms for Carbon Flux Estimation Using GOSAT Observational Data
- Vol. 16 CGER-I097-2011 (Out of stock)
NAKAJIMA K.: Idealized Numerical Experiments on the Space-time Structure of Cumulus Convection Using a Large-domain Two-dimensional Cumulus-Resolving Model
- Vol. 17 CGER-I098-2011 (Out of stock)
UEDA H.: Atmospheric Motion and Air Quality in East Asia
- Vol. 18 CGER-I103-2012 (Out of stock)
NAKAYAMA T.: Development of Process-based NICE Model and Simulation of Ecosystem Dynamics in the Catchment of East Asia (Part III)
- Vol. 19 CGER-I108-2013 (Out of stock)
KOMORI S.: Numerical Simulations of Turbulence Structure and Scalar Transfer across the Air-Water Interfaces
- Vol. 20 CGER-I114-2014 (Out of stock)
NAKAYAMA T.: Development of Process-based NICE Model and Simulation of Ecosystem Dynamics in the Catchment of East Asia (Part IV)

- Vol. 21 CGER-I120-2015
SHIOGAMA H.: Influence of Anthropogenic Aerosol Emissions on Pattern Scaling Projections
- Vol. 22 CGER-I127-2016
SATO H. M., ROH, W., HASHINO, T.: Evaluations of Clouds and Precipitations in NICAM Using the Joint Simulator for Satellite Sensors
- Vol. 23 CGER-I132-2017
GOTO, D., SCHUTGENS, N.A.J., OIKAWA, E., TAKEMURA, T., NAKAJIMA, T.: Improvement of a global aerosol transport model through validation and implementation of a data assimilation system
- Vol. 24 CGER-I138-2018
TAKEMURA, T., AND SPRINTARS DEVELOPER TEAM : Development of a global aerosol climate model SPRINTARS
- Vol. 25 CGER-I143-2019
MAKSYUTOV, S., ODA, T., SAITO, M., TAKAGI, H., BELIKOV, D., VALSALA, V.: Transport modeling algorithms for application of the GOSAT observations to the global carbon cycle modeling
- Vol. 26 CGER-I148-2019
NAKAYAMA, T : Development of Process-based NICE Model and Simulation of Ecosystem Dynamics in the Catchment of East Asia (Part V)
- Vol. 27 CGER-I153-2021
ISHIWATAR, M., NAKAJIMA, K., TAKEHIRO, S., KAWAI, Y., TAKAHASHI, Y.O., HASHIMOTO, G.L., SASAKI, Y., HAYASHI, Y. : Numerical studies on the variety of climates of exoplanets using idealistic configurations

レポートの多くは、地球環境研究センターのウェブサイトから PDF 形式で閲覧可能です。
<https://www.cger.nies.go.jp/ja/activities/supporting/publications/report/>

Many of the reports are also available as PDF files.

See: <https://www.cger.nies.go.jp/en/activities/supporting/publications/report/>

